POLITECNICO DI TORINO

SCUOLA DI DOTTORATO

Dottorato in Ingegneria Elettronica e delle Comunicazioni – XXVI ciclo

PhD Dissertation

Analysis and Design of Microwave and Millimeter-wave Passive Devices for Scientific Instrumentation

Muhammad Zunnoorain FAROOQUI

Tutore
Prof. Renato ORTA,
Dr. Oscar Antonio PEVERINI

Coordinatore del corso di dottorato
Prof. Ivo MONTROSSET

March 2014

Acknowledgements

I wish to express my sincere gratitude to Istituto di Elettronica e di Ingegneria dell'Informazione e delle Telecomunicazioni (IEIIT) of Consiglio Nazionale delle Ricerche (CNR) and, especially, to Dr. Oscar Antonio PEVERINI whose endless help and unbounded support made me able to write this dissertation. His supervision and guidance always kept me on the right track. His curious attitudes always motivate me to explore new solutions. I wish also to express my thankfulness to Dr. Giuseppe VIRONE whose observations and research approach taught me how to synthesize a complex problem in order to make it simpler. I am very obliged to Dr. Giuseppe ADDAMO who helped me to write this thesis and shared his knowledge generously at various stages of my doctoral course apart from the quality and the frequency of the questions. I am also thankful to Mauro LUMIA who provided me the mechanical draft of the Dual-Fold-Stub (DFS) polarizer and assisted me to create the beautiful figures for the dissertation. I also pay my sincere gratitude to Prof. Renato ORTA and Prof. Riccardo TASCONE who provided me the peaceful professional working environment and accommodated me among the Applied Electromagnetics & Electronic Devices (AE&ED) group of IEIIT-CNR.

List of acronyms

AR Axial Ratio

API Application Program Interface

AE&ED Applied Electromagnetics & Electronic Devices

CPU Central Processing Unit

CNR Consiglio Nazionale delle Ricerche

CST-MWS CST Micro Wave Studio Suite

CAD Computer-Aided Design

COM Component Object Model

CF Cost Function

CP Circular Polarization

COM-EM-AT Component Object Model Electromagnetic Automation Tool

CU Correlation Unit

CMB Cosmic Microwave Background

CMBR Cosmic Microwave Background Radiation

CUDA Compute Unified Device Architecture (Nvidia)

DASI Degree Angular Scale Interferometer

DUT Device Under Test

DFS Dual-Fold-Stub

DC Distributed Computing

DG-FEM Discontinuous Galerkin FEM

EM Electromagnetic

EP Elliptical Polarization

EDM Electrical Discharge Machining

FEKO FEKO

FORTRAN FORmula TRANslation

FDTD Finite-Difference Time-Domain Method

FEM Finite-Element Method

GA Genetic Algorithm

GPU Graphics Processing Unit

GOT Global Optimization Toolbox

HFSS Ansys HFSS

HP Hewlett Packard

IEIIT Istituto di Elettronica e di Ingegneria dell'Informazione e delle Telecomunicazioni

LHCP Left Hand Circular Polarization

RHCP Right Hand Circular Polarization

LNA Low Noise Amplifier

LP Linear Polarization

MATLAB® Matrix Laboratory Mathworks, Inc.

MDCST MATLAB® Distributed Computing Server Toolbox

MDCS MATLAB® Distributed Computing Server

OMT Ortho-Mode Transducer

OpenMP Open Multi-Processing

OpenMPI Open Message Passing Interface

OpenCL Open Computing Language

OpenGL Open Graphics Library

PMC Perfect Magnetic Conductor

PEC Perfect Electric Conductor

PCT Parallel Computing Toolbox

PSO Particle Swarm Optimization

RAM Random Access Memory

RF Radio Frequency

SFS Single-Fold-Stub

SEM Spectral-Element Method

TRL Through-Reflection-Line

TDFEM Time-Domain Finite-Element Method

VBA Visual Basic for Applications

VNA Vector Network Analyzer

WCU Waveguide Correlation Unit

XPT Cross Polarization in Transmission

XPR Cross Polarization in Reflection

Contents

Introduction

Discovery of the Cosmic Microwave Background (CMB) in 1965 revealed a new realm to the astrophysicists in order to study the age of the universe. CMB polarization was produced due to the density perturbations and gravitational waves. It can be decomposed into curl-free (E-modes) and grad-free (B-modes) modes and both have the same order of magnitude [1]. CMB anisotropies in polarization has been initially detected by the Degree Angular Scale Interferometer (DASI) [2]. In order to study the cosmological re-ionization history, the measurement of the CMB polarization [3, 4] is one of the key objectives.

The CMB polarized component is quite weak with respect to the unpolarized background. In fact only 10 % of the CMB is estimated to be polarized [5] as compared to the unpolarized component. Hence, in order to detect this faint signal, measurement instruments should have very high sensitivity to the polarized component with a very high rejection to the unpolarized background, i.e. they should have very low systematic errors[2]. This goal can be achieved by exploiting clusters of high-performance polarimeters. The measurement accuracy mainly depends on the performance of the polarimeter's building blocks, e.g. antennas, polarizers, ortho-mode transducers, correlation units and low noise amplifiers. Since arrays containing tens or hundreds of polarimeters are used for Cosmic Microwave Background Radiation (CMBR) measurement, the manufacturing of each polarimeter building block should be compatible with a medium/large-scale production. Hence from the mechanical point of view, each building block should be compact in size, low weight, low cost, easily scalable and easy to manufacture for medium/large-scale production with high precision and accuracy. From the electrical point of view, generally, every component should exhibit good return loss, low cross polarization and high isolation level. Recent astrophysical experiments based on arrays of polarimeters aimed at the detection of the CMB polarization state are QUIET [6], LSPE [7] and QUIJOTE [8, 9].

In this perspective, a novel layout of OMTs and polarizers, that are key passive waveguide elements of dual-circular polarization polarimeters, have been designed during the doctoral program. The polarizer is based on a dual-fold stub design having 20 % bandwidth centered at 94.5 GHz, whereas the broadband OMT [10, 11] is based on turnstile junction with 30 % bandwidth centered at 94 GHz.

Besides the novelty of the electromagnetic design of both components, the manufacturing technology has been duly considered in this research work. As an example, electro-forming techniques provide a monolithic fabrication with good manufacturing accuracy, compactness and without any packing screws, but the machining time is quite long, thus leading to a relatively high cost. Another manufacturing technique commonly used is milling that is compatible with a split-block design of the components. Since the milling process can be automatized, the corresponding manufacturing time and costs are reduced. For this manufacturing process, a limitation in the fabrication of millimeter-wave components can be the minimum size of the milling tool.

Nowadays, the platelet/multilayer manufacturing is an emerging solution in Radio Frequency (RF) design in order to combine high accuracy with large-scale production. Platelet manufacturing has already been employed for the realization of corrugated horn arrays [12, 13, 14, 15] and its Technological Readiness Level (TRL) in this field is relatively high [16]. Platelet manufacturing is definitely cheaper with respect to electroforming [17] and provides the same accuracy level [14]. Hence, there is no trade-off in terms of performance. In a platelet design, each part of the component is machined out of a specific plate by a metal removal technique. Various metal removal techniques can be exploited in this regards. For instance, metal can be removed from each plate through photo-lithography, laser machining or wire Electrical Discharge Machining (EDM). The latter technology is known also as spark erosion technique. Photo-lithographic masks and machine programs can be developed once for all and, then, several identical components can be easily realized. The main limitation comes from the maximum height of the metal layer to be removed. Laser machining and wire spark erosion are good choices because several identical plates can be manufactured in just one machining process. These approaches provide the parallelism in manufacturing that consequently reduces the machining time and the component cost. Finally, a stack of metallic plates can be assembled together by bonding (light brazing or diffusion bonding) or by employing the packing screws in order to assemble the complete component.

In light of the above discussion, the present doctoral research activity focused on the feasibility study and the prototype development of polarizers and OMTs based on platelet manufacturing where metal is removed from each plate through wire EDM. The exploitation of this manufacturing solution provides high level of repeatability and accuracy along with low cost, making this solution well suitable for the realization of polarimetric arrays consisting of tens/hundreds of chains. Both components have been designed by exploiting the Component Object Model Electromagnetic Automation Tool (COM-EM-AT) developed during the doctoral program. Parallel Computing Toolbox (PCT) and MATLAB® Distributed Computing Server Toolbox (MDCST) have also been employed in order to accelerate simulations. The performance of both components have been measured through a vector network

analyzer waveguide setup. A tight agreement between the predicted and measured electrical responses have been achieved.

The layout of the thesis is as follows.

In Chapter 1, basic terminologies for the polarizer (i.e. linear/circular polarization basis, transformation matrices for linear/circular polarization basis, scattering matrix in linear basis and figure-of-merits of the polarizer) are defined. These terminologies are used in the subsequent chapter. The behavior of the polarizer in terms of Stokes parameters is also reported.

Chapter 2 is dedicated to the polarizer design. A polarizer stub configuration is chosen since its structure is suitable for platelet manufacturing. A detailed comparison is performed between the existing single-fold stub structure and the dual-fold stub configuration conceived in the doctoral program. It's proved that the performance required in the astrophysical experiments aimed at the detection of the CMB polarization can not be achieved through the SFS design as long as platelet manufacturing is concerned. Conversely, the DFS configuration proves to be applicable to this manufacturing process. Polarizer performances are reported for DFS designs with one, two and three stubs. Tolerance analysis are also reported in order to verify that the uncertainty in the manufacturing does not degrade significantly the component performance. Two prototypes have been developed and their mechanical accuracy has been verified using a 2-axis non-contact measuring microscope. The electrical performance of the prototypes have been measured through a waveguide setup connected to a vector network analyzer operating in W band. The remarkable agreement between the measured and predicted results confirms the applicability of the polarizer desgin to the fabrication of polarimeter clusters operating in W band.

Chapter 3 is focused on the OMT design. In this chapter a broad-band turnstile junction layout is presented and the complete architecture of a W-band multilayer OMT is reported. The OMT configuration has been specifically designed in view of a platelet manufacturing based on wire EDM. Finally, measurements of the OMT electrical response, being in good agreement with the computed results, are reported.

In Chapter 4, the COM-EM-AT developed during the doctoral program is reported. The COM-EM-AT provides an integration among Matrix Laboratory Mathworks, Inc. (MATLAB®) and a commercial EM tool, e.g. CST Micro Wave Studio Suite (CST-MWS) and Ansys HFSS (HFSS). This tool provides various features like the integration between in-house simulation tools and commercial EM tools and flexibility in terms of optimization, grid parametric analysis and post processing. These features are explained with the help of simple examples.

Chapter 5 is devoted to the Distributed Computing (DC) approach that, as an example, has been applied to the tolerance analysis of the polarizer described in Chapter 2. In order to speed-up the analysis the two MATLAB® toolboxes PCT and MDCST have been employed. Local computer cluster configuration, PCT and MDCST implementation details from the EM perspective along with the obtained

results are reported.

The whole research activity has been carried out in the AE&ED group of the IEIIT that is a research structure of the CNR of Italy. All the component's performances have been measured in the IEIIT-CNR microwave laboratory located in the headquarters inside the main campus of Politecnico di Torino.

Chapter 1

Waveguide Polarizer Principles and Stokes Parameters

1.1 Introduction

A general scheme of correlation polarimeter for the evaluation of the Stokes parameters $\boldsymbol{Q}_m$ and $\boldsymbol{U}_m$ of a partially-polarized radiation is shown in Fig. 1.1. A key role in this scheme is represented by the polarizer that converts the two circular polarizations fields, incident at the antenna, into two mutual orthogonal linear polarizations which are subsequently split by the OMT. Finally, the Stokes parameters are computed by the Correlation Unit (CU). The polarizer features can be realized exploiting different configurations, one of the most common choice is the insertion of iris discontinuities along the waveguide (see Fig. 1.2) as reported in [18] and in [19]. The iris behaves differently for the two polarizations of the $\boldsymbol{TE}_{11}$ mode. Indeed, the $\boldsymbol{TE}_{11}$ mode polarized along $\hat{\mathbf{y}}$ gets a phase advancement with respect to the $\boldsymbol{TE}_{11}$ mode polarized along $\hat{\mathbf{x}}$. This fact is usually described as *inductive* and *capacitive* behavior of the discontinuity for the two polarizations of the incident field.

A polarizer has two physical ports but from an electrical point of view, if only the

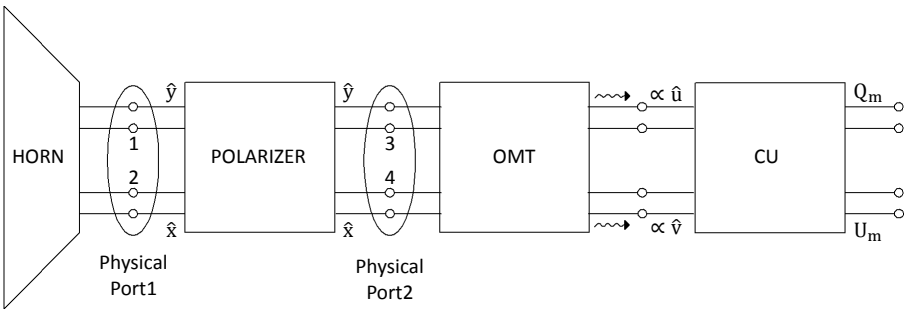

Figure 1.1. General scheme of a dual-circular polarization correlation polarimeter.

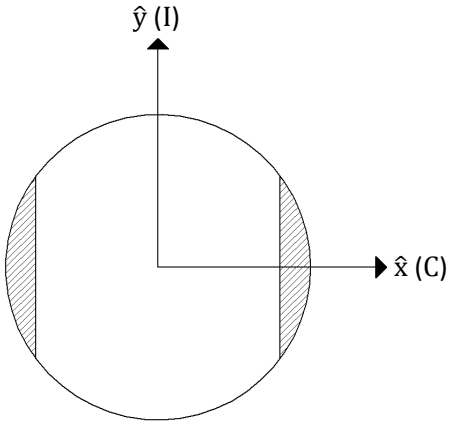

Figure 1.2. Iris discontinuity in circular waveguide. The discontinuity behaves inductively for the TE_{11} mode polarized along $\hat{\mathbf{y}}$ and capacitively for TE_{11} mode polarized along $\hat{\mathbf{x}}$. This explains the "C" and "I" close to the $\hat{\mathbf{x}}$ and $\hat{\mathbf{y}}$ axes.

fundamental mode is considered, then four electrical ports are required in order to take into account the two polarizations of the fundamental mode. As a consequence, the relevant scattering matrix $\mathbf{S}$ is 4×4. The scattered field at the physical port 2 ($\mathbf{E}_2^{scat} = E_{x,2}^{scat}\hat{\mathbf{x}} + E_{y,2}^{scat}\hat{\mathbf{y}}$) is related to the incident one $\mathbf{E}_1^{inc} = E_{x,1}^{inc}\hat{\mathbf{x}} + E_{y,1}^{inc}\hat{\mathbf{y}}$ at the physical port 1 by the scattering matrix block $\mathbf{S}_{21}$. In the ideal case where insertion losses and mutual coupling between the polarizations can be neglected, the matrix block $\mathbf{S}_{21}$ is diagonal and contains only phase shift terms. In particular, the scattered and incident fields components along $\hat{\mathbf{x}}$ and $\hat{\mathbf{y}}$ are related by:

$$\begin{bmatrix} E_{y,2}^{scat} \\ E_{x,2}^{scat} \end{bmatrix} = \begin{bmatrix} e^{j\varphi_y} & 0 \\ 0 & e^{j\varphi_x} \end{bmatrix} \begin{bmatrix} E_{y,1}^{inc} \\ E_{x,1}^{inc} \end{bmatrix}$$

i.e.

$$E_{y,2}^{scat} = e^{j\varphi_y} E_{y,1}^{inc}$$
$$E_{x,2}^{scat} = e^{j\varphi_x} E_{x,1}^{inc}$$

This means that a Left Hand Circular Polarization (LHCP) incident signal (i.e. $\mathbf{E}_1^{inc} = (\hat{\mathbf{x}} + j\hat{\mathbf{y}})/\sqrt{2}$) generates a scattered field at the port 2, which is given as:

$$\mathbf{E}_2^{scat} = \frac{1}{\sqrt{2}}(e^{j\varphi_x}\hat{\mathbf{x}} + je^{j\varphi_y}\hat{\mathbf{y}}) = \frac{e^{j\varphi_x}}{\sqrt{2}}(\hat{\mathbf{x}} + je^{j(\varphi_y - \varphi_x)}\hat{\mathbf{y}}) = \frac{e^{j\varphi_x}}{\sqrt{2}}(\hat{\mathbf{x}} + je^{j\Delta\varphi}\hat{\mathbf{y}})$$

where $\Delta\varphi = \varphi_y - \varphi_x$.
If the polarizer is designed such that $\Delta\varphi = \pi/2$ then $\mathbf{E}_2^{scat}$ is linear polarized along $\hat{\mathbf{v}} = (\hat{\mathbf{x}} - \hat{\mathbf{y}})/\sqrt{2}$ direction. Similarly, a Right Hand Circular Polarization (RHCP) incident signal at the port 1 generates a scattered field at the port 2 that is linearly

polarized along $\hat{\mathbf{u}} = (\hat{\mathbf{x}} + \hat{\mathbf{y}})/\sqrt{2}$. The OMT connected to the polarizer is rotated by 45° with respect to the polarizer principal axes. In this way, the OMT output ports are proportional to $\hat{\mathbf{u}}$ and $\hat{\mathbf{v}}$ field components.

The example just considered here puts in evidence that the polarizer $\pi/2$ phase difference between the inductive and capacitive polarizations is necessary for the correct work of the polarimeter chain.

1.2 Polarizer's Basis Definition and Matrix Relation

The brief discussion of the previous section has shown that the polarizer characteristics can be clearly described by exploiting three different set of basis:

- Principal direction basis
- Circular polarization basis
- Tilted polarization basis

Principal Direction Basis The *principal* direction basis is defined by $\hat{\mathbf{x}}$ and $\hat{\mathbf{y}}$ orthonormal unit vectors. They form the natural basis to describe the two polarizations[1] of the fundamental TE_{11} mode. The scattering matrix of the polarizer is computed in this basis.

Circular Polarization Basis The *circular* polarization basis is composed by the $\hat{\mathbf{e}}_{\mathrm{R}}$ and $\hat{\mathbf{e}}_{\mathrm{L}}$ orthonormal unit vectors. These vectors are related to the principal direction basis by the following equations:

$$\left.\begin{aligned} \hat{\mathbf{e}}_{\mathrm{R}} &= \frac{1}{\sqrt{2}}(\hat{\mathbf{x}} - jp\hat{\mathbf{y}}) \\ \hat{\mathbf{e}}_{\mathrm{L}} &= \frac{1}{\sqrt{2}}(\hat{\mathbf{x}} + jp\hat{\mathbf{y}}) \end{aligned}\right\} \tag{1.1}$$

Since the right and left circular polarizations definitions depend on the wave propagation direction $\hat{\mathbf{n}}$, we introduce the symbol p to take into account both cases, i.e. $\hat{\mathbf{n}} = \pm\hat{\mathbf{z}}$. In particular p is equal to:

$$p = \begin{cases} -1 & \text{if } \hat{\mathbf{n}} = -\hat{\mathbf{z}} \\ 1 & \text{if } \hat{\mathbf{n}} = +\hat{\mathbf{z}} \end{cases}$$

[1] sometimes also referred as inductive ($\hat{\mathbf{y}}$) and capacitive ($\hat{\mathbf{x}}$) polarizations

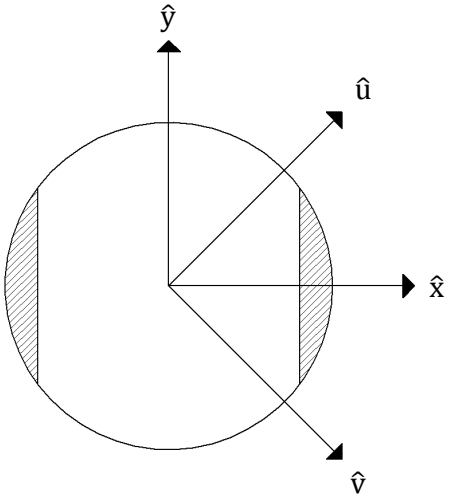

Figure 1.3. Tilted polarization basis representation.

This basis is the natural basis to describe the incident (and scattered) field at the port 1 of the polarizer, i.e. the port connected to the antenna, as depicted in Fig. 1.1.

Tilted Polarization Basis The *tilted* polarization basis is composed by $\hat{\mathbf{u}}$ and $\hat{\mathbf{v}}$ orthonormal unit vectors. These vectors are related to $\hat{\mathbf{x}}$ and $\hat{\mathbf{y}}$ by the following equations (see Fig. 1.3):

$$\left.\begin{aligned} \hat{\mathbf{u}} &= \frac{1}{\sqrt{2}}(\hat{\mathbf{x}} + \hat{\mathbf{y}}) \\ \hat{\mathbf{v}} &= \frac{1}{\sqrt{2}}(\hat{\mathbf{x}} - \hat{\mathbf{y}}) \end{aligned}\right\} \tag{1.2}$$

This basis is the natural basis to describe the scattered (and incident) field at the port 2 of the polarizer, i.e. the port connected to the OMT, as depicted in Fig. 1.1.

1.2.1 Transformation Matrices for the Electric Field

The three different basis introduced in the previous section are necessary for the description of the polarizer characteristics. The purpose of this section is to derive the transformation matrices which relate the components of the electric field described in these three different basis. The electric field $\mathbf{E}$ in principal, circular and tilted polarization basis can be written as

$$\mathbf{E} = E_x\hat{\mathbf{x}} + E_y\hat{\mathbf{y}} = E_R\hat{\mathbf{e}}_\mathbf{R} + E_L\hat{\mathbf{e}}_\mathbf{L} = E_u\hat{\mathbf{u}} + E_v\hat{\mathbf{v}} \tag{1.3}$$

The projection of Eq.(1.3) with $\hat{\mathbf{e}}_{\mathbf{R}}$ permits to find the relation between E_R and E_x and E_y:

$$E_R = \langle \mathbf{E}, \hat{\mathbf{e}}_{\mathbf{R}} \rangle = \frac{1}{\sqrt{2}} \left(jpE_y + E_x \right) \tag{1.4}$$

similarly, the projection of $\mathbf{E}$ along $\hat{\mathbf{e}}_{\mathbf{L}}$:

$$E_L = \langle \mathbf{E}, \hat{\mathbf{e}}_{\mathbf{L}} \rangle = \frac{1}{\sqrt{2}} \left(-jpE_y + E_x \right) \tag{1.5}$$

Combining Eq.(1.4) with (1.5), one obtains in matrix form:

$$\begin{bmatrix} E_R \\ E_L \end{bmatrix} = \frac{1}{\sqrt{2}} \begin{bmatrix} j\,p & 1 \\ -j\,p & 1 \end{bmatrix} \cdot \begin{bmatrix} E_y \\ E_x \end{bmatrix} = \mathbf{T}_p \cdot \begin{bmatrix} E_y \\ E_x \end{bmatrix}$$

where

$$\mathbf{T}_p = \frac{1}{\sqrt{2}} \begin{bmatrix} j\,p & 1 \\ -j\,p & 1 \end{bmatrix}$$

Similarly by projecting $\mathbf{E}$ along $\hat{\mathbf{u}}$ and $\hat{\mathbf{v}}$ one obtains:

$$E_u = \langle \mathbf{E}, \hat{\mathbf{u}} \rangle = \frac{1}{\sqrt{2}} \left(E_y + E_x \right) \tag{1.6}$$

$$E_v = \langle \mathbf{E}, \hat{\mathbf{v}} \rangle = \frac{1}{\sqrt{2}} \left(-E_y + E_x \right) \tag{1.7}$$

Combining Eq.(1.6) and (1.7):

$$\begin{bmatrix} E_u \\ E_v \end{bmatrix} = \frac{1}{\sqrt{2}} \begin{bmatrix} 1 & 1 \\ -1 & 1 \end{bmatrix} \cdot \begin{bmatrix} E_y \\ E_x \end{bmatrix} = \mathbf{T} \cdot \begin{bmatrix} E_y \\ E_x \end{bmatrix}$$

where:

$$\mathbf{T} = \frac{1}{\sqrt{2}} \begin{bmatrix} 1 & 1 \\ -1 & 1 \end{bmatrix}$$

1.3 Polarizer Scattering Matrix

The polarizer analysis is performed in the principal direction basis, while its operative condition are naturally described considering the circular and tilted basis at the input physical port (1) and output physical port (2), respectively. It is, then, necessary to to derive the relation between the scattering matrices of the polarizer where these two different basis sets are employed.

The polarizer has two physical ports but four electrical ports are necessary to describe the different polarizations of the TE_{11} mode. With reference to Fig. 1.1,

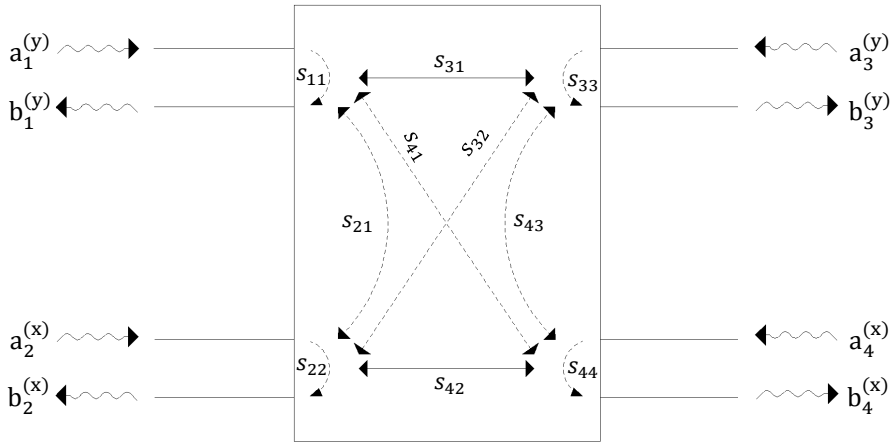

Figure 1.4. Polarizer scattering matrix in principal direction basis.

electrical port 1 and port 2 are connected to the feed antenna/horn whereas the electrical port 3 and port 4 are connected to the OMT. Using the principal polarization basis, we assume that electrical port 1 and 3 are related to $\hat{\mathbf{y}}$ direction while the electrical ports 2 and 4 are related to $\hat{\mathbf{x}}$ direction. Let $\mathbf{S}$ be the relevant 4×4 polarizer scattering matrix. For definition, by collecting the scattered and incident power waves in column vectors $\mathbf{b}$ and $\mathbf{a}$, respectively, we have:

$$\mathbf{b} = \mathbf{S} \cdot \mathbf{a}$$

where:

$$\mathbf{b} = \begin{bmatrix} b_1^{(y)} \\ b_2^{(x)} \\ b_3^{(y)} \\ b_4^{(x)} \end{bmatrix} \qquad \mathbf{a} = \begin{bmatrix} a_1^{(y)} \\ a_2^{(x)} \\ a_3^{(y)} \\ a_4^{(x)} \end{bmatrix}$$

Here the superscripts are employed to emphasize the relevant polarization direction, as referred in Fig. 1.4.

The physical ports 1 and 2 can be described in the circular and tilted polarization basis, respectively. Let $\tilde{\mathbf{S}}$ be the 4×4 polarizer scattering matrix computed in this reference system. In particular the electrical ports 1 and 2 (which belong to physical port 1) would refer to right and left circular polarization basis, respectively, while the electrical ports 3 and 4 (which belong to physical port 2) refer to the $\hat{\mathbf{u}}$ and $\hat{\mathbf{v}}$ tilted polarization basis, respectively as referred in Fig. 1.5. By collecting the scattered and incident power waves in the column vectors $\tilde{\mathbf{b}}$ and $\tilde{\mathbf{a}}$, respectively, we obtain the following matrix relation:

$$\tilde{\mathbf{b}} = \tilde{\mathbf{S}} \cdot \tilde{\mathbf{a}}$$

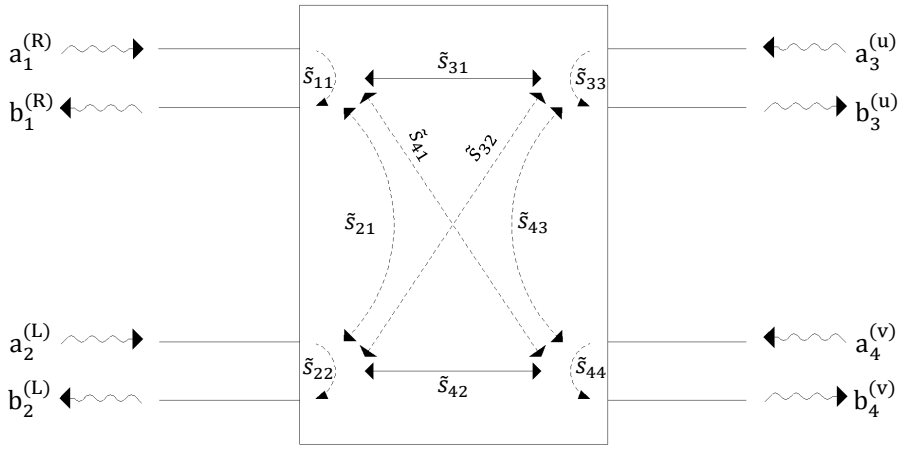

Figure 1.5. Polarizer scattering matrix in circular and tilted basis.

where:

$$\tilde{\mathbf{b}} = \begin{bmatrix} \tilde{b}_1^{(R)} \\ \tilde{b}_2^{(L)} \\ \tilde{b}_3^{(u)} \\ \tilde{b}_4^{(v)} \end{bmatrix} \quad \tilde{\mathbf{a}} = \begin{bmatrix} \tilde{a}_1^{(R)} \\ \tilde{a}_2^{(L)} \\ \tilde{a}_3^{(u)} \\ \tilde{a}_4^{(v)} \end{bmatrix}$$

To get the relation between the $\tilde{\mathbf{S}}$ and $\mathbf{S}$ it is necessary to exploit matrices $\mathbf{T}_p$ and $\mathbf{T}$ introduced in section 1.2.1. The incident and scattered power waves in these two different polarization basis are indeed related by the following equations:

$$\begin{bmatrix} \tilde{a}_1^{(R)} \\ \tilde{a}_2^{(L)} \end{bmatrix} = \hat{\mathbf{T}} \begin{bmatrix} a_1^{(y)} \\ a_2^{(x)} \end{bmatrix}, \quad \begin{bmatrix} \tilde{b}_1^{(R)} \\ \tilde{b}_2^{(L)} \end{bmatrix} = \check{\mathbf{T}} \begin{bmatrix} b_1^{(y)} \\ b_2^{(x)} \end{bmatrix}, \quad \begin{bmatrix} \tilde{a}_3^{(u)} \\ \tilde{a}_4^{(v)} \end{bmatrix} = \mathbf{T} \begin{bmatrix} a_3^{(y)} \\ a_4^{(x)} \end{bmatrix}, \quad \begin{bmatrix} \tilde{b}_3^{(u)} \\ \tilde{b}_4^{(v)} \end{bmatrix} = \mathbf{T} \begin{bmatrix} b_3^{(y)} \\ b_4^{(x)} \end{bmatrix}$$

where, for sake of notation clearness, $\hat{\mathbf{T}} = \mathbf{T}_p$ with $p = 1$ and $\check{\mathbf{T}} = \mathbf{T}_p$ with $p = -1$. In compact format

$$\left.\begin{aligned} \tilde{\mathbf{a}} &= \mathbf{P}_a \cdot \mathbf{a} \\ \tilde{\mathbf{b}} &= \mathbf{P}_b \cdot \mathbf{b} \end{aligned}\right\}$$

i.e.:

$$\left.\begin{aligned} \mathbf{a} &= (\mathbf{P}_a)^{-1} \cdot \tilde{\mathbf{a}} \\ \mathbf{b} &= (\mathbf{P}_b)^{-1} \cdot \tilde{\mathbf{b}} \end{aligned}\right\} \tag{1.8}$$

where

$$\mathbf{P}_a = \begin{bmatrix} \hat{\mathbf{T}} & \mathbf{0} \\ \mathbf{0} & \mathbf{T} \end{bmatrix} \qquad \mathbf{P}_b = \begin{bmatrix} \check{\mathbf{T}} & \mathbf{0} \\ \mathbf{0} & \mathbf{T} \end{bmatrix}$$

Finally from the relation

$$\mathbf{b} = \mathbf{S} \cdot \mathbf{a}$$

by substituting Eq.(1.8) we obtain:

$$\begin{aligned}(\mathbf{P}_b)^{-1}\cdot\tilde{\mathbf{b}} &= \mathbf{S}\cdot(\mathbf{P}_a)^{-1}\cdot\tilde{\mathbf{a}}\\ \tilde{\mathbf{b}} &= \underbrace{\mathbf{P}_b\cdot\mathbf{S}\cdot(\mathbf{P}_a)^{-1}}_{\tilde{\mathbf{S}}}\cdot\tilde{\mathbf{a}}\end{aligned}$$

where

$$\tilde{\mathbf{S}} = \mathbf{P}_b\cdot\mathbf{S}\cdot(\mathbf{P}_a)^{-1}$$

By partitioning the scattering matrices $\tilde{\mathbf{S}}$ in the standard 2×2 block division, one obtains:

$$\tilde{\mathbf{S}} = \left[\begin{array}{c:c}\tilde{\mathbf{S}}_{11} & \tilde{\mathbf{S}}_{12}\\ \hdashline \tilde{\mathbf{S}}_{21} & \tilde{\mathbf{S}}_{22}\end{array}\right]$$

where

$$\begin{aligned}\tilde{\mathbf{S}}_{11} &= \check{\mathbf{T}}\,\mathbf{S}_{11}\,(\hat{\mathbf{T}})^{-1}\\ \tilde{\mathbf{S}}_{12} &= \check{\mathbf{T}}\,\mathbf{S}_{12}\,\mathbf{T}^{-1}\\ \tilde{\mathbf{S}}_{21} &= \mathbf{T}\,\mathbf{S}_{21}\,(\hat{\mathbf{T}})^{-1}\\ \tilde{\mathbf{S}}_{22} &= \mathbf{T}\,\mathbf{S}_{22}\,\mathbf{T}^{-1}\end{aligned}$$

The explicit computation of the matrices product is reported in appendix A.2.

1.4 Polarizer Figure-of-Merits

For a designer point of view, any microwave device has to guarantee a very low reflection coefficient at the input ports. This means that the $\mathbf{S}_{11}$ and $\mathbf{S}_{22}$ blocks of the overall polarizer scattering matrix $\mathbf{S}$ has to be minimized. Moreover, in order to guarantee the desired conversion, other requirements has to be taken into account. For the reader convenience they are listed below and discussed in detail in the following subsections.

- Cross Polarization in Transmission (XPT)
- Axial Ratio (AR)
- Cross Polarization in Reflection (XPR)
- Differential Phase Shift

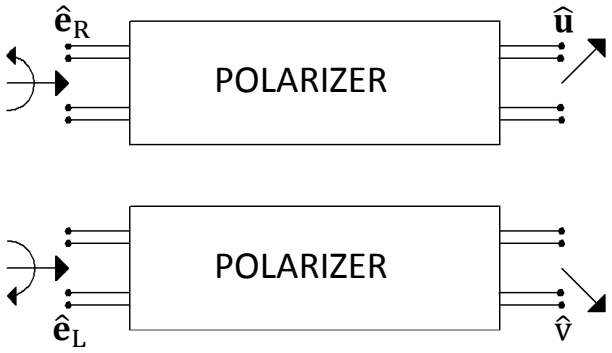

Figure 1.6. Circular and tilted polarization basis.

1.4.1 Cross Polarization in Transmission (XPT)

The main goal of the polarizer is to convert the incident right/left circular polarization(i.e. $\hat{\mathbf{e}}_R/\hat{\mathbf{e}}_L$) in one of the two tilted(i.e. $\hat{\mathbf{u}}/\hat{\mathbf{v}}$) linear polarizations. With reference to Fig. 1.6, the input right (left) circular polarization should be totally converted to the output $\hat{\mathbf{u}}$ ($\hat{\mathbf{v}}$) linear polarization component. The spurious coupling represents the cross-polarization term while the direct contribution is called co-polar term. The XPT is the ratio between the cross-polar and co-polar components. It is useful to derive the expression of XPT as a function of the scattering matrix elements **S**. The generic expression of the incident electric field at the input port 1 expressed in circular basis is given as:

$$\mathbf{E}_1^{inc} = E_R\hat{\mathbf{e}}_R + E_L\hat{\mathbf{e}}_L$$

Then the relevant scattered electric field at port 2 is given as:

$$\mathbf{E}_2^{scat} = \left(E_R\tilde{s}_{31} + E_L\tilde{s}_{32}\right)\hat{\mathbf{u}} + \left(E_R\tilde{s}_{41} + E_L\tilde{s}_{42}\right)\hat{\mathbf{v}} \tag{1.9}$$

If, for instance, the input incident field at the port 1 is only RHCP (i.e. $E_L = 0$) then the Eq.(1.9) reduces to:

$$\mathbf{E}_2^{scat} = E_R\tilde{s}_{31}\hat{\mathbf{u}} + E_R\tilde{s}_{41}\hat{\mathbf{v}}$$

In this case the E_{co} and $E_{\times p}$ components are those directed along $\hat{\mathbf{u}}$ and $\hat{\mathbf{v}}$, respectively, i.e.:

$$\begin{aligned} E_{co} &= E_R\tilde{s}_{31} \\ E_{\times p} &= E_R\tilde{s}_{41} \end{aligned}$$

Since the XPT is the ratio between $E_{\times p}$ and E_{co} we have:

$$\text{XPT} = \frac{E_{\times p}}{E_{co}} = \frac{E_R\tilde{s}_{41}}{E_R\tilde{s}_{31}} = \frac{\tilde{s}_{41}}{\tilde{s}_{31}} = \frac{(s_{42} - s_{32}) + j(s_{31} - s_{41})}{(s_{42} + s_{32}) - j(s_{31} + s_{41})} \tag{1.10}$$

where the last equivalence comes out from the expression of $\tilde{s}_{31}$ and $\tilde{s}_{41}$ as a function of the scattering matrix elements ($s_{i,j}$) (see Appendix A.2).

In the ideal case of perfect polarizer symmetry, the cross coupling between the principal polarizations can be neglected (i.e. $s_{32} = s_{41} = 0$), Eq.(1.10) reduces to:

$$\mathrm{XPT} = \frac{s_{42} + j s_{31}}{s_{42} - j s_{31}} \tag{1.11}$$

From Eq.(1.11) we can derive the condition that is necessary to minimize the XPT. For this purpose we manage the expression as it follows:

$$\mathrm{XPT} = \frac{1 + j\frac{s_{31}}{s_{42}}}{1 - j\frac{s_{31}}{s_{42}}} = \frac{1 + \left|\frac{s_{31}}{s_{42}}\right| e^{j(\angle s_{31} - \angle s_{42} + \pi/2)}}{1 - \left|\frac{s_{31}}{s_{42}}\right| e^{j(\angle s_{31} - \angle s_{42} + \pi/2)}}$$

The XPT is then exactly zero when $\left|\frac{s_{31}}{s_{42}}\right| e^{j(\angle s_{31} - \angle s_{42} + \pi/2)} = -1$ i.e. when

$$\begin{aligned} \left|\frac{s_{31}}{s_{42}}\right| &= 1 \\ \angle s_{31} - \angle s_{42} &= \pi/2 \end{aligned}$$

An equivalent definition of XPT can be obtained by considering the polarizer in transmitter mode. For instance, let us consider an incident electric field polarized along $\hat{\mathbf{u}}$ at the physical port 2 (i.e. $\mathbf{E}_2^{inc} = E_u \hat{\mathbf{u}}$). Then the scattered field at port 1 is given as:

$$\mathbf{E}_1^{scat} = E_u \tilde{s}_{13} \hat{\mathbf{e}}_{\mathbf{R}} + E_u \tilde{s}_{23} \hat{\mathbf{e}}_{\mathbf{L}}$$

where the terms $E_u \tilde{s}_{13} \hat{\mathbf{e}}_{\mathbf{R}}$ and $E_u \tilde{s}_{23} \hat{\mathbf{e}}_{\mathbf{L}}$ are the co-polar and cross-polar components of the scattered field. Then the XPT is given as:

$$\mathrm{XPT} = \frac{\tilde{s}_{23}}{\tilde{s}_{13}} = \frac{s_{23} + s_{24} + j(s_{13} + s_{14})}{s_{23} + s_{24} - j(s_{13} + s_{14})} \tag{1.12}$$

If the polarizer is reciprocal, then the scattering terms $s_{i,j}$ are equal to $s_{j,i}$ and the Eq.(1.12) coincides to Eq.(1.10). Similar expression can be derived by considering an incident electric field polarized along $\hat{\mathbf{v}}$.

1.4.2 Axial Ratio (AR)

The Axial Ratio (AR) is an other way to define the polarization purity of the polarizer. It is defined as the ratio between the major and minor axes of the polarization ellipse of the electric field. From this definition it is clear that in the case of perfect circularly polarized signal the AR = 1, for the generic case of elliptic polarization AR > 1 and, finally, AR tends to $+\infty$ for the linear polarization case.

An incident field at the physical port 2 of the polarizer directed along $\hat{\mathbf{u}}$ (i.e. $\mathbf{E}_2^{inc} = E_u\hat{\mathbf{u}}$) produces a scattered field at physical port 1 equal to

$$\mathbf{E}_1^{scat} = E_u\tilde{s}_{13}\hat{\mathbf{e}}_\mathbf{R} + E_u\tilde{s}_{23}\hat{\mathbf{e}}_\mathbf{L} = \left(\tilde{s}_{13}\hat{\mathbf{e}}_\mathbf{R} + \tilde{s}_{23}\hat{\mathbf{e}}_\mathbf{L}\right) E_u$$

The major and minor axes of the polarization ellipse of the electric field occur when the two components[2] are in phase and in counter-phase, respectively. Then, the AR is equal to:

$$\mathrm{AR} = \frac{|\tilde{s}_{13}| + |\tilde{s}_{23}|}{|\tilde{s}_{13}| - |\tilde{s}_{23}|} = \frac{1 + |\tilde{s}_{23}|/|\tilde{s}_{13}|}{1 - |\tilde{s}_{23}|/|\tilde{s}_{13}|} = \frac{1 + |\mathrm{XPT}|}{1 - |\mathrm{XPT}|}$$

Note that XPT is equal to zero means AR equal to one (i.e. circular polarization). On the contrary when XPT tends to one then AR tends to $+\infty$.

1.4.3 Cross Polarization in Reflection (XPR)

The XPR is a measure of the coupling between the $\hat{\mathbf{u}}$ and $\hat{\mathbf{v}}$ components of the received field at the physical port 2 where a spurious contribution (reflected by the OMT or by the CU) impinge on this port of the polarizer. This mutual coupling between the $\hat{\mathbf{u}}$ and $\hat{\mathbf{v}}$ components has to be minimized since it deteriorates the Stokes parameters determination.

The ratio between the scattered field along $\hat{\mathbf{v}}$ when an incident filed along $\hat{\mathbf{u}}$ impinge at the port 2 is given as:

$$\mathrm{XPR} = \frac{E_v^{scat}}{E_u^{inc}} = \tilde{s}_{43} = \frac{1}{2}\left(s_{44} - s_{33} + s_{43} - s_{34}\right)$$

If the polarizer is reciprocal (i.e. $s_{34} = s_{43}$) it reduces to:

$$\mathrm{XPR} = \frac{1}{2}\left(s_{44} - s_{33}\right) \tag{1.13}$$

We need to consider an other cross-coupling term, i.e. the cross coupling at the physical port 1 between the right and left incident circular polarization. From the scattering matrix definition it is is equal to $\tilde{s}_{21}$ i.e. $\frac{1}{2}\left(s_{11} + s_{22} + j(s_{12} - s_{21})\right)$. If the polarizer is reciprocal (i.e. $s_{12} = s_{21}$), then $\tilde{s}_{21}$ reduces to $\frac{1}{2}(s_{11} + s_{22})$. The XPR is then minimized by reducing the difference $s_{33} - s_{44}$ and the sum $s_{11} + s_{22}$.

[2]The two component considered here are the right- and left-circularly polarized components at electrical ports 1.

1.4.4 Differential Phase Shift

In order to obtain a low level in XPT, polarizer should provide 90° differential phase shift between its inductive and capacitive transmission coefficient as it is discuss in the introductory paragraph of this chapter. Hence differential phase shift is defined as

$$\Phi = \angle \frac{s_{31}}{s_{42}} = \angle s_{31} - \angle s_{42}$$

where s_{31} and s_{42} has the usual meaning as depicted in Fig. 1.4.

There are some other derived terms from differential phase shift which really help to synthesize the design. These derived terms are described below.

Average Differential Phase Shift as it is obvious from its name, is the average of the differential phase shift between the inductive and capacitive transmission coefficient in the operative frequency band. It is defined as

$$\overline{\Phi} = \underset{\Delta\omega}{\text{mean}}\{\Phi(\omega)\} \tag{1.14}$$

In Eq.(1.14) $\Delta\omega$ indicate the operative bandwidth.

Absolute Differential Phase Error is measure the absolute deviation of Φ from the reference phase value. In Eq.(1.15) the reference phase value is defined as the average differential phase shift in the operative band whereas in Eq.(1.16) the reference phase value is set to the 90°

$$\Delta\Phi = \max_{\Delta\omega} \left|\Phi(\omega) - \overline{\Phi}\right| \tag{1.15}$$

$$\Delta\Phi = \max_{\Delta\omega} |\Phi(\omega) - 90^\circ| \tag{1.16}$$

Relative Differential Phase Error is the ratio between the absolute differential phase error and the average differential phase shift. It measure the uncertainty in the Φ relative to the reference phase value. It is defined as

$$\epsilon_{\Delta\Phi} = \left|\frac{\Delta\Phi}{\overline{\Phi}}\right| \times 100$$

1.5 Stokes Parameters

As well known, in time domain the generic expression of the transverse electric field in the **x-y** plane is:

$$\mathscr{E}(t) = \mathscr{E}_x \cos(\omega_0 t + \varphi_x)\hat{\mathbf{x}} + \mathscr{E}_y \cos(\omega_0 t + \varphi_y)\hat{\mathbf{y}}$$

where $\mathscr{E}_x$ and $\mathscr{E}_y$ are the amplitude of the x and y components, respectively. In the frequency domain, with the $e^{+j\omega t}$ time convention, the previous equation reads as

$$\mathbf{E} = E_x\hat{\mathbf{x}} + E_y\hat{\mathbf{y}}$$

If circular polarization is considered the previous expression becomes

$$\mathbf{E} = E_L\hat{\mathbf{e}}_\mathbf{L} + E_R\hat{\mathbf{e}}_\mathbf{R}$$

where $\hat{\mathbf{e}}_\mathbf{L}$ and $\hat{\mathbf{e}}_\mathbf{R}$ are the unit vectors for the left and right circular polarization, respectively. The Stokes parameters represent a standard way to describe the polarization state of a signal. Referring to the linear component of the signal, they are defined as[3]

$$\begin{aligned} I &= \left\langle |E_x|^2 + |E_y|^2 \right\rangle \\ Q &= \left\langle |E_x|^2 - |E_y|^2 \right\rangle \\ U &= 2\Re\left\langle E_x E_y^* \right\rangle \\ V &= -2\Im\left\langle E_x E_y^* \right\rangle \end{aligned} \tag{1.17}$$

where the superscript $*$ denotes the complex conjugate while $< ... >$ represents the average value in the operative frequency band.

The Stokes parameters are related by the classical formula:

$$I^2 = Q^2 + U^2 + V^2 \tag{1.18}$$

The term **I** is the total intensity of the signal, **Q** represents the amount of linear (horizontal/vertical) polarization, **U** describes the amount of linear $\pm 45^\circ$ tilted polarization, finally **V** quantifies the amount of left hand or right hand circular polarizations. It is easy to prove that for a linearly polarizer signal $V = 0$, whereas for a circular polarized signal $Q = U = 0$ while $V = \pm 1$. In the more general case of an elliptical polarization, all the Stokes parameters are different from zero. Note that in the case of unpolarized signal the average values of E_x and E_y are identical and there is no correlation between them. Therefore Q, V and U are zero.

In the correlation radiometer scheme shown in Fig 1.1, on page 5, the system works in circular polarization basis, for which the Stokes parameters assume the following expressions:

$$\begin{aligned} I &= \left\langle |E_L|^2 + |E_R|^2 \right\rangle \\ Q &= 2\Re\langle E_L E_R^* \rangle \\ U &= -2\Im\langle E_L E_R^* \rangle \\ V &= \left\langle |E_L|^2 - |E_R|^2 \right\rangle \end{aligned} \tag{1.19}$$

[3]Stokes parameters were defined by George Gabriel Stokes in 1852 [20].

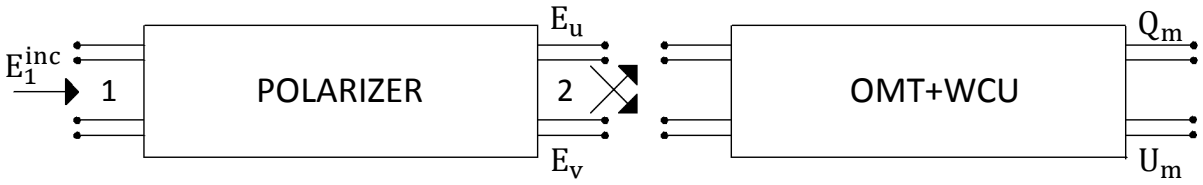

Figure 1.7. Incident signal on the polarizer and its propagation along the Ortho-Mode Transducer (OMT) and the Waveguide Correlation Unit (WCU) for the computation of the Stokes parameters Q_m and U_m.

1.6 Stokes Parameter's Formulation for Polarizer

In order to derive the effect of the polarizer on the Stokes parameters of the signals entering at physical port(1) and exiting from physical port(2), let us consider a generic incident field at the port 1 of the polarizer, as referred in Fig. 1.7:

$$\mathbf{E}_1^{inc} = E_R \hat{\mathbf{e}}_\mathbf{R} + E_L \hat{\mathbf{e}}_\mathbf{L}$$

By exploiting the scattering matrix notation, the scattered field at the port 2 is equal to:

$$\mathbf{E}_2^{scat} = \left(E_R \tilde{s}_{31} + E_L \tilde{s}_{32}\right) \hat{\mathbf{u}} + \left(E_R \tilde{s}_{41} + E_L \tilde{s}_{42}\right) \hat{\mathbf{v}} = E_u \hat{\mathbf{u}} + E_v \hat{\mathbf{v}}$$

where

$$E_u = E_R \tilde{s}_{31} + E_L \tilde{s}_{32} = \frac{E_R}{2}\left[(s_{42} + s_{32}) - j(s_{31} + s_{41})\right] + \frac{E_L}{2}\left[(s_{42} + s_{32}) + j(s_{31} + s_{41})\right]$$
$$E_v = E_R \tilde{s}_{41} + E_L \tilde{s}_{42} = \frac{E_R}{2}\left[(s_{42} - s_{32}) + j(s_{31} - s_{41})\right] + \frac{E_L}{2}\left[(s_{42} - s_{32}) - j(s_{31} - s_{41})\right]$$

We want to evaluate the Stokes parameters Q_m and U_m at the output port 2 as a function of the incident ones. The relation would put in evidence the effect of the polarizer and would show the figures of merit which has to be optimized in the design procedure.
Since $Q_m = 2\Re\{E_v E_u^*\}$ and $U_m = -2\Im\{E_v E_u^*\}$, let us consider the product $2E_v E_u^*$[4]:

$$\begin{aligned} 2E_v E_u^* = \; & \frac{1}{2}\left(|s_{42}|^2 - |s_{32}|^2 + |s_{31}|^2 - |s_{41}|^2\right) Q + \left(\Re\{s_{41}s_{42}^*\} - \Re\{s_{31}s_{32}^*\}\right) U \\ + \; & \frac{1}{2}\left(|s_{42}|^2 - |s_{32}|^2 - |s_{31}|^2 + |s_{41}|^2\right) I + \left(-\Im\{s_{41}s_{42}^*\} + \Im\{s_{31}s_{32}^*\}\right) V \\ + \; & j\left(\Im\{s_{42}s_{32}^*\} + \Im\{s_{31}s_{41}^*\}\right) Q + j\left(\Im\{s_{42}s_{31}^*\} - \Im\{s_{32}s_{41}^*\}\right) U \\ + \; & j\left(\Im\{s_{42}s_{32}^*\} - \Im\{s_{31}s_{41}^*\}\right) I - j\left(\Re\{s_{42}s_{31}^*\} - \Re\{s_{32}s_{41}^*\}\right) V \end{aligned} \quad (1.20)$$

[4]The detailed derivation is reported in appendix A.3

where Q, U, V and I are the input Stokes parameters as defined in Eq.(1.17).

From Eq.(1.20) we obtain

$$\begin{aligned} Q_m = & \frac{1}{2}\left(|s_{42}|^2 - |s_{32}|^2 + |s_{31}|^2 - |s_{41}|^2\right)Q \quad + \left(\Re\{s_{41}s_{42}^*\} - \Re\{s_{31}s_{32}^*\}\right)U \\ + & \frac{1}{2}\left(|s_{42}|^2 - |s_{32}|^2 - |s_{31}|^2 + |s_{41}|^2\right)I \quad + \left(-\Im\{s_{41}s_{42}^*\} + \Im\{s_{31}s_{32}^*\}\right)V \\ U_m = & -\left(\Im\{s_{42}s_{32}^*\} + \Im\{s_{31}s_{41}^*\}\right)Q \quad + \left(\Im\{s_{32}s_{41}^*\} - \Im\{s_{42}s_{31}^*\}\right)U \\ + & \left(-\Im\{s_{42}s_{32}^*\} + \Im\{s_{31}s_{41}^*\}\right)I \quad + \left(\Re\{s_{42}s_{31}^*\} - \Re\{s_{32}s_{41}^*\}\right)V \end{aligned} \tag{1.21}$$

In matrix form:

$$\begin{aligned} \begin{bmatrix} Q_m \\ U_m \end{bmatrix} = & \begin{bmatrix} \frac{1}{2}\left(|s_{42}|^2 - |s_{32}|^2 + |s_{31}|^2 - |s_{41}|^2\right) & \Re\{s_{41}s_{42}^*\} - \Re\{s_{31}s_{32}^*\} \\ -\Im\{s_{42}s_{32}^*\} - \Im\{s_{31}s_{41}^*\} & \Im\{s_{32}s_{41}^*\} - \Im\{s_{42}s_{31}^*\} \end{bmatrix} \cdot \begin{bmatrix} Q \\ U \end{bmatrix} \\ + & \begin{bmatrix} \frac{1}{2}\left(|s_{42}|^2 - |s_{32}|^2 - |s_{31}|^2 + |s_{41}|^2\right) & -\Im\{s_{41}s_{42}^*\} + \Im\{s_{31}s_{32}^*\} \\ -\Im\{s_{42}s_{32}^*\} + \Im\{s_{31}s_{41}^*\} & \Re\{s_{42}s_{31}^*\} - \Re\{s_{32}s_{41}^*\} \end{bmatrix} \cdot \begin{bmatrix} I \\ V \end{bmatrix} \end{aligned} \tag{1.22}$$

The previous expression put in evidence that the received Q_m and U_m are not only proportional to Q and U but they are a linear combination, in general, of all the incident ones. In order to obtain a compact form of Eq. (1.22), we define two matrices $\mathbf{H}$ and $\mathbf{K}$:

$$\mathbf{H} = \begin{bmatrix} H_{QQ} & H_{QU} \\ H_{UQ} & H_{UU} \end{bmatrix} \tag{1.23}$$

where:

$$\begin{aligned} H_{QQ} &= \frac{1}{2}\left(|s_{42}|^2 - |s_{32}|^2 + |s_{31}|^2 - |s_{41}|^2\right) \\ H_{QU} &= \Re\{s_{41}s_{42}^*\} - \Re\{s_{31}s_{32}^*\} \\ H_{UQ} &= -\Im\{s_{42}s_{32}^*\} - \Im\{s_{31}s_{41}^*\} \\ H_{UU} &= \Im\{s_{32}s_{41}^*\} - \Im\{s_{42}s_{31}^*\} \end{aligned}$$

and

$$\mathbf{K} = \begin{bmatrix} K_{QI} & K_{QV} \\ K_{UI} & K_{UV} \end{bmatrix} \tag{1.24}$$

where:

$$\begin{aligned} K_{QI} &= \frac{1}{2}\left(|s_{42}|^2 - |s_{32}|^2 - |s_{31}|^2 + |s_{41}|^2\right) \\ K_{QV} &= -\Im\{s_{41}s_{42}^*\} + \Im\{s_{31}s_{32}^*\} \\ K_{UI} &= -\Im\{s_{42}s_{32}^*\} + \Im\{s_{31}s_{41}^*\} \\ K_{UV} &= \Re\{s_{42}s_{31}^*\} - \Re\{s_{32}s_{41}^*\} \end{aligned}$$

Then Eq.(1.22) becomes

$$\begin{bmatrix} Q_m \\ U_m \end{bmatrix} = \mathbf{H} \cdot \begin{bmatrix} Q \\ U \end{bmatrix} + \mathbf{K} \cdot \begin{bmatrix} I \\ V \end{bmatrix} \tag{1.25}$$

From Eq.(1.25) it is clear that the Q_m and U_m are affected by the other stokes parameters I and V through the matrix $\mathbf{K}$. Ideally the elements of this matrix should be zero and this can be achieved as proposed in [21], so in this way Q_m and U_m will not be contaminated from I and V. Moreover we would like to have $Q_m = Q$ and $U_m = U$, i.e. the matrix $\mathbf{H}$ equal to the identity one.

In the case of perfect symmetry of th polarizer such that the cross coupling among electrical ports 1 and 4 or among electrical ports 2 and 3 in the principal basis can be neglected (i.e. $s_{41} = s_{32} = 0$), Eq.(1.22) reduces to:

$$\begin{aligned} \begin{bmatrix} Q_m \\ U_m \end{bmatrix} = & \begin{bmatrix} \frac{1}{2}\left(|s_{42}|^2 + |s_{31}|^2\right) & 0 \\ 0 & -\Im\{s_{42}s_{31}^*\} \end{bmatrix} \cdot \begin{bmatrix} Q \\ U \end{bmatrix} \\ + & \begin{bmatrix} \frac{1}{2}\left(|s_{42}|^2 - |s_{31}|^2\right) & 0 \\ 0 & \Re\{s_{42}s_{31}^*\} \end{bmatrix} \cdot \begin{bmatrix} I \\ V \end{bmatrix} \end{aligned} \tag{1.26}$$

From Eq.(1.26) it is clear that matrix $\mathbf{K}$ is equal to zero when $|s_{42}| = |s_{31}|$ and the product $s_{42}s_{31}^* = |s_{42}||s_{31}|e^{j(\angle s_{42} - \angle s_{31})}$ is purely imaginary, i.e. $\angle s_{42} - \angle s_{31} = (2n+1)\,\pi/2$. This means the magnitude difference of the transmission terms s_{42} and s_{31} affects the Q_m, while the phase difference $\angle s_{42} - \angle s_{31}$ acts on U_m.

Chapter 2

Polarizer Design

2.1 Introduction

The CMBR is an electromagnetic radiation that fills the Universe. In principle, the polarization of the CMBR could be measured by means of one single polarimeter. As a matter of fact, since the incoming radiation is quite faint, arrays of polarimeters are currently used in order to increase instrument sensitivity. Recent astrophysical experiments based on arrays of polarimeters aimed at the detection of the CMBR polarization state are QUIET [6], LSPE [7] and QUIJOTE [8, 9]. The measurement accuracy mainly depends on the performance of the polarimeter's building blocks, e.g. antennas, polarizers, OMTs and LNAs. Since arrays containing tens or hundreds of polarimeters are used for CMBR measurement, the manufacturing of each polarimeter building block should be compatible with a large-scale production.

In this chapter, a novel design of the polarizer is proposed. As described in the previous chapter, the principle of the polarizer is to provide $\frac{\pi}{2}$ differential phase shift($\mathbf{\Phi}$) between its inductive and capacitive transmission coefficient. This goal can be achieved in various manners for wide or narrow frequency band. For instance circular-rectangular waveguide polarizer [22], grooved circular waveguide polarizer [23], polarizer via optimum iris concept [18], circular ridged waveguide polarizer [24] and polarizer by means of elliptical irises design with an hierarchical optimization approach [19] can be found in the indicated literature. Corrugated circular-rectangular waveguide polarizer, grooved circular waveguide polarizers, ridge circular waveguide polarizers and circular waveguide polarizers with optimum-iris-set are reported in figure 2.1 (a), (b), (c) and (d) respectively. An efficient tool is reported in [25] in order to design a polarizer by employing irises.

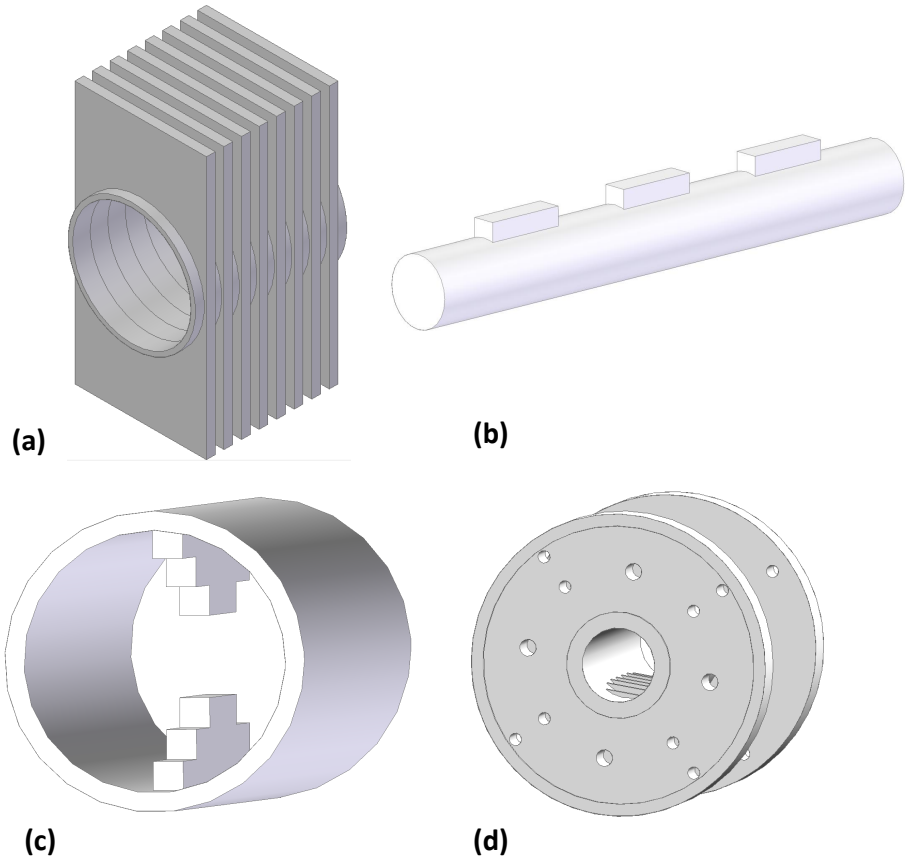

Figure 2.1. Various kind of waveguide polarizers. (a) Corrugated circular-rectangular waveguide polarizer. (b) Grooved circular waveguide polarizer. (c) Ridge circular waveguide polarizer. (d) Circular waveguide polarizer with optimum-iris-set. (All designs are not scaled).

In [22] quasi-stub and in [23] stub polarizers are proposed. The main advantage of the stub polarizer configuration is related to its simple design, compactness and low weight. In principle, one of the benefits of the stub configuration with respect to the iris one is the low reflection coefficient and insertion loss introduced by a single stub. As a consequence, the structure is less sensitive to mechanical tolerance. Since stub polarizers have a symmetrical structure, it also avoids the excitation of higher order modes. In addition to that, the use of platelet technology by wire spark erosion technique makes this solution particularly suitable for mass production.

In the present chapter we consider the design of a W-band polarizer operating at $[85, 104]$ GHz. The polarizer waveguide is set to be circular in order to avoid the employment of transitions for the connection, on one side, with the horn antenna and, on the other side, with the OMT. We start by considering the configuration proposed

in [23] putting in evidence the limits of this solution if platelet technology manufacturing is considered. Subsequently, a new configuration is introduced, discussed and applied to the design of a high performance polarizer. An extensive sensitivity analysis has been carried out in order to show the applicability of the platelet technology to the design under consideration. Two prototypes have been manufactured. Their geometry has been validated by means of a dedicated microscope. Finally, they have been measured by a Vector Network Analyzer (VNA) confirming the validity of the proposed configuration. The performances are reported in the last section of this chapter.

The device has been analyzed exploiting a Spectral-Element Method (SEM) [26] code whose MATLAB® [27] version has been parallelized as explained in chapter 5. The results have been validated by comparison with the two commercial softwares Ansys HFSS (HFSS) [28] and CST Micro Wave Studio Suite (CST-MWS) [29].

2.2 Single-Fold-Stub (SFS) Polarizer

The idea of a SFS solution ([23]) is to insert a symmetric stub along one of the principal axis of the circular waveguide as shown in Fig. 2.2. The stub produces a different behavior between the two polarizations[1] of the TE_{11} mode. In particular the stub height h affects considerably the horizontal polarization while leaves unperturbed the vertical one. This fact is verified by considering Fig. 2.3 where the critical constants k_t^V and k_t^H for the vertical and horizontal polarizations of the TE_{11}-like modes of the stub cross-section are reported as a function of the height h. In the plot the circular waveguide diameter D and the stub width w are fixed and equal to $2.62\,\text{mm}$ and $1\,\text{mm}$, respectively. As shown in the Fig. 2.3, while the vertical polarization critical constant k_t^V is almost unperturbed[2] as h varies, the horizontal one k_t^H decreases monotonically as a function of h. As a consequence the horizontal polarization propagate in delay with respect the vertical one. This analysis shows that the stub has a capacitive behavior for the horizontal polarization and an inductive for the vertical polarization. In order to avoid confusion, hereafter we refer the TE_{11} polarizations as capacitive and inductive. The desirable feature of employment platelet technology for the polarizer fabrication in order to reduce the costs in perspective of mass production, force to use layers of the same thickness. Among the available commercial values, $3\,\text{mm}$ thickness layers are a good compromise between manufacture robustness and overall weight of the device. Also from an electrical point of view this choice is promising, since in the W-band the free-space

[1] with reference to Fig. 2.2 we call *vertical* and *horizontal* polarizations the cases where the TE_{11} mode is directed along the y and x directions, respectively.

[2] actually it slowly increases as a function of h.

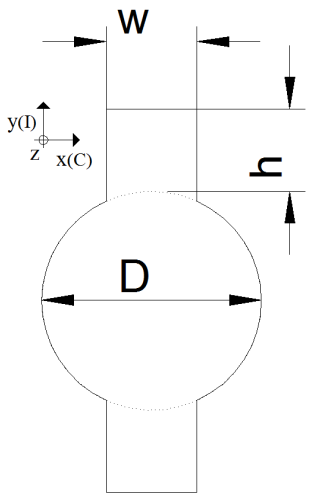

Figure 2.2. Geometry and relevant parameters of a Single-Fold-Stub (SFS).

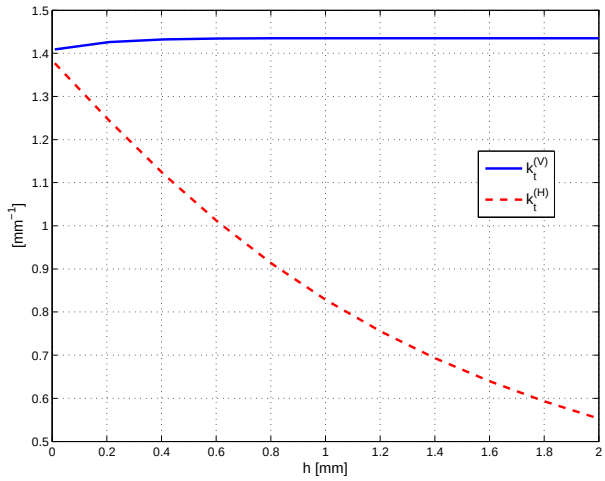

Figure 2.3. Critical constants k_t^V and k_t^H for the vertical and horizontal polarizations of the TE_{11}-like modes in the stub cross-section as a function of the height h. In the plot the circular waveguide diameter D and the stub width w are fixed and equal to 2.62 mm and 1 mm, respectively.

wavelength is almost 3 mm and, hence, higher-order mode interaction in the cavity formed by two subsequent stubs is negligible.

The desired 90° differential phase shift among the two polarizations can be obtained by using one or a cascade of SFS. As discussed in the introduction, the common circular waveguide diameter is fixed and equal to 2.62 mm. The design parameters are then the width w and heights h of the stubs. These can be determined by exploiting the design maps reported in Fig. 2.4–2.7 that show, as a function of the w and h, the average differential phase shift ($\overline{\Phi}$), the reflection coefficients for the

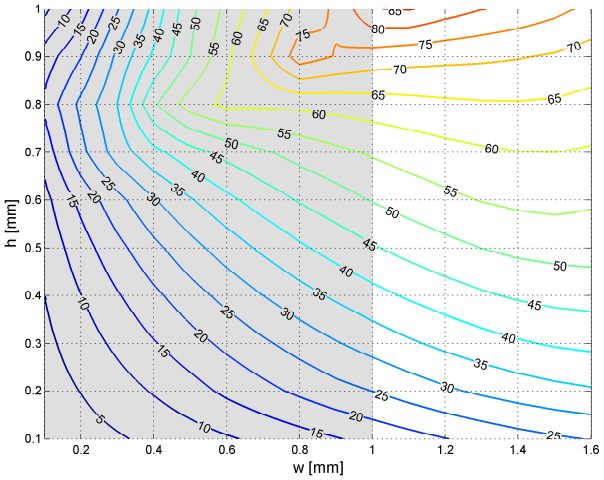

Figure 2.4. Average differential phase shift ($\overline{\Phi}$) between the two TE_{11} mode polarizations as a function of the width (w) and height (h) for only one SFS. The diameter D is equal to 2.62 mm. The considered frequency band is [85, 104] GHz. The gray area represents the forbidden region.

inductive ($s_{11}^{(I)}$) and capacitive ($s_{11}^{(C)}$) polarizations and the relative differential phase error ($\epsilon_{\Delta\Phi}$). The plots refer to the operative frequency band under consideration, i.e. [85,104] GHz. For manufacture feasibility, the width w has to be greater or equal to 1 mm. There are in the plots, some parts where SFS width(w)do not satisfy this requirement therefore it is labeled as *forbidden* region and highlighted by a gray color. This choice would be taken into account in all the designs proposed in this thesis.

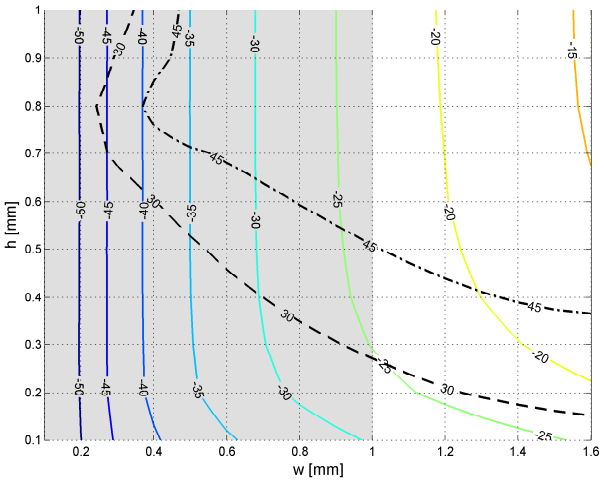

Figure 2.5. Maximum reflection coefficient for the inductive polarization ($s_{11}^{(I)}$) as a function of the width (w) and height (h) for only one SFS. The diameter D is equal to 2.62 mm. The considered frequency band is [85, 104] GHz. The gray area represents the forbidden region. The black dash lines indicate the iso-level curves on which the average differential phase shift is fixed at 30° and 45°, respectively (see Fig. 2.4).

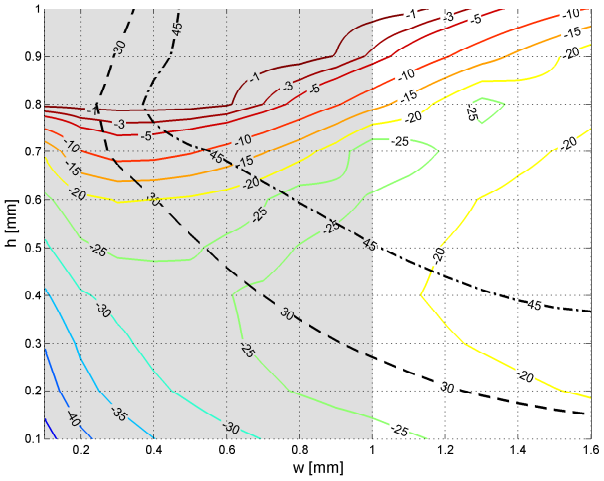

Figure 2.6. Maximum reflection coefficient for the capacitive polarization ($s_{11}^{(C)}$) as a function of the width (w) and height (h) for only one SFS. The diameter D is equal to 2.62 mm. The considered frequency band is [85, 104] GHz. The gray area represents the forbidden region. The black dash lines indicate the iso-level curves on which the average differential phase shift is fixed at 30° and 45°, respectively (see Fig. 2.4).

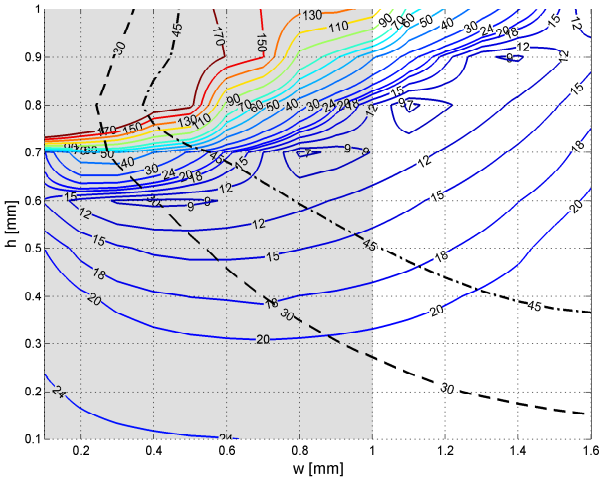

Figure 2.7. Relative differential phase error ($\epsilon_{\Delta\phi}$) as a function of the width (w) and height (h) for only one SFS. The diameter D is equal to 2.62 mm. The considered frequency band is [85, 104] GHz. The gray area represents the forbidden region.The black dash lines indicate the iso-level curves on which the average differential phase shift is fixed at 30° and 45°, respectively (see Fig. 2.4).

Exploiting these design charts, different polarizer solutions have been investigated. The simplest one consists on a single stub polarizer. In this case the single stub has to introduce the desired 90° differential phase shift(Φ). Among the possible solution we choose the width(w) and the height(h) equal to 1.471 mm and 0.953 mm, respectively. This choice represents the best compromise between the minimum relative differential phase error $\epsilon_{\Delta\phi}$ and the lowest reflection coefficients. Unfortunately, the performances are not good: $s_{11}^{(I)} \leq -16\,\text{dB}$, $s_{11}^{(C)} \leq -13\,\text{dB}$ and $\epsilon_{\Delta\phi} \approx 22.4\,\%$.

The case of a polarizer with two SFS has, then, been investigated and in particular a symmetric configuration has been considered. In this case, the two identical stubs have been designed to introduce a 45° differential phase shift(Φ) and the best solution is represented by a width(w) and an height(h) equal to 1 mm and 0.524 mm, respectively (see the dash-dotted-line on Fig. 2.5, 2.6 and 2.7). The performances are slightly better than single stub case but still unfortunately not significant: $s_{11}^{(I)} \leq -17.9\,\text{dB}$, $s_{11}^{(C)} \leq -16.3\,\text{dB}$ and $\epsilon_{\Delta\phi} \approx 15.3\,\%$.

Finally a three stubs symmetric configuration has been considered. In this case we have first fixed all the stubs identical and producing a 30° differential phase shift(Φ) (see the dashed lines on Fig. 2.5, 2.6 and 2.7). The polarizer performances are then refined using an optimization procedure[3]. The final widths are 1 mm for all the stubs, the first and last height of the stub are 0.1 mm and the central one is

[3]classical optimization algorithm [30].

0.694 mm. Although the performances are better than the other cases but still not satisfactory: $s_{11}^{(I)} \leq -17.7\,\text{dB}$, $s_{11}^{(C)} \leq -18.7\,\text{dB}$ and $\epsilon_{\Delta\phi} \approx 10.5\,\%$.

Tables 2.1, 2.2 and 2.3, summarize the reachable performances and the relevant geometries. In all these designs the stubs and cavity lengths have been fixed to 3 mm and the diameter(D) equal to 2.62 mm, for this reason these designs are referred as *constrained* cases.

In order to consider the effect of this limitation, we have repeated the three designs by neglecting the constrains on the lengths. In all these cases an optimization algorithm has been exploited using as starting point the relevant *constrained* geometries. Significant improvements in the polarizer performances can be observed in these cases. Tables 2.1, 2.2 and 2.3 show the relevant geometries and the performances comparison between *constrained* and *unconstrained* cases. This study has put in evidence the significant effect of thickness layer constraint the performance and shows that for low cost mass production in W-band the SFS configuration is not promising.

	Unit	1-stub cont. pol	1-stub uncont. pol
D	[mm]	2.62	2.418
w_k	[mm]	1.471	1
h_k	[mm]	0.953	0.91
$L_k^{(stub)}$	[mm]	3	3.067
$L_k^{(cav)}$	[mm]	-	-
$s_{11}^{(I)}$	[dB]	-16	-21.6
$s_{11}^{(C)}$	[dB]	-13	-22.6
XPR	[dB]	-18.2	-25.5
XPT	[dB]	-14.9	-24.7
$\Delta\Phi$	[deg]	20.2	6.7
$\epsilon_{\Delta\Phi}$	[%]	22.4	7.4

Table 2.1. Geometry and electrical performances comparison between the SFS constrained and unconstrained polarizers with one stub.

	Unit	2-stub const. pol		2-stub unconst. pol	
D	[mm]	2.62		2.7	
$w_k^{(I)}$	[mm]	1	1	1	1
$h_k^{(I)}$	[mm]	0.524	0.524	0.606	0.606
$L_k^{(stub)}$	[mm]	3	3	2.92	2.92
$L_k^{(cav)}$	[mm]	3		3.966	
$s_{11}^{(I)}$	[dB]	-17.9		-22.6	
$s_{11}^{(C)}$	[dB]	-16.3		-23.6	
XPR	[dB]	-20.4		-28.5	
XPT	[dB]	-18.4		-25.6	
$\Delta\Phi$	[deg]	13.7		6	
$\epsilon_{\Delta\Phi}$	[%]	15.3		6.6	

Table 2.2. Geometry and electrical performances comparison between the SFS constrained and unconstrained polarizers with two stubs.

	Unit	3-stub const. pol.			3-stub unconst. pol.		
D	[mm]	2.62			2.724		
$w_k^{(I)}$	[mm]	1	1	1	1	1.067	1
$h_k^{(I)}$	[mm]	0.1	0.694	0.1	0.611	0.1	0.611
$L_k^{(stub)}$	[mm]	3	3	3	2.87	1	2.87
$L_k^{(cav)}$	[mm]	3	3		4.158	4.158	
$s_{11}^{(I)}$	[dB]	-17.7			-23.3		
$s_{11}^{(C)}$	[dB]	-18.7			-24.3		
XPR	[dB]	-22			-27.4		
XPT	[dB]	-21.6			-26.3		
$\Delta\Phi$	[deg]	9.4			5.5		
$\epsilon_{\Delta\Phi}$	[%]	10.5			6.1		

Table 2.3. Geometry and electrical performances comparison between the SFS constrained and unconstrained polarizers with three stubs.

2.3 Dual-Fold-Stub (DFS) Polarizer

The limitation of the SFS configuration where fixed thickness layers are employed and manufacturing constrains are considered, can be overcome by introducing additional degrees of freedom in the design. For this purpose we have investigated a new stub configuration, called *dual fold*, which consist of two arms along the principal axes of the circular waveguide (see Fig. 2.8). The superscripts C and I refer to the inductive and capacitive axes as discussed in the previous section. As in the SFS design, this configuration is two folded symmetric (i.e. it exhibits two symmetry axes), therefore, in the case of ideal realization of the structure, the first higher mode excited by an incident TE_{11} mode is the TM_{11}. In DFS configuration the design parameters are the two widths (i.e. $w^{(I)}$ and $w^{(C)}$) and the two heights (i.e. $h^{(I)}$ and $h^{(C)}$). The remaining parameters, i.e. the circular waveguide diameter(D) and the

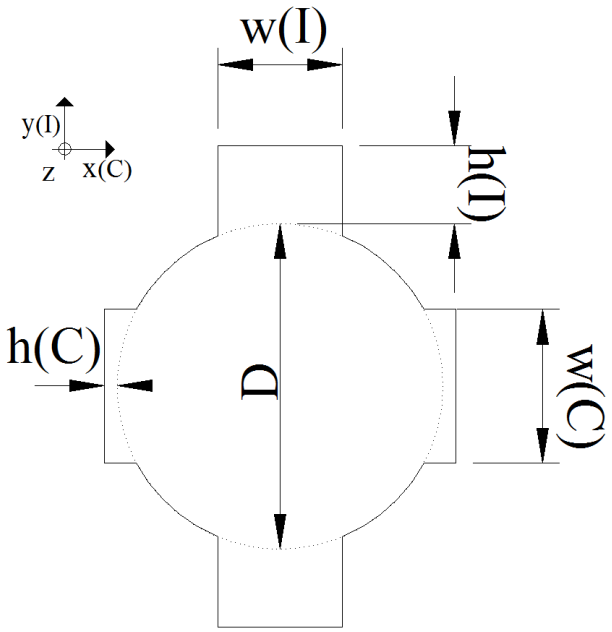

Figure 2.8. Geometry and relevant parameters of a Dual-Fold-Stub (DFS). The figure shows also the *inductive* and *capacitive* axes.

stub and cavities lengths, are fixed and equal to 2.62 mm and 3 mm, respectively, exactly like the SFS *constrained* case.

The derivation of DFS characteristics as a function of the geometry is more complicated with respect to the SFS ones since the two additional design parameters have to be considered. However it should be noted that the capacitive arm is introduced in order to compensate the layer thickness constraints so they operate for refinement purpose. Exploiting this idea we generalized the plots shown in Fig. 2.4–2.7 for the SFS case. For each couple $(w^{(I)}, h^{(I)})$, we determine, through optimization, the capacitive arm geometry which minimizes the relative differential phase error($\epsilon_{\Delta\Phi}$) in the frequency band [85,104] GHz. We refer to these specific values of $w^{(C)}$ and $h^{(C)}$ as the *optimum* ones. They are reported in Fig. 2.9 and 2.10, respectively. The relevant relative differential phase error($\epsilon_{\Delta\Phi}$), the average differential phase shift ($\overline{\Phi}$) and the inductive and capacitive reflections coefficients are reported in Fig. 2.11, 2.12, 2.13 and 2.14, respectively. In order to take into account the manufacturing limitations[4] already discussed, the plots have been divided in four different regions labeled in roman numerals **I-IV**. The geometries that belong to region **I-III** can not be considered in the design since one or both the stub widths $w^{(I)}$ and $w^{(C)}$ would be lower than 1 mm, hence only the configuration in region *IV* can be used in the

[4] i.e. the stub width can not be lower than 1 mm.

design. From the plots it can be observed that DFS presents considerable good performances[5] if geometries providing an average differential phase shift($\overline{\Phi}$) lower than 30° are addressed.

This feature is not present in SFS configuration and this, indeed, represents the main advantages of DFS. The simplest and shortest solution is the employment of three identical stubs which produces 30° differential phase shift(Φ) each. Among the possible solutions the best compromise between low reflection coefficient and minimum relative differential phase error($\epsilon_{\Delta\Phi}$) is represented by $w^{(I)} = 1.216\,\text{mm}$, $h^{(I)} = 0.705\,\text{mm}$ (and as a consequence $w^{(C)} = 1\,\text{mm}$ and $h^{(C)} = 0.257\,\text{mm}$). This geometry is indicated by a green square in Fig. 2.9–2.14. The reflection coefficients $s_{11}^{(I)}$, $s_{11}^{(C)}$, the XPT and XPR and the relative differential phase errors for this configuration are shown in Fig. 2.15–2.19, respectively. The performances are quite satisfying, however they have been refined exploiting an optimization procedure. The geometry and the performance of the pre and post optimization solutions are listed in Table 2.4.

Fig. 2.20–2.25 show the performances of the optimized solution computed exploiting the SEM code and two commercial software HFSS and CST-MWS. The excellent accordance among the curves confirms the validity of the proposed configuration. As it can be observed in these plots, the final solution presents significant good performance both in terms of reflection coefficients (lower than $-30\,\text{dB}$) and in the cross-polarization terms (XPT and XPR lower than $-35\,\text{dB}$ and $-33\,\text{dB}$, respectively), finally, the differential phase shift is in the range $[88^\circ,92^\circ]$.

[5] reflection coefficients and relative differential phase errors ($\epsilon_{\Delta\Phi}$) lower than $-30\,\text{dB}$ and $3\,\%$, respectively.

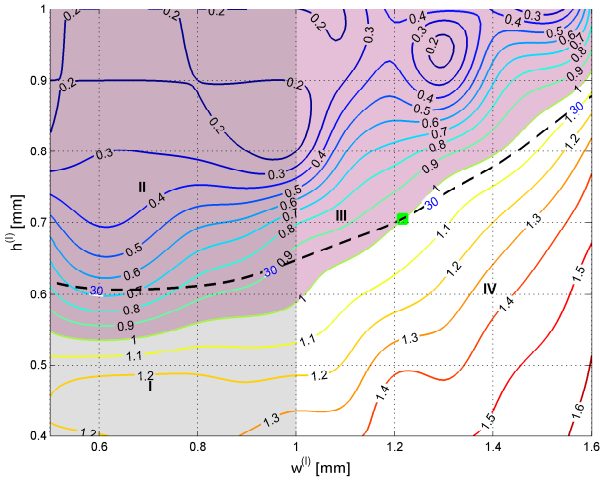

Figure 2.9. Optimum value of $w^{(C)}$ as a function of $w^{(I)}$ and $h^{(I)}$ (see Fig. 2.8) for a single DFS. The diameter D is equal to 2.62 mm. The considered frequency band is [85,104] GHz. The gray areas represent the forbidden region. The black dash line indicates the iso-level curves on which the average differential phase shift is fixed at 30° (see Fig. 2.12).

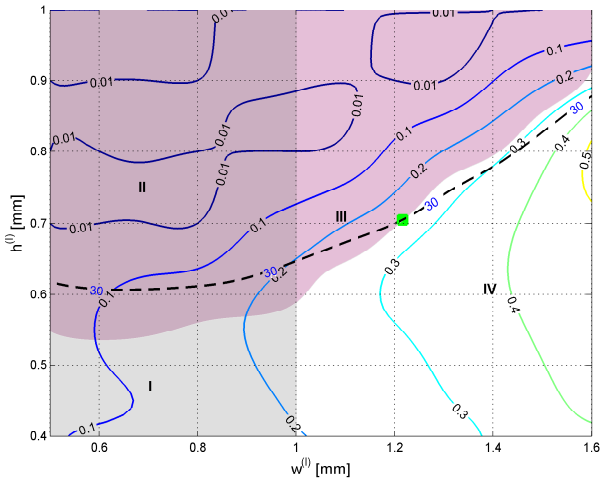

Figure 2.10. Optimum value of $h^{(C)}$ as a function of $w^{(I)}$ and $h^{(I)}$ (see Fig. 2.8) for a single DFS. The diameter D is equal to 2.62 mm. The considered frequency band is [85,104] GHz. The gray areas represent the forbidden region. The black dash line indicates the iso-level curves on which the average differential phase shift is fixed at 30° (see Fig. 2.12).

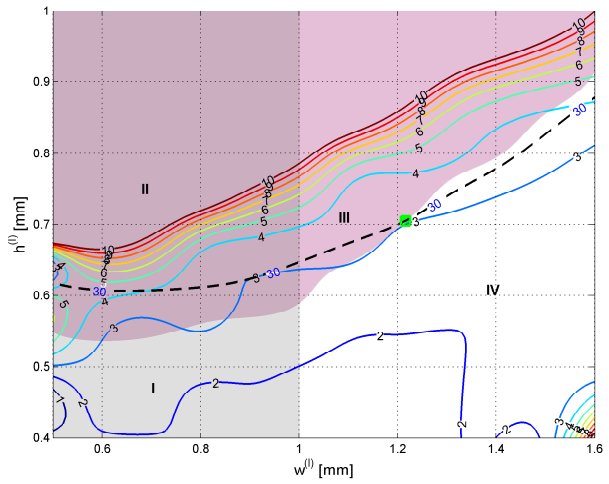

Figure 2.11. Relative differential phase error($\epsilon_{\Delta\Phi}$) as a function of $w^{(I)}$ and $h^{(I)}$ (see Fig. 2.8) for a single DFS. The diameter D is equal to 2.62 mm. The considered frequency band is [85,104] GHz. The gray areas represent the forbidden region. The black dash line indicates the iso-level curves on which the average differential phase shift is fixed at 30° (see Fig. 2.12).

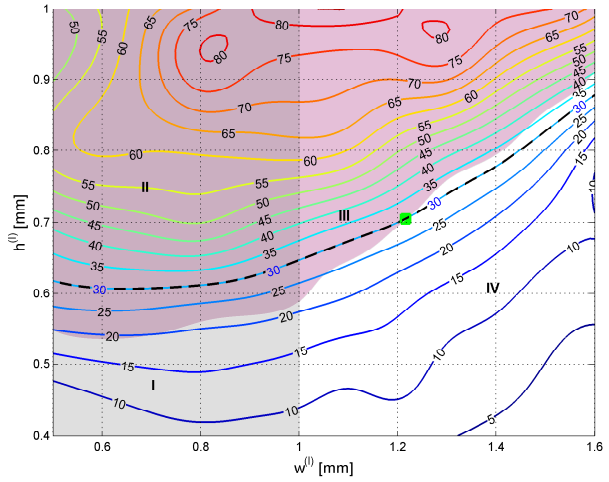

Figure 2.12. Average differential phase shift($\overline{\Phi}$)between the capacitive and inductive polarizations as a function of $w^{(I)}$ and $h^{(I)}$ (see Fig. 2.8) for a single DFS. The diameter D is equal to 2.62 mm. The considered frequency band is [85,104] GHz. The gray areas represent the forbidden region. The black dash line indicates the iso-level curves on which the average differential phase shift is fixed at 30°.

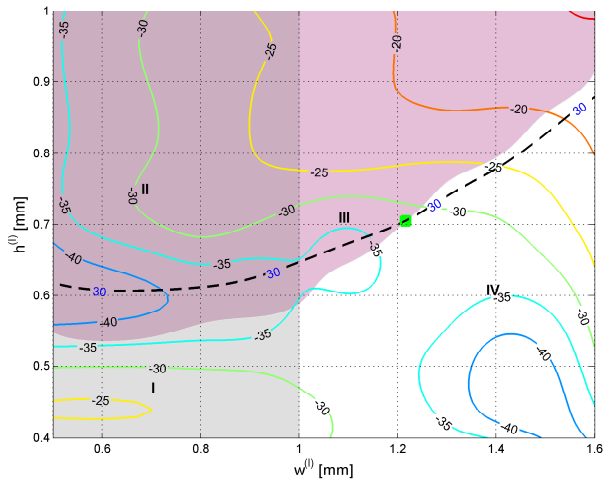

Figure 2.13. Maximum reflection coefficient for the inductive($s_{11}^{(I)}$) polarization as a function of $w^{(I)}$ and $h^{(I)}$ (see Fig. 2.8) for a single DFS. The diameter D is equal to 2.62 mm. The considered frequency band is [85,104] GHz. The gray areas represent the forbidden region. The black dash line indicates the iso-level curves on which the average differential phase shift is fixed at 30° (see Fig. 2.12).

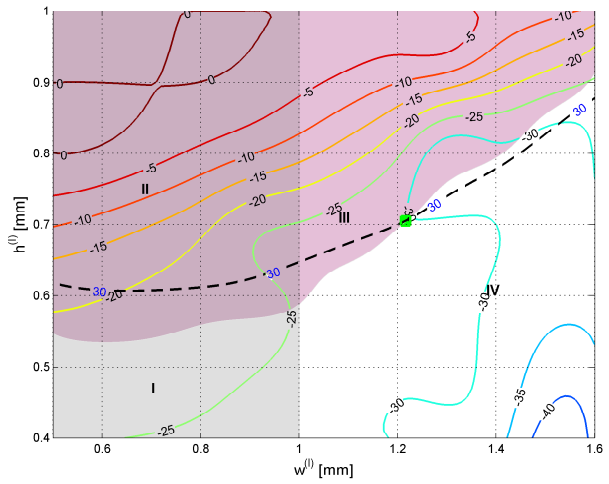

Figure 2.14. Maximum reflection coefficient for the capacitive($s_{11}^{(C)}$) polarization as a function of $w^{(I)}$ and $h^{(I)}$ (see Fig. 2.8) for a single DFS. The diameter D is equal to 2.62 mm. The considered frequency band is [85,104] GHz. The gray areas represent the forbidden region. The black dash line indicates the iso-level curves on which the average differential phase shift is fixed at 30° (see Fig. 2.12).

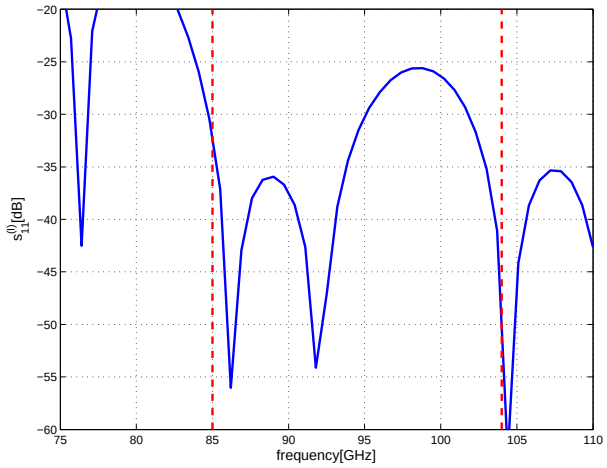

Figure 2.15. Reflection coefficient $s_{11}^{(I)}$ of the inductive polarization as a function of the frequency for the pre-optimization three-DFS polarizer in 20% bandwidth centered at 94.5 GHz. The vertical dashed-lines indicate the operative frequency band. The polarizer geometry is reported in Table 2.4.

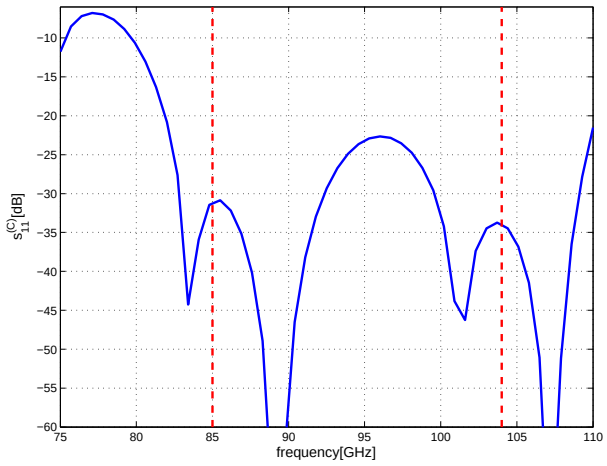

Figure 2.16. Reflection coefficient $s_{11}^{(C)}$ of the capacitive polarization as a function of the frequency for the pre-optimization three-DFS polarizer in 20% bandwidth centered at 94.5 GHz. The vertical dashed-lines indicate the operative frequency band. The polarizer geometry is reported in Table 2.4.

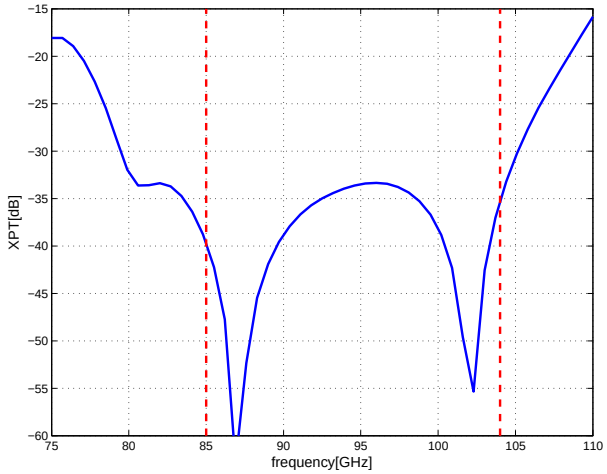

Figure 2.17. Cross Polarization in Transmission (XPT) as a function of the frequency for the pre-optimization three-DFS polarizer in 20% bandwidth centered at 94.5 GHz. The vertical dashed-lines indicate the operative frequency band. The polarizer geometry is reported in Table 2.4.

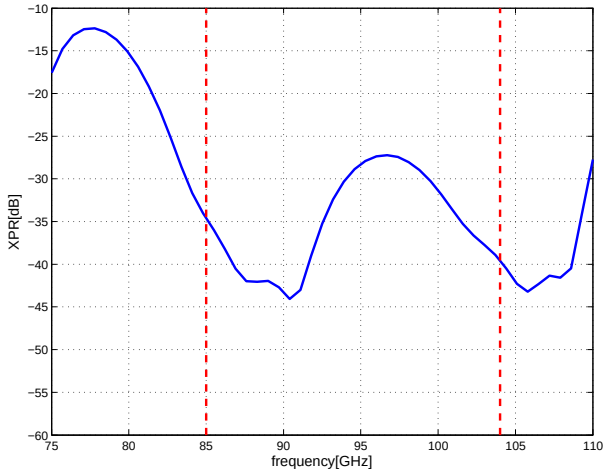

Figure 2.18. Cross Polarization in Reflection (XPR) as a function of the frequency for the pre-optimization three-DFS polarizer in 20% bandwidth centered at 94.5 GHz. The vertical dashed-lines indicate the operative frequency band. The polarizer geometry is reported in Table 2.4.

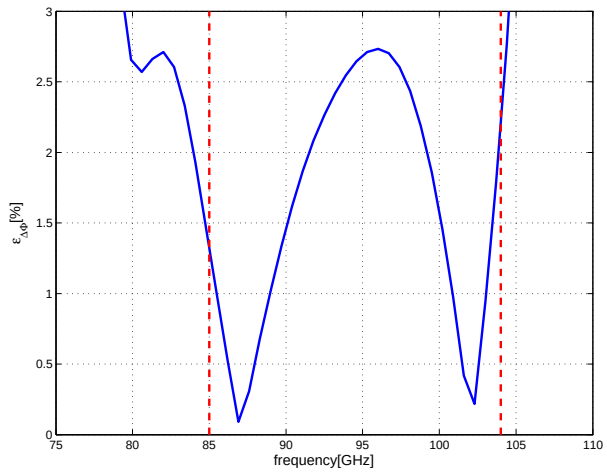

Figure 2.19. Relative differential phase error($\epsilon_{\Delta\Phi}$) as a function of the frequency for the pre-optimization three-DFS polarizer in 20% bandwidth centered at 94.5 GHz. The vertical dashed-lines indicate the operative frequency band. The polarizer geometry is reported in Table 2.4.

	Unit	Pre opt. DFS Pol			Post opt. DFS Pol		
D	[mm]	2.62			2.62		
$w_k^{(I)}$	[mm]	1.216	1.216	1.216	1	1	1
$h_k^{(I)}$	[mm]	0.705	0.705	0.705	0.624	0.614	0.624
$w_k^{(C)}$	[mm]	1	1	1	1.238	1.425	1.238
$h_k^{(C)}$	[mm]	0.257	0.257	0.257	0.1	0.122	0.1
$L_k^{(stub)}$	[mm]	3	3	3	3	3	3
$L_k^{(cav)}$	[mm]	3	3		3	3	
$s_{11}^{(I)}$	[dB]	-25.597			-36.558		
$s_{11}^{(C)}$	[dB]	-22.644			-30.885		
XPR	[dB]	-27.219			-36.571		
XPT	[dB]	-33.357			-35.421		
$\Delta\Phi$	[deg]	2.459			1.941		
$\epsilon_{\Delta\Phi}$	[%]	2.733			2.157		

Table 2.4. Geometry and electrical performances comparison between the pre- and post-optimization DFS polarizers with three stubs.

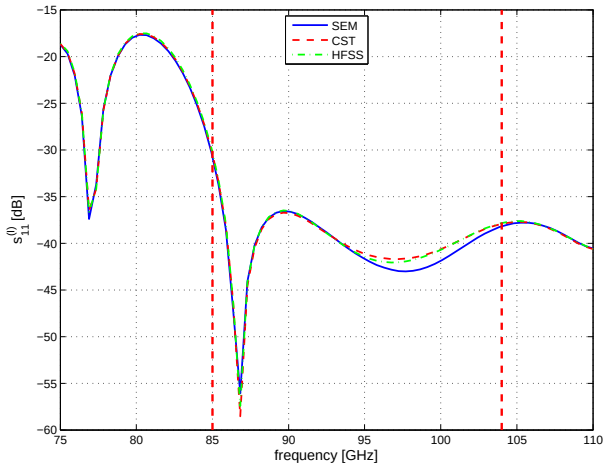

Figure 2.20. Reflection coefficient of the inductive polarization($s_{11}^{(I)}$) as a function of the frequency for the optimum three-DFS polarizer in 20% bandwidth centered at 94.5 GHz. Solid, dashed and dot-dashed lines refer to SEM, CST-MWS and HFSS simulations, respectively. The vertical dashed-lines indicate the operative frequency band. The polarizer geometry is reported in Table 2.4.

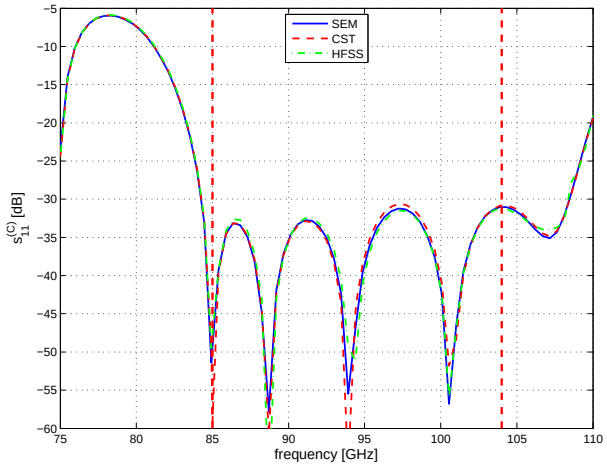

Figure 2.21. Reflection coefficient of the capacitive polarization($s_{11}^{(C)}$) as a function of the frequency for the optimum three-DFS polarizer in 20% bandwidth centered at 94.5 GHz. Solid, dashed and dot-dashed lines refer to SEM, CST-MWS and HFSS simulations, respectively. The vertical dashed-lines indicate the operative frequency band. The polarizer geometry is reported in Table 2.4.

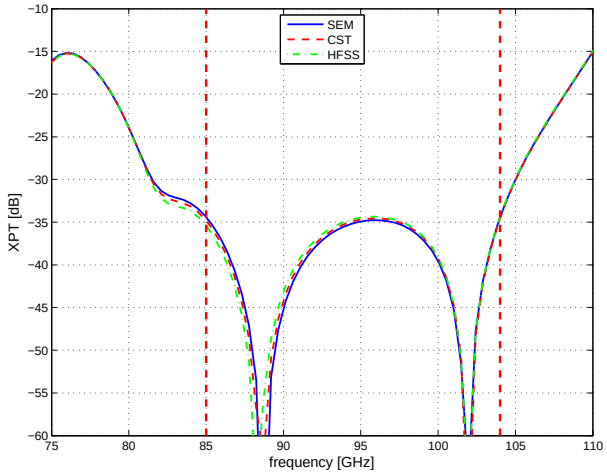

Figure 2.22. Cross Polarization in Transmission (XPT) as a function of the frequency for the optimum three-DFS polarizer in 20% bandwidth centered at 94.5 GHz. Solid, dashed and dot-dashed lines refer to SEM, CST-MWS and HFSS simulations, respectively. The vertical dashed-lines indicate the operative frequency band. The polarizer geometry is reported in Table 2.4.

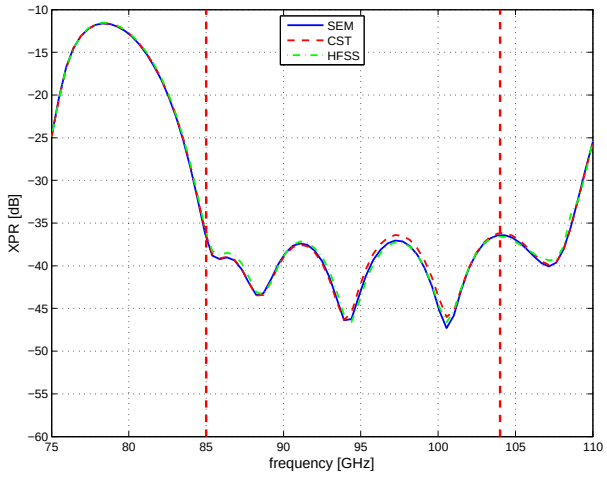

Figure 2.23. Cross Polarization in Reflection (XPR) as a function of the frequency for the optimum three-DFS polarizer in 20% bandwidth centered at 94.5 GHz. Solid, dashed and dot-dashed lines refer to SEM, CST-MWS and HFSS simulations, respectively. The vertical dashed-lines indicate the operative frequency band. The polarizer geometry is reported in Table 2.4.

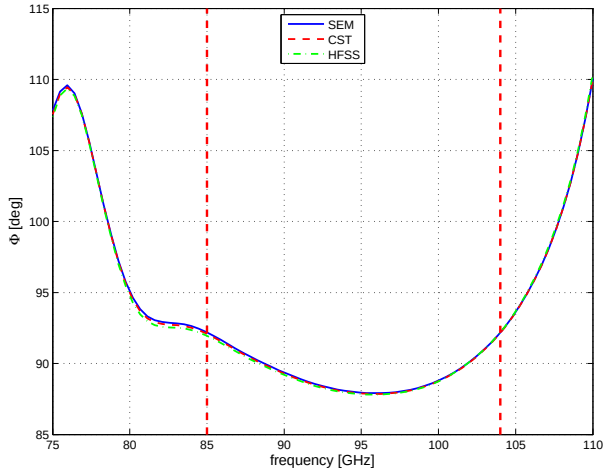

Figure 2.24. Differential phase shift(Φ) as a function of the frequency for the optimum three-DFS polarizer in 20% bandwidth centered at 94.5 GHz. Solid, dashed and dot-dashed lines refer to SEM, CST-MWS and HFSS simulations, respectively. The vertical dashed-lines indicate the operative frequency band. The polarizer geometry is reported in Table 2.4.

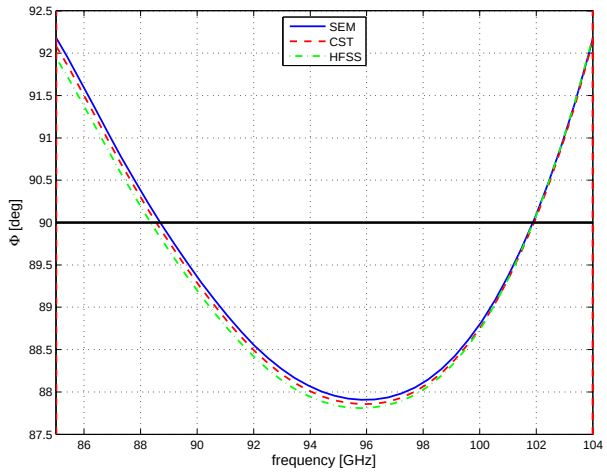

Figure 2.25. Differential phase shift(Φ) in *operative band* as a function of the frequency for the optimum three-DFS polarizer in 20% bandwidth centered at 94.5 GHz. Solid, dashed and dot-dashed lines refer to SEM, CST-MWS and HFSS simulations, respectively. The vertical dashed-lines indicate the operative frequency band. The polarizer geometry is reported in Table 2.4.

2.3.1 Analysis of the Constraints Effects on the Design

It is important to understand the effect of the constraints imposed on the design, i.e. the diameter dimension D and the lengths of the stubs ($L_k^{(stub)}$) and cavities($L_k^{(cav)}$). For this purpose three different polarizer solutions (with one, two and three stubs) have been considered and compared with the relevant *constrained* cases in the same way discussed for the SFS configuration at the end of section 2.2. In Tables 2.5, 2.6 and 2.7 the geometrical and electrical parameters are reported for the one-, two- and three-stubs configurations.

The single stub case presents poor performances in both constrained an unconstrained configurations (see Table 2.5). In the case of two stubs, instead, the unconstrained solution is quite promising while the constrained one is still not satisfactory (see Table 2.6). This performances gap is minimized in the case of three stubs (see Table 2.7).

This analysis proves the validity of the DFS configuration with respect to the SFS structure, since the use of the DFS permits, indeed, to compensate the limitation imposed on the lengths of the stubs and cavities and, therefore, it is suitable for mass production using platelet technology with wire spark erosion technique. More complicated structures (with more stubs) have not been considered, since the constrained solution with three stubs is sufficient for the desired application while minimizing the mechanical complexity of the polarizer.

	Unit	1-stub const. pol.	1-stub unconst. pol.
D	[mm]	2.62	2.186
$w_k^{(I)}$	[mm]	1.52	1.31
$h_k^{(I)}$	[mm]	1.019	1.177
$w_k^{(C)}$	[mm]	1	1
$h_k^{(C)}$	[mm]	0.1	0.1
$L_k^{(stub)}$	[mm]	3	2.834
$L_k^{(cav)}$	[mm]	-	-
$s_{11}^{(I)}$	[dB]	-16.8	-20
$s_{11}^{(C)}$	[dB]	-8.7	-21
XPR	[dB]	-14.9	-25.1
XPT	[dB]	-10.7	-23
$\Delta\Phi$	[deg]	32.45	8.09
$\epsilon_{\Delta\Phi}$	[%]	36	8.9

Table 2.5. Geometry and electrical performances comparison between the DFS constrained and unconstrained polarizers with one stub.

	Unit	2-stub const. pol.		2-stub unconst. pol.	
D	[mm]	2.62		2.62	
$w_k^{(I)}$	[mm]	1.042	1.042	1	1
$h_k^{(I)}$	[mm]	0.75	0.75	0.624	0.624
$w_k^{(C)}$	[mm]	1	1	1.238	1.238
$h_k^{(C)}$	[mm]	0.1	0.1	0.1	0.1
$L_k^{(stub)}$	[mm]	3	3	3	3
$L_k^{(cav)}$	[mm]	3		3	
$s_{11}^{(I)}$	[dB]	-25.4		-32.7	
$s_{11}^{(C)}$	[dB]	-29.6		-33.7	
XPR	[dB]	-30.1		-37.8	
XPT	[dB]	-28.4		-35.8	
$\Delta\Phi$	[deg]	4.33		1.86	
$\epsilon_{\Delta\Phi}$	[%]	4.8		2	

Table 2.6. Geometry and electrical performances comparison between the DFS constrained and unconstrained polarizers with two stubs.

	Unit	3-stub const. pol.			3-stub unconst. pol.		
D	[mm]	2.62			2.49		
$w_k^{(I)}$	[mm]	1	1	1	1.126	1.032	1.126
$h_k^{(I)}$	[mm]	0.624	0.614	0.624	0.585	0.742	0.585
$w_k^{(C)}$	[mm]	1.238	1.425	1.238	1.741	1.216	1.741
$h_k^{(C)}$	[mm]	0.1	0.122	0.1	0.1	0.131	0.1
$L_k^{(stub)}$	[mm]	3	3	3	2.895	2.948	2.895
$_k^{(cav)}$	[mm]	3	3		3.236	3.236	
$s_{11}^{(I)}$	[dB]	-36.5			-33.8		
$s_{11}^{(C)}$	[dB]	-30.8			-34.7		
XPR	[dB]	-36.6			-37.2		
XPT	[dB]	-35.4			-36.7		
$\Delta\Phi$	[deg]	1.94			1.67		
$\epsilon\_\Delta\Phi$	[%]	2.1			1.8		

Table 2.7. Geometry and electrical performances comparison between the DFS constrained and unconstrained polarizers with three stubs.

2.3.2 Blending Effect and Final Polarizer Geometry

The realization of the DFS polarizer exploiting platelet technology and wire spark erosion technique requires to take into account the actual manufacturing of the device that includes the blending of the stubs terminations (see Fig. 2.26). The main blending effect is the reduction of the effective heights of both inductive and capacitive arms and, as a consequence, it deteriorates the performance of the polarizer. In particular we have observed that the XPT and $\epsilon_{\Delta\Phi}$ are particularly sensitive to the arms heights reduction. However, the nominal performance of the polarizer can be fully recovered by varying the heights of both arms in order to

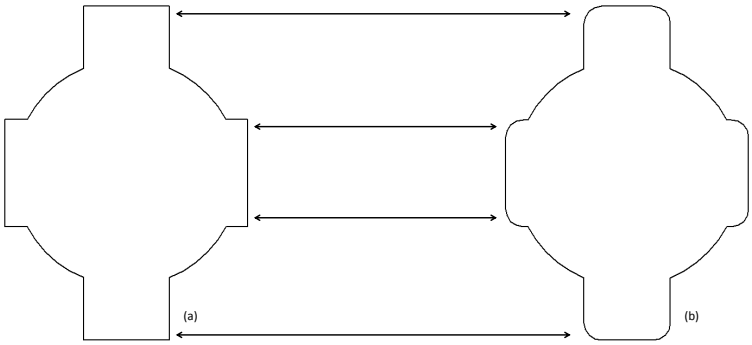

Figure 2.26. DFS cross-section geometry before (a) and post (b) blending the stub terminations.

compensate for the blending effect. Fig. 2.27–2.31 show the reflection coefficients, XPT, XPR and the relative differential phase error($\epsilon_{\Delta\Phi}$) as a function of the heights increments $\Delta h^{(I)} = h^{(I)}_{new} - h^{(I)}_{old}$ and $\Delta h^{(C)} = h^{(C)}_{new} - h^{(C)}_{old}$ of the inductive and capacitive arms, respectively. The variables $h^{(I)}_{old}$ and $h^{(C)}_{old}$ denote the values of the optimized structure before edge blending.. The curves refer to a blend with curvature radius equal to $0.2\,\mathrm{mm}$. In the plots, a common minimum indicated by a red circle can be observed for $\Delta h^{(I)} = 17\,\mu\mathrm{m}$ and $\Delta h^{(C)} = 12\,\mu\mathrm{m}$, corresponding to XPT$\leq -35\,\mathrm{dB}$ and $\epsilon_{\Delta\Phi} \leq 2\,\%$. Note that without this compensation XPT and $\epsilon_{\Delta\Phi}$ increase to $-29\,\mathrm{dB}$ and $4\,\%$, respectively.

Table 2.8 reports the final polarizer configuration geometry and the relevant performances. Fig. 2.32–2.37 show a comparison between the original version of the polarizer (where the blending on the stubs terminations is not applied) and the final polarizer configuration.

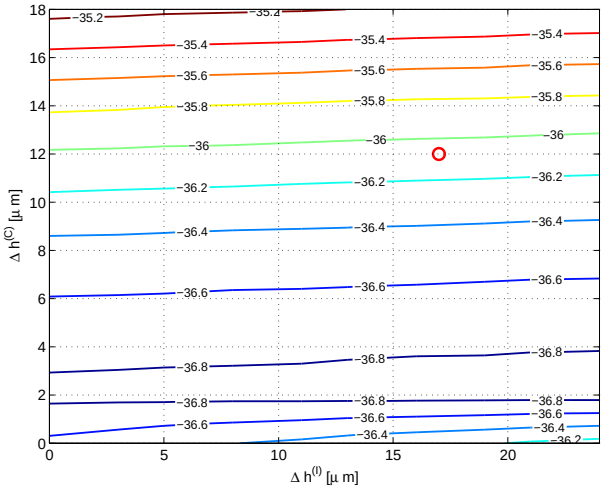

Figure 2.27. Maximum reflection coefficient of inductive polarization($s_{11}^{(I)}$) in the operative band [85,104] GHz for the DFS polarizer having blended edges as a function of heights increments $\Delta h^{(I)}$ and $\Delta h^{(C)}$ for the inductive and capacitive arms. The polarizer geometry is reported in Table 2.7.

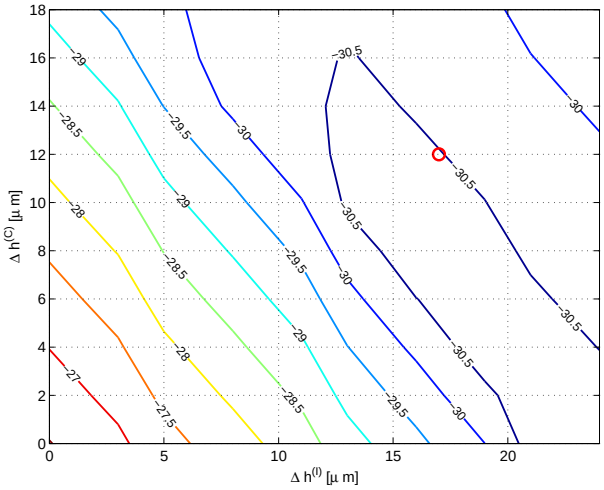

Figure 2.28. Maximum reflection coefficient of capacitive polarization ($s_{11}^{(C)}$) in the operative band [85,104] GHz for the DFS polarizer having blended edges as a function of heights increments $\Delta h^{(I)}$ and $\Delta h^{(C)}$ for the inductive and capacitive arms. The polarizer geometry is reported in Table 2.7.

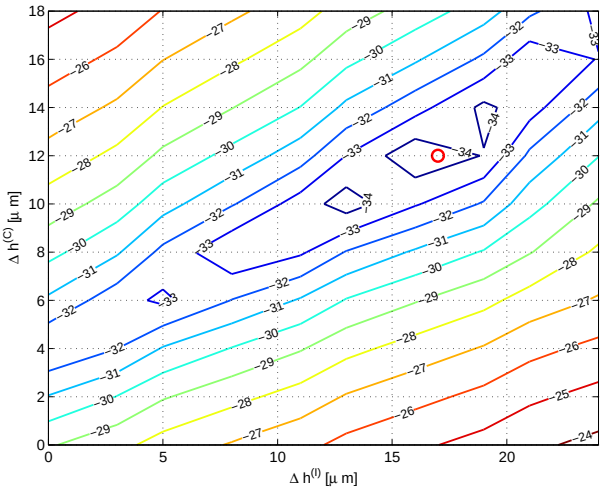

Figure 2.29. Maximum Cross Polarization in Transmission (XPT) in the operative band [85,104] GHz for the DFS polarizer having blended edges as a function of heights increments $\Delta h^{(I)}$ and $\Delta h^{(C)}$ for the inductive and capacitive arms. The polarizer geometry is reported in Table 2.7.

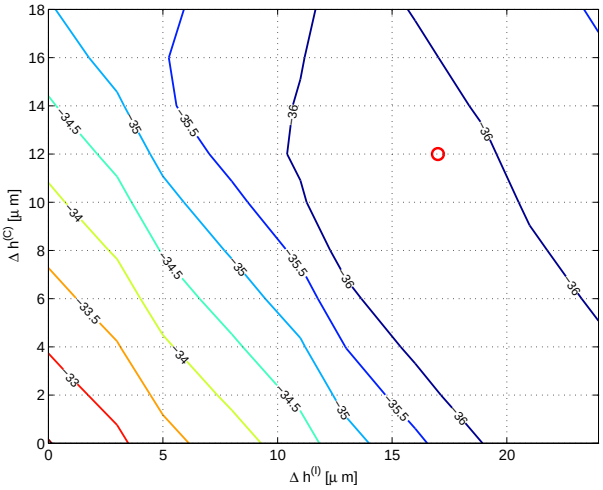

Figure 2.30. Maximum Cross Polarization in Reflection (XPR) in the operative band [85,104] GHz for the DFS polarizer having blended edges as a function of heights increments $\Delta h^{(I)}$ and $\Delta h^{(C)}$ for the inductive and capacitive arms. The polarizer geometry is reported in Table 2.7.

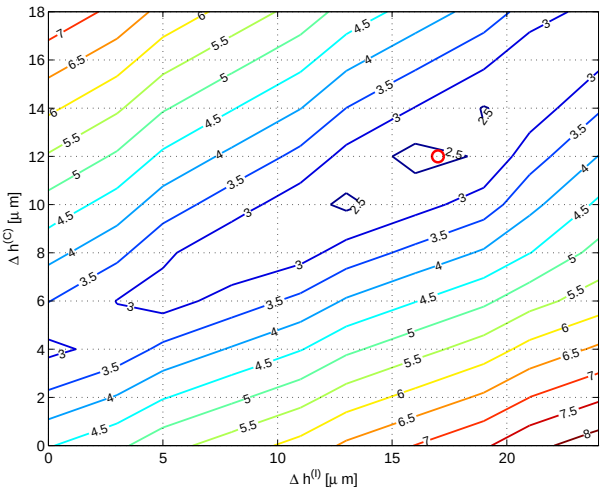

Figure 2.31. Relative differential phase error($\epsilon_{\Delta\Phi}$) in the operative band [85,104] GHz for the DFS polarizer having blended edges as a function of heights increments $\Delta h^{(I)}$ and $\Delta h^{(C)}$ for the inductive and capacitive arms. The polarizer geometry is reported in Table 2.7.

	Unit	DFS pol. geometry		
D	[mm]	2.62		
$w_k^{(I)}$	[mm]	1	1	1
$h_k^{(I)}$	[mm]	0.642	0.632	0.642
$w_k^{(C)}$	[mm]	0.113	0.135	0.113
$h_k^{(C)}$	[mm]	0.1	0.122	0.1
$L_k^{(stub)}$	[mm]	3	3	3
$L_k^{(cav)}$	[mm]	3	3	
$s_{11}^{(I)}$	[dB]	-35.963		
$s_{11}^{(C)}$	[dB]	-30.39		
XPR	[dB]	-36.056		
XPT	[dB]	-34.922		
$\Delta\Phi$	[deg]	2.056		
$\epsilon_{\Delta\Phi}$	[%]	2.284		

Table 2.8. Final three DFS polarizer geometry with blending and relevant performances.

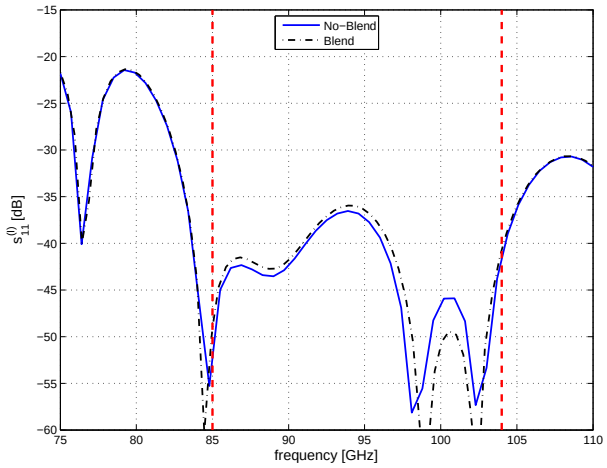

Figure 2.32. Reflection coefficient of the inductive polarization ($s_{11}^{(I)}$) for the pre-blending and post-blending three-DFSs polarizers. The vertical dashed-lines indicate the operative frequency band.

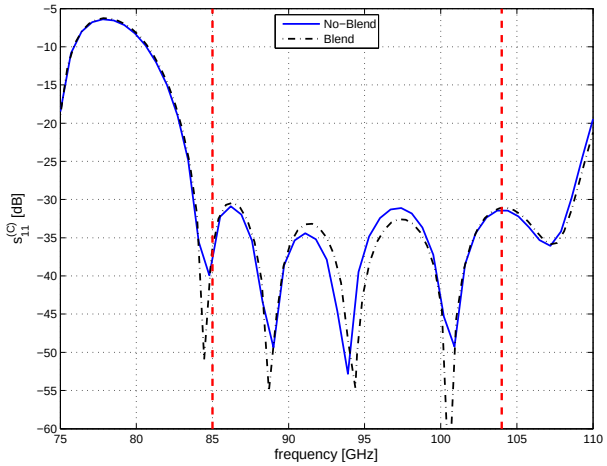

Figure 2.33. Reflection coefficient of the capacitive polarization ($s_{11}^{(C)}$) for the pre-blending and post-blending three-DFSs polarizers. The vertical dashed-lines indicate the operative frequency band.

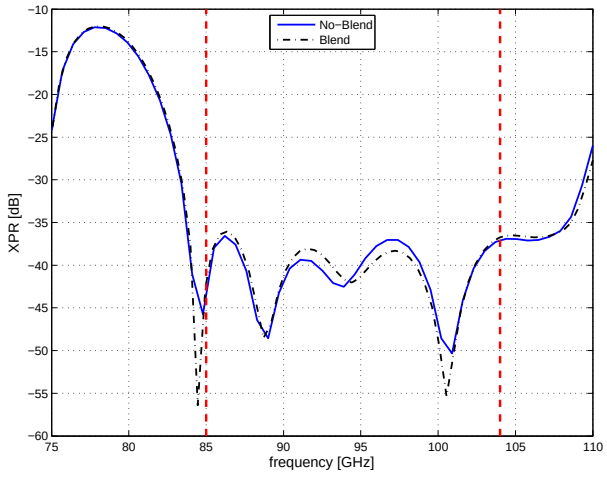

Figure 2.34. Cross Polarization in Reflection (XPR) for the pre-blending and post-blending three-DFSs polarizers. The vertical dashed-lines indicate the operative frequency band.

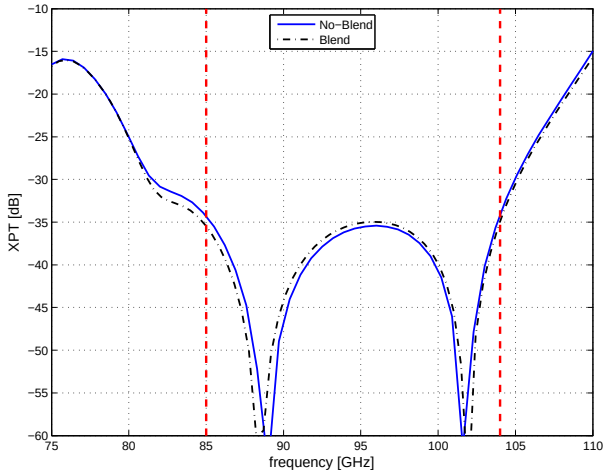

Figure 2.35. Cross Polarization in Transmission (XPT) for the pre-blending and post-blending three-DFSs polarizers. The vertical dashed-lines indicate the operative frequency band.

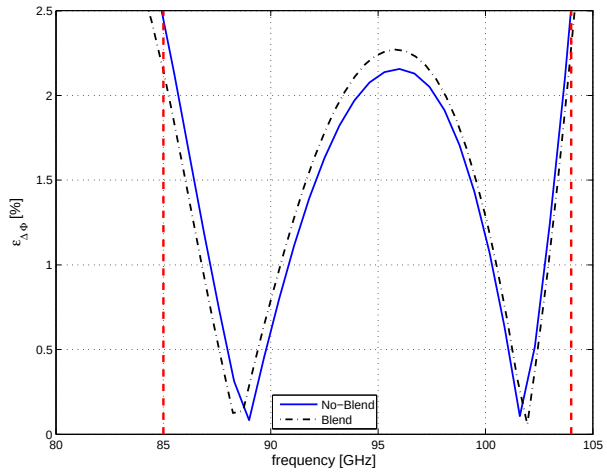

Figure 2.36. Relative differential phase error($\epsilon_{\Delta\Phi}$) for the pre-blending and post-blending three-DFSs polarizers. The vertical dashed-lines indicate the operative frequency band.

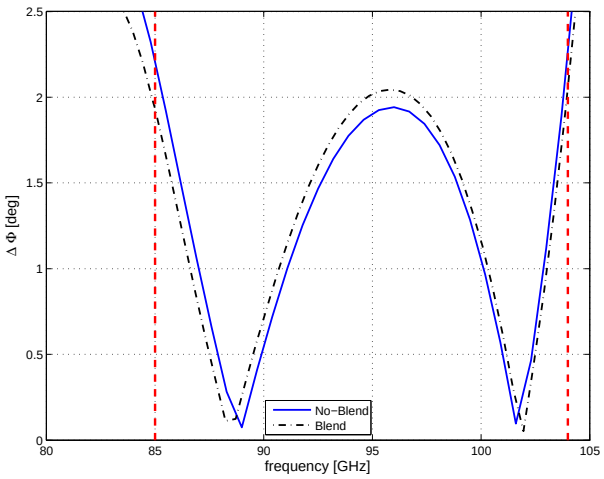

Figure 2.37. Absolute differential phase error($\mathbf{\Delta\Phi}$) for the pre-blending and post-blending three-DFSs polarizers. The vertical dashed-lines indicate the operative frequency band.

The polarizer structure have been analyzed considering different values of surface equivalent resistivity(ρ) in order to determine the effect of metallic losses on the insertion losses. Fig. 2.38–2.39 show the transmission coefficients for the inductive($s_{21}^{(I)}$) and capacitive($s_{21}^{(C)}$) polarizations as a function of frequency for different values of ρ.

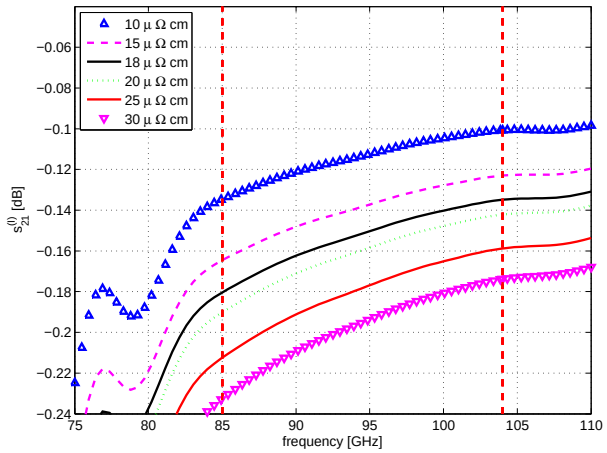

Figure 2.38. Transmission coefficient of the inductive polarization $s_{21}^{(I)}$ in the 20% bandwidth centered at 94.5 GHz for different resistivity values. The vertical dash--lines denote the operative band.

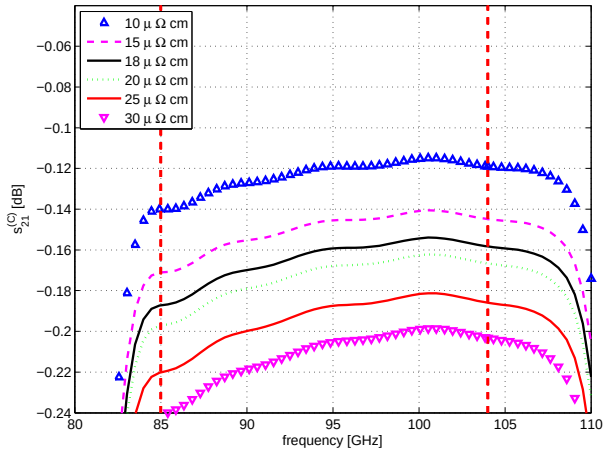

Figure 2.39. Transmission coefficient of the capacitive polarization $s_{21}^{(C)}$ in the 20% bandwidth centered at 94.5 GHz for different resistivity values. The vertical dash-lines denote the operative band.

2.3.3 Tolerance Analysis

The sensitivity analysis of the complete structure has been carried out before manufacturing the component. To this end, a set of 1000 polarizer's geometries (obtained by inserting random perturbations in the range of $\pm 5\,\mu m$) have been analyzed. The envelope and the nominal curves of the reflection coefficients ($s_{11}^{(I)}$ and $s_{11}^{(C)}$), the cross polarization terms (XPT and XPR) and the differential phase shift are reported on the left side in Fig. 2.40–2.44. The same data has been presented using histogram bars on the right side in Fig. 2.40–2.44.

The same procedure has been repeated by considering random perturbations in the ranges $[3,40]\,\mu m$ in order to understand the dependency of the device performances with the manufacturing tolerance. The results of this extensive analysis is summarized in the Fig. 2.45–2.50, where the means value and the standard deviation are reported for different tolerances. In these plots, the perturbation range is $tol \in \pm\{3,5,10,20,30,40\}\,\mu m$. The figures put in evidence, how some parameters (e.g. $s_{11}^{(I)}$) are less sensitive with respect to the others (e.g. $s_{11}^{(C)}$, XPT, XPR and Φ). The deterioration in the polarizer's performance is considerably high when larger values of tolerances are considered. It is important to point out that this tolerance analysis has been driven by considering the variation of transversal, longitudinal and all the geometrical parameters of the polarizer. Since the device has to be realized in platelet technology, it is interesting to understand whether the performance degradation is mainly related to the longitudinal parameters variations (i.e. the stubs and cavities lengths) or to the transversal parameters variations (i.e. the heights and widths of the stubs and the diameters). For a large-scale production of this device, it is preferable to choose commercially available metal layers of standard thickness. Since the cross section of each stubs is realized by wire spark erosion technique, its manufacturing accuracy and precision can be set to the best achievable level. But higher precision requirement will increase the manufacturing time and cost.

In Table 2.9 the mean value and the standard deviation of the DFS polarizer performance parameters are reported for 3, 5, 10, 20, 30 and $40\,\mu m$ perturbation in all dimensions. Fig. 2.45–2.50 show the mean value and standard deviation of the polarizer performance as a function of the tolerance for the transversal and longitudinal dimension, respectively. The plots put in evidence that the degradation in performances are mainly related to the variation of the cross-section. For instance, the absolute differential phase error ($\Delta\Phi$) increases from 2° to 5° when tolerances in the order of $\pm 20\,\mu m$ on the cross-section parameters are considered, while it remains almost unvaried when the same variation is considered to the longitudinal parameters. This fact confirms that platelet technology is applicable to the manufacturing of the polarizer, since commercially available metal plates with standard accuracy in the oder of $\pm 20 \div 30\,\mu m$ can be employed. Finally, for the design under consideration, it is reasonable to consider acceptable manufacturing tolerance in the range of $\pm 10\,\mu m$, that can be guaranteed by precise wire EDM.

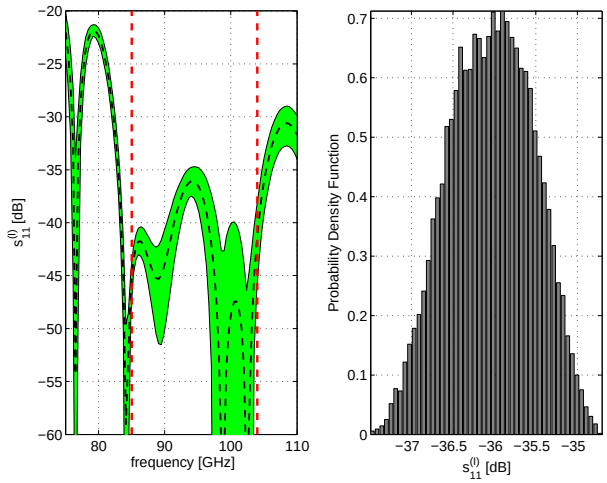

Figure 2.40. Reflection coefficient of the inductive polarization ($s_{11}^{(I)}$) of the DFS polarizer. (On the left) The green envelop refers to the frequency responses obtained by introducing $\pm 5\,\mu m$ perturbation in all dimensions. The vertical dashed lines denote the 20% band centered at $94.5\,GHz$. (On the right) Probability density function of $s_{11}^{(I)}$ obtained by the $\pm 5\,\mu m$ perturbation analysis.

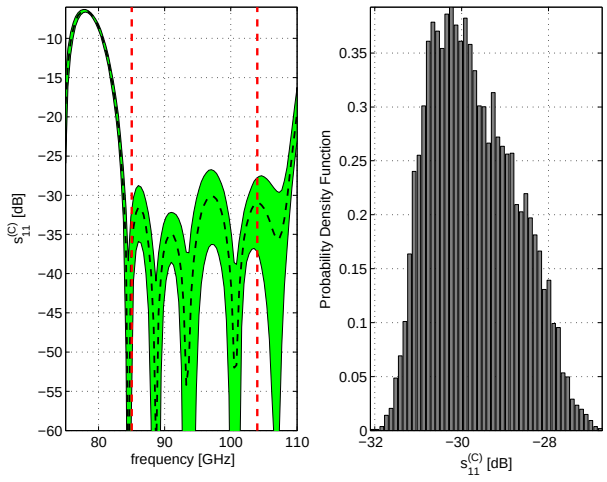

Figure 2.41. Reflection coefficient of the capacitive polarization($s_{11}^{(C)}$) of the DFS polarizer. (On the left) The green envelop refers to the frequency responses obtained by introducing $\pm 5\,\mu m$ perturbation in all dimensions. The vertical dashed lines denote the 20% band centered at $94.5\,GHz$. (On the right) Probability density function of $s_{11}^{(C)}$ obtained by the $\pm 5\,\mu m$ perturbation analysis.

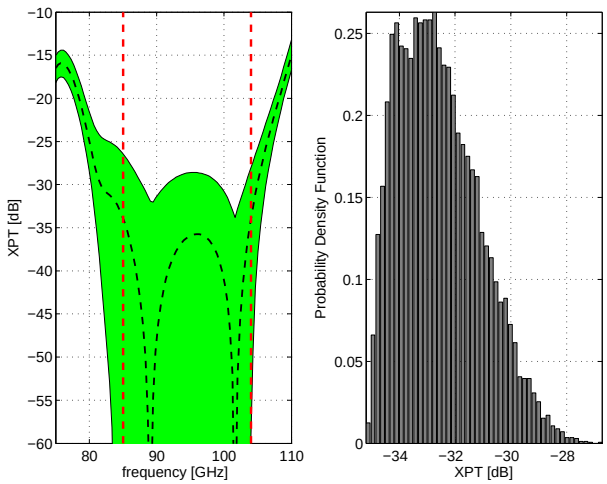

Figure 2.42. Cross Polarization in Transmission (XPT) of the DFS polarizer. (On the left) The green envelop refers to the frequency responses obtained by introducing ±5 µm perturbation in all dimensions. The vertical dashed lines denote the 20% band centered at 94.5 GHz. (On the right) Probability density function of XPT obtained by the ±5 µm perturbation analysis.

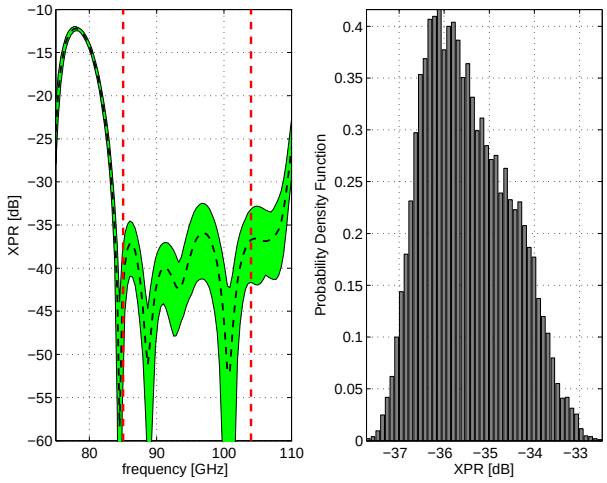

Figure 2.43. Cross Polarization in Reflection (XPR) of the DFS polarizer. (On the left) The green envelop refers to the frequency responses obtained by introducing ±5 µm perturbation in all dimensions. The vertical dashed lines denote the 20% band centered at 94.5 GHz. (On the right) Probability density function of XPR obtained by the ±5 µm perturbation analysis.

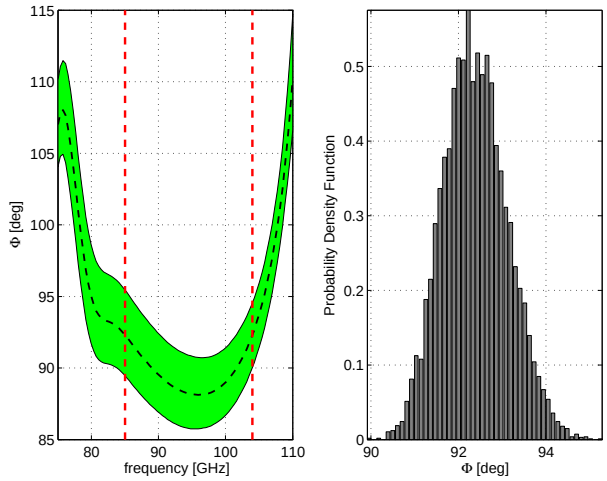

Figure 2.44. Differential phase shift (Φ) of the DFS polarizer. (On the left) The green envelop refers to the frequency responses obtained by introducing $\pm 5\,\mu m$ perturbation in all dimensions. The vertical dashed lines denote the 20% band centered at 94.5 GHz. (On the right) Probability density function of Φ obtained by the $\pm 5\,\mu m$ perturbation analysis.

Parameter	Tolerance[µm]	Mean value	Standard deviation
$s_{11}^{(I)}$ [dB]	3	-36.0614	0.3057
	5	-36.0402	0.5084
	10	-35.9678	0.9977
	20	-35.4221	1.7593
	30	-34.2849	2.357
	40	-33.0056	2.787
$s_{11}^{(C)}$ [dB]	3	-30.0144	0.7267
	5	-29.7159	0.9788
	10	-28.9036	1.4891
	20	-27.357	2.1711
	30	-25.9551	2.5836
	40	-24.677	2.8815
XPT [dB]	3	-33.3988	1.0284
	5	-32.5633	1.4617
	10	-30.7821	2.3013
	20	-28.1029	3.3052
	30	-26.1099	3.8864
	40	-24.4193	4.3897
XPR [dB]	3	-35.7984	0.6947
	5	-35.4784	0.9461
	10	-34.6534	1.4593
	20	-33.0434	2.1088
	30	-31.5847	2.494
	40	-30.2062	2.7858
Φ [deg]	3	92.2924	0.4433
	5	92.3847	0.7353
	10	92.6313	1.4899
	20	93.1576	3.0013
	30	93.6784	4.4772
	40	94.3827	6.0823

Table 2.9. Mean value and standard deviation of the DFS polarizer's performance parameters for 3, 5, 10, 20, 30 and 40 µm perturbation in all dimensions.

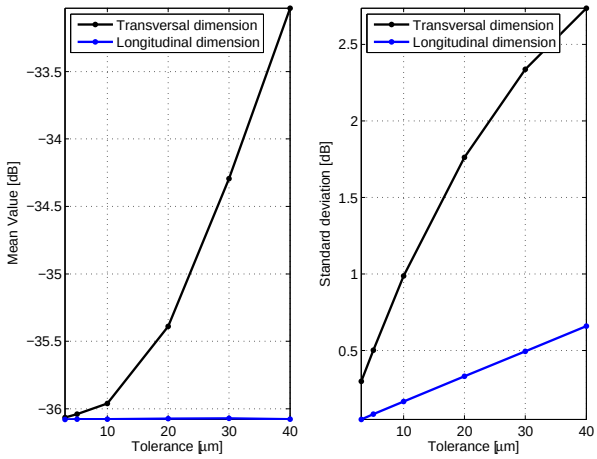

Figure 2.45. Reflection coefficient distribution of the DFS polarizer for the inductive polarization ($s_{11}^{(I)}$) obtained by performing the tolerance analysis along the longitudinal and transversal dimensions in the 20% bandwidth centered at 94.5 GHz. (On the left) Mean value. (On the right) Standard deviation.

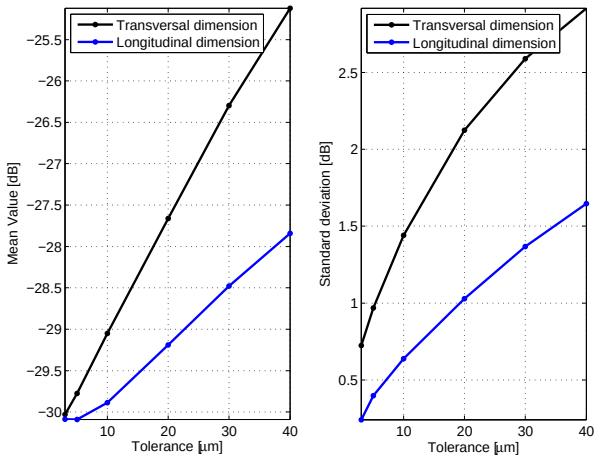

Figure 2.46. Reflection coefficient distribution of the DFS polarizer for the capacitive polarization ($s_{11}^{(C)}$) obtained by performing the tolerance analysis along the longitudinal and transversal dimensions in the 20% bandwidth centered at 94.5 GHz. (On the left) Mean value. (On the right) Standard deviation.

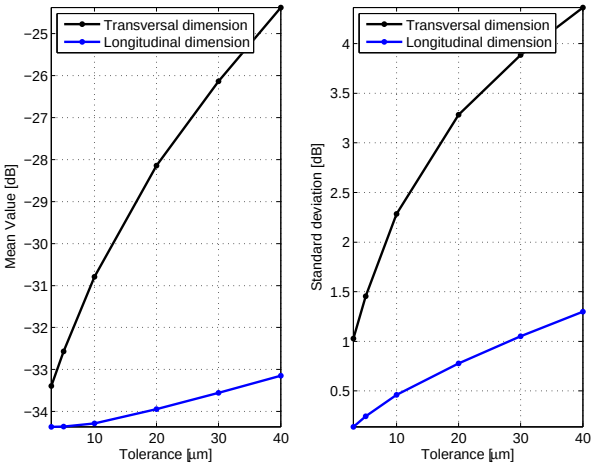

Figure 2.47. Cross Polarization in Transmission (XPT) distribution of the DFS polarizer obtained by performing the tolerance analysis along the longitudinal and transversal dimensions in the 20% bandwidth centered at 94.5 GHz. (On the left) Mean value. (On the right) Standard deviation.

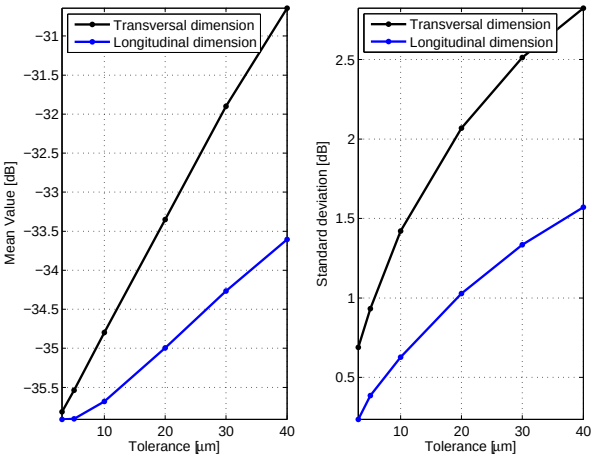

Figure 2.48. Cross Polarization in Reflection (XPR) distribution of the DFS polarizer obtained by performing the tolerance analysis along the longitudinal and transversal dimensions in the 20% bandwidth centered at 94.5 GHz. (On the left) Mean value. (On the right) Standard deviation.

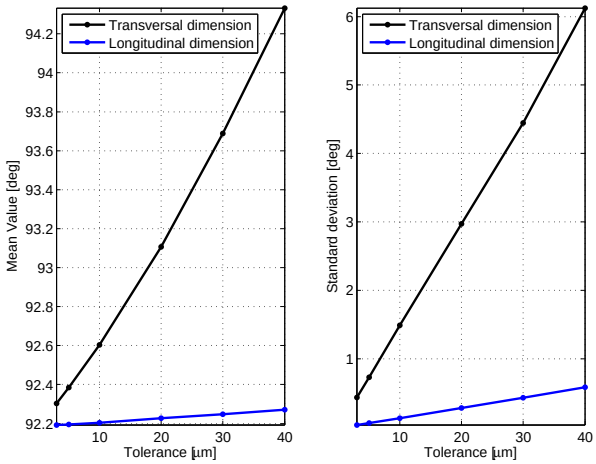

Figure 2.49. Differential phase shift(Φ) distribution of the DFS polarizer obtained by performing the tolerance analysis along the longitudinal and transversal dimensions in the 20% bandwidth centered at 94.5 GHz. (On the left) Mean value. (On the right) Standard deviation.

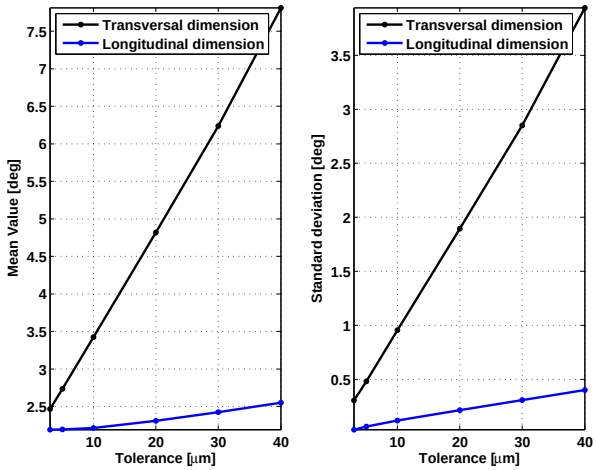

Figure 2.50. Absolute differential phase error($\Delta\Phi$) distribution of the DFS polarizer obtained by performing the tolerance analysis along the longitudinal and transversal dimensions in the 20% bandwidth centered at 94.5 GHz. (On the left) Mean value. (On the right) Standard deviation.

2.3.4 Mechanical Analysis of the Prototypes

Two DFS polarizers prototypes have been manufactured using 7 plates. With reference to Fig. 2.52 showing an exploded view of the component, the first and last plates contain the input and output circular waveguides, the plates 2, 4 and 6 contain the stubs, whereas the cavities are manufactured in plates 3 and 5. Apart from the first and last plates (the interface ones) whose thickness is equal to 5 mm, the thickness of the other plates are equal to 3 mm as already discussed. With reference to Fig. 2.51, two alignment pins (whose diameter is 2 mm) are placed along the capacitive arm centered at 15 mm diameter circle. Four M3 Hex standard screws are used in order to pack the 7 plates together. These screws are placed opposite to each other and are centered at 8.2 mm diameter circle. A cutout can be seen on plate 1, 2, 4, 6, 7 in Fig. 2.52. The aim of the cutout is to reduce the surface contact among the plates in order to increase the strain around the center regions of the plate and, as a consequence, to minimize the insertion loss for spurious leakage. The corners of the plates 2 to 6 have been cut in order to make some space for the alignment pins placed on plate 1 and plate 7 that are used to align the polarizer with the horn and the OMT. These 8 alignment pins are equidistantly placed around a 22 mm diameter circle and allow the component to be mounted in several positions. In this way, it is possible to measure the polarizer both in a stand-alone configuration along its principal directions and in the operative condition. In the latter condition the polarizer is mounted inside the feed-horn assembly with its principal axes rotated by 45 degrees with respect to the OMT axes.

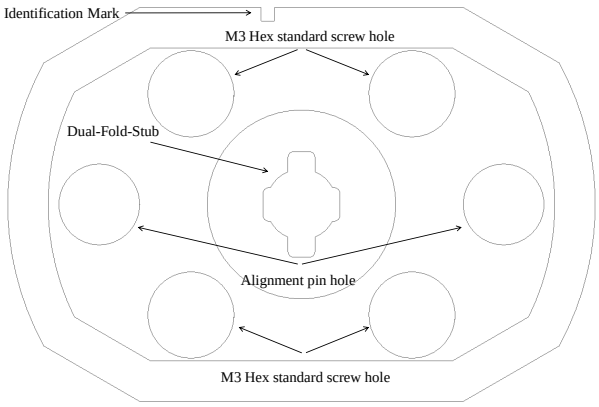

Figure 2.51. Mechanical design of plate 2 of the DFS polarizer. Identification mark, holes for M3 hex screw, alignment pins and the Dual-Fold-Stub (DFS) are marked by arrows.

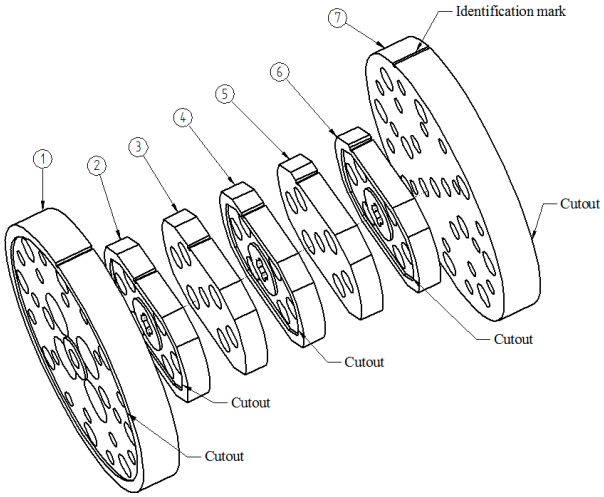

Figure 2.52. Exploded view of the DFS polarizer. Plate numbers along with their identification marks and the cutouts are depicted here.

A plate identification mark having dimension $0.5\,\text{mm} \times 0.5\,\text{mm}$ is excavated on the side of each plate in order to put the plate on its right position and order. This identification mark can be seen from Fig. 2.51–2.52.

Using a 2-axis non-contact measuring microscope[6] each layer has been mechanically measured. In particular, the circle diameters, the height and the width of each stub has been evaluated. The accuracy in the mechanical measurements through the microscope has been estimated, by using some reference samples, to be within $\pm 10\,\mu\text{m}$. The two prototypes of the DFS polarizer have been named A and B. The nominal and the measured values for plates 2, 4 and 6 for prototype A and B are reported in table 2.10 and 2.12, respectively. The nominal and the measured values of for plates 1, 3, 5 and 7 for the two prototypes are reported in table 2.11 and 2.13. These values have been determined by a suitable procedure described in the following.

A set of points along the cross section of the plate is collected for each layer (see Fig. 2.53). It is then exploited to recreate the manufactured cross section in order to compare it with the nominal dimension. For each data set, this comparison requires the evaluation of the translation and the rotation of the acquired points in order to minimize the unwanted systematic errors in the acquisition. These geometrical operations have been done by first considering the points that belong to the pins and determining the best fitting circles $\mathscr{C}_1$ and $\mathscr{C}_2$. The origin $\boldsymbol{O}$ of the coordinate system is, then, determined as the middle point between the centers $\boldsymbol{O}_1$ and $\boldsymbol{O}_2$ of the circles $\mathscr{C}_1$ and $\mathscr{C}_2$, respectively (see Figure 2.54). The rotation angle θ is then determined

[6]Hawk Optical Measurement Microscope With qc - 200 Microprocessor.

from the slope of the line which connects the centers O_1 and O_2 (see Figure 2.54) and according to this θ, the classical rotational transformation is applied in order to rotate the measured set of points. An example of measured set of points before and after the rotation is reported in Fig. 2.55. Finally, the comparison between the rotated data set with the nominal cross-section is performed, as depicted in Fig. 2.56. This procedure has revealed a good agreement between the nominal and measured cross sections for all the plates and confirms a manufacturing accuracy of the wire EDM within the measurement accuracy of the microscope, i.e. $\pm 10\,\mu m$, thus confirming that the platelet design of the DFS polarizer with the required electrical performances is feasible.

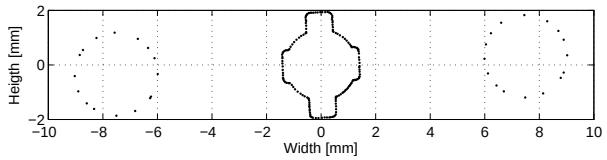

Figure 2.53. Acquired set of points using microscope over the cross section of prototype A, plate 2.

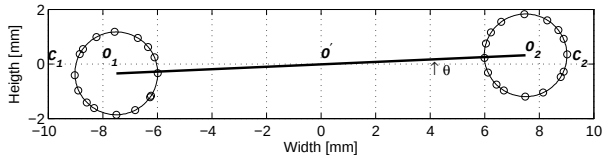

Figure 2.54. Acquired set of points using microscope over the alignment pin cross section of prototype A, plate 2. Two fitted circle $\mathscr{C}_1$, $\mathscr{C}_2$ on the acquired data set having center at $\mathscr{O}_1$ and $\mathscr{O}_2$ are reported. The balck solid line joining the center of both circles having an inclination θ from the horizontal axis

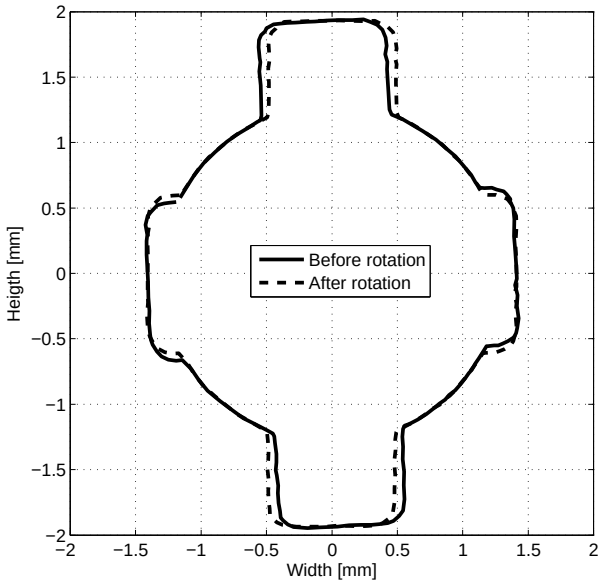

Figure 2.55. Example of mechanical measurement using microscope. The solid line denotes the acquired set of points over the DFS cross section, whereas the dash line refers to the same data set after the rotation through an angle θ as depicted in Fig. 2.54.

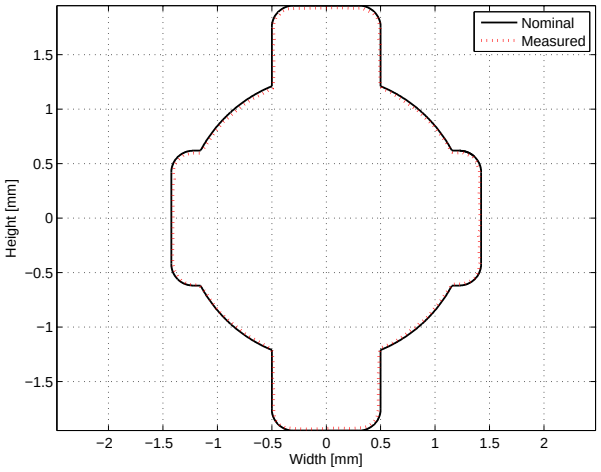

Figure 2.56. Acquired set of points using microscope over the DFS cross section for prototype A, plate 2 compared with the nominal geometry of the plate.

2.3.5 Electrical Measurements

The two prototypes A and B of the DFS polarizer have been measured in the W band using a circular waveguide setup connected to a Hewlett Packard (HP)-8510C 2-port VNA with millimeter-wave extension to operate in the $75 - 110\,\mathrm{GHz}$

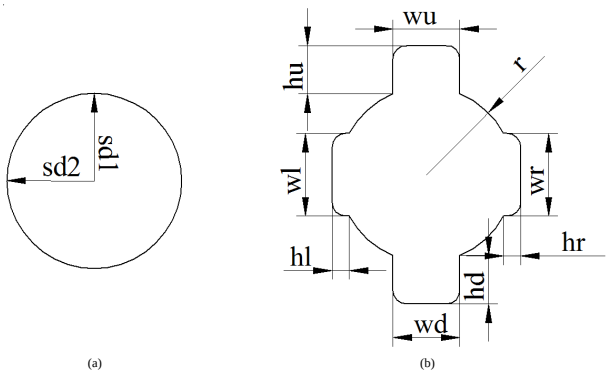

Figure 2.57. Labeling of the geometrical parameters that have been measured through the microscope. Figure (a) refers to plates 1, 3, 5 and 7 (circular waveguide sections), whereas Fig. (b) refers to plates 2, 4 and 6 (Dual-Fold-Stub (DFS)).

	Plate No. 2			Plate No. 4			Plate No. 6		
	Model	Meas	Δ	Model	Meas	Δ	Model	Meas	Δ
wu	1	0.982	-0.018	1	0.997	-0.003	1	0.995	-0.005
wd	1	0.989	-0.011	1	1	0	1	0.996	-0.004
wr	1.238	1.231	-0.007	1.425	1.424	-0.001	1.238	1.238	0
wl	1.238	1.235	-0.003	1.425	1.422	-0.003	1.238	1.228	-0.01
hu	0.741	0.74	-0.001	0.731	0.725	-0.006	0.741	0.74	-0.001
hd	0.741	0.729	-0.012	0.731	0.734	0.003	0.741	0.74	-0.001
hr	0.268	0.259	-0.009	0.346	0.347	0.001	0.268	0.258	-0.01
hl	0.268	0.266	-0.002	0.346	0.344	-0.002	0.268	0.269	0.001
r	1.31	1.303	-0.007	1.31	1.313	0.003	1.31	1.306	-0.004

Table 2.10. Mechanical measurement of the DFS polarizer prototype A: plates number 2, 4 and 6. The deviation Δ is the difference between measured and nominal values. All dimensions are in millimeter.

band. As shown in Fig. 2.58, the setup consists of WR10 rectangular waveguides, a pair of Flann transitions[31] from WR10 to circular waveguide and two custom flanges. The setup has been calibrated by performing a Through-Reflection-Line (TRL) calibration procedure at the circular waveguide ports.

The measurements have been performed in two steps by mounting the polarizer along both the principal directions. In this way, the scattering parameters have been determined for both the inductive and capacitive polarizations. The measurement results for the principal polarizations of both prototypes are reported in Fig. 2.59–2.64. The comparison with the simulation is also reported in these figures. It can be noticed that the measurements results are in good agreement with the predicted results concerning both the curve levels and location of the zeros. In particular, for both prototypes the reflection coefficients for the inductive and capacitive polarizations are better than $-35\,\mathrm{dB}$ and $-28\,\mathrm{dB}$ in the operative band, respectively. The

	Plate No. 1			Plate No. 3			Plate No. 5			Plate No. 7		
	Model	Meas	Δ	Model	Meas	Δ	Model	Meas	Δ	Model	Meas	Δ
sd1	1.31	1.303	-0.007	1.31	1.309	-0.001	1.31	1.312	0.002	1.31	1.302	-0.008
sd2	1.31	1.302	-0.008	1.31	1.308	-0.002	1.31	1.311	0.001	1.31	1.309	-0.001

Table 2.11. Mechanical measurement of the DFS polarizer prototype A: plates number 1, 3, 5 and 7. The deviation Δ is the difference between measured and nominal values. All dimensions are in millimeter.

	Plate No. 2			Plate No. 4			Plate No. 6		
	Model	Meas	Δ	Model	Meas	Δ	Model	Meas	Δ
wu	1	0.989	-0.011	1	0.995	-0.005	1	0.983	-0.018
wd	1	0.995	-0.005	1	0.996	-0.004	1	0.989	-0.011
wr	1.238	1.234	-0.004	1.425	1.424	-0.001	1.238	1.231	-0.007
wl	1.238	1.236	-0.002	1.425	1.421	-0.004	1.238	1.226	-0.012
hu	0.741	0.738	-0.003	0.731	0.738	0.007	0.741	0.738	-0.003
hd	0.741	0.734	-0.007	0.731	0.733	0.002	0.741	0.736	-0.005
hr	0.268	0.265	-0.003	0.346	0.332	-0.014	0.268	0.254	-0.014
hl	0.268	0.265	-0.003	0.346	0.342	-0.004	0.268	0.258	-0.01
r	1.31	1.309	-0.001	1.31	1.3	-0.01	1.31	1.304	-0.006

Table 2.12. Mechanical measurement of the DFS polarizer prototype B: plates number 2, 4 and 6. The deviation Δ is the difference between measured and nominal values. All dimensions are in millimeter.

insertion losses for both prototypes and both polarizations are better than approximately $-0.2\,\mathrm{dB}$ with an equalization between the two channels within $0.02\,\mathrm{dB}$. By comparing Fig. 2.38–2.39 with the relevant measured curves in Fig. 2.61–2.62, we can infer that the actual value of resistivity in the frequency band under consideration is about $18\,\mu\Omega\mathrm{cm}$ for both prototypes. The measured values of the main figure-of-merit of the polarizer, i.e. the differential phase shift(Φ) between the two principal polarizations, are very close to the predicted one with a relative differential phase error($\epsilon_{\Delta\Phi}$) within $2.5\,\%$. The aforementioned measured results for the principal directions translate in quite interesting results when the polarizer is analyzed according to its working basis, i.e. circular and tilted polarizations. Indeed, the measured values of XPT and XPR shown in Fig. 2.65 and 2.66 are in very good agreement with the predicted curves. Since both polarizer prototypes exhibit a XPT better than $-34\,\mathrm{dB}$, the validity of the design solution exploiting platelet technology has been successfully validated.

Fig. 2.67–2.69 show the measured and computed relevant terms of the matrices **H** and **K** that describe the polarizer behavior in terms of Stokes parameters when the polarizer is to be used in the dual-circular polarization radiometer as shown in Fig. 1.1 on page 5. The coefficients $\boldsymbol{H}_{QQ}$ and $\boldsymbol{H}_{UU}$ are the direct terms and, hence, have to be maximized. Conversely, the coefficient $\boldsymbol{K}_{QI}$ refers to the contamination in the $\boldsymbol{Q}$ channel due to the total intensity $\boldsymbol{I}$. This quantity has to be minimized because the

	Plate No. 1			Plate No. 3			Plate No. 5			Plate No. 7		
	Model	Meas	Δ	Model	Meas	Δ	Model	Meas	Δ	Model	Meas	Δ
sd1	1.31	1.302	-0.008	1.31	1.306	-0.004	1.31	1.31	0	1.31	1.289	-0.021
sd2	1.31	1.308	-0.002	1.31	1.305	-0.005	1.31	1.304	-0.006	1.31	1.301	-0.009

Table 2.13. Mechanical measurement of the DFS polarizer prototype B: plates number 1, 3,5 and 7. The deviation Δ is the difference between measured and nominal values. All dimensions are in millimeter.

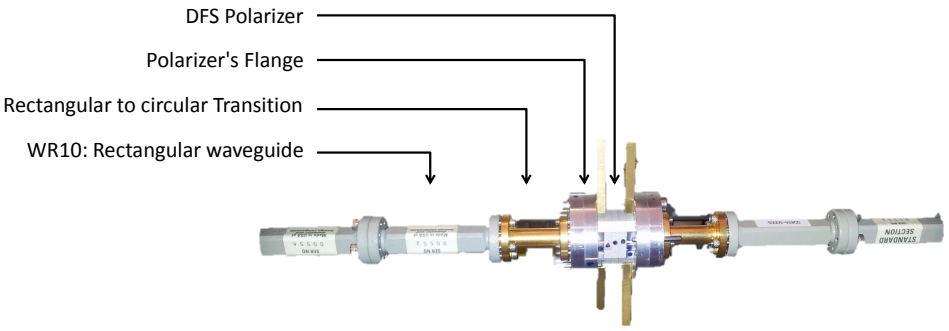

Figure 2.58. Waveguide setup that is connected to the VNA in order to experimentally characterize the DFS polarizer prototypes.

signal of interest, i.e. the linearly polarized signal, is very faint as compared to the total intensity. It can be also seen from its mathematical expression (see Eq. 1.26) that this quantity is zero when $|s_{21}^{(I)}| = |s_{21}^{(C)}|$ or, in other words, when a good amplitude equalization between the two channel is achieved. Since a channel equalization within $0.02\,\mathrm{dB}$ has been achieved for both prototypes, the measuerd value of $\boldsymbol{K}_{QI}$ is better than $-23\,\mathrm{dB}$ in the operative band, that is a promising result for W-band polarimeter arrays. Finally, the coefficient $\boldsymbol{K}_{UV}$ refers to the contamination in the $\boldsymbol{U}$ channel due to circularly polarized signals. As discussed in Sec. 1.6, this parameter is related to the differential phase shift(Φ). Indeed, the frequency behavior of the electrical parameters $\boldsymbol{K}_{UV}$ and XPT are the same apart for a scale factor due to the fact that $\boldsymbol{K}_{UV}$ deals with quadratic quantities.

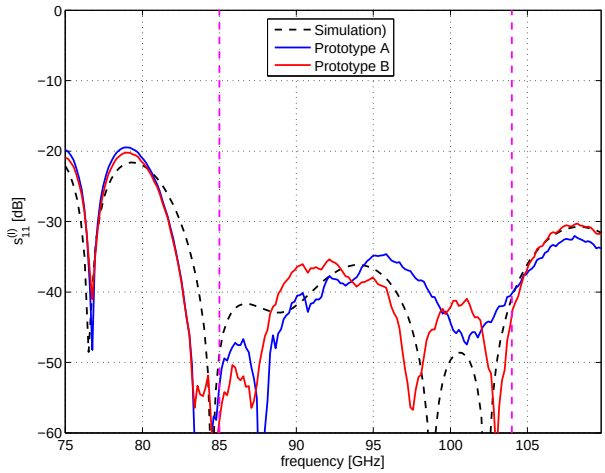

Figure 2.59. Computed and measured reflection coefficients for the inductive polarization ($s_{11}^{(I)}$) of the W-band DFS polarizer prototypes A and B. The vertical dash lines denotes the operative band $[85,\ 104]$ GHz.

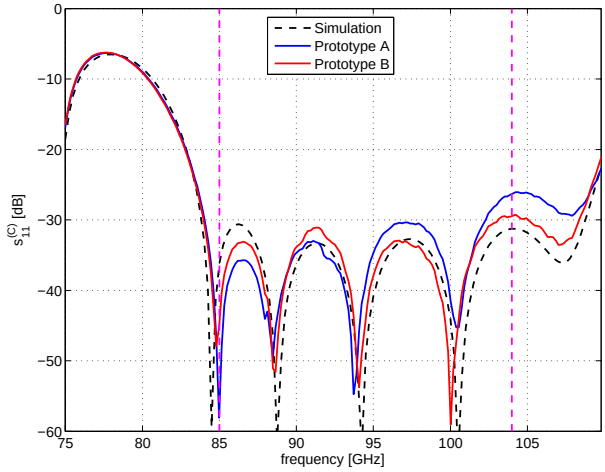

Figure 2.60. Computed and measured reflection coefficients for the capacitive polarization ($s_{11}^{(C)}$) of the W-band DFS polarizer prototypes A and B. The vertical dash lines denotes the operative band $[85,\ 104]$ GHz.

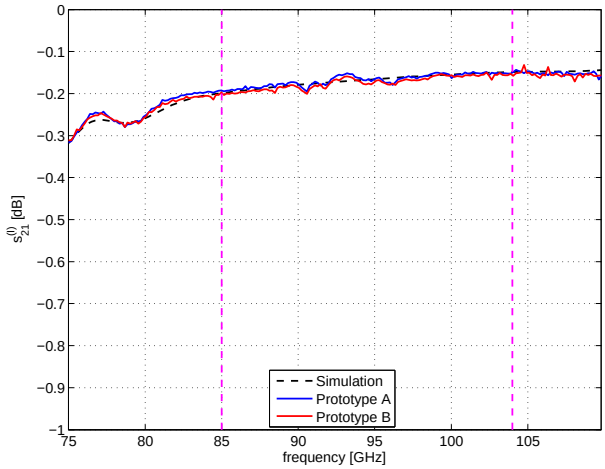

Figure 2.61. Computed and measured transmission coefficients for the inductive polarization ($s_{21}^{(I)}$) of the W-band DFS polarizer prototypes A and B. The vertical dash lines denotes the operative band [85, 104] GHz.

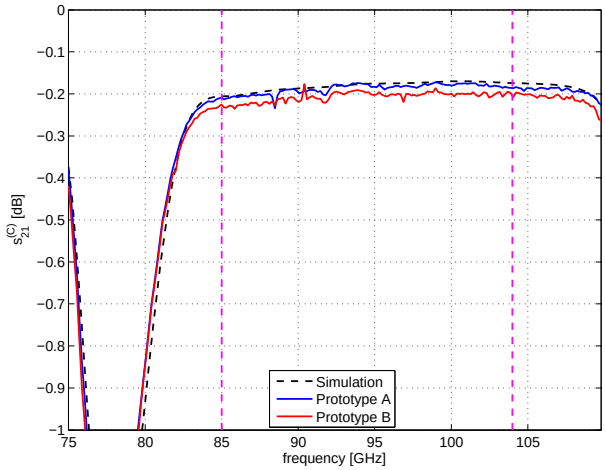

Figure 2.62. Computed and measured transmission coefficients for the capacitive polarization ($s_{21}^{(C)}$) of the W-band DFS polarizer prototypes A and B. The vertical dash lines denotes the operative band [85, 104] GHz.

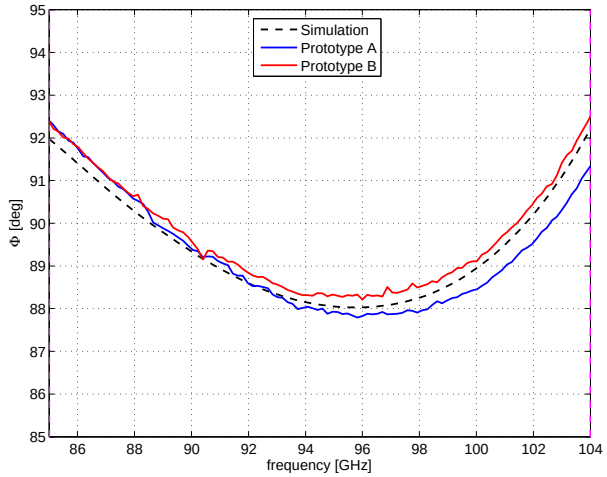

Figure 2.63. Computed and measured levels of differential phase shift (Φ) (in operative band) between the transmission coefficients of the two principal polarizations for the W-band DFS polarizer prototypes A and B.

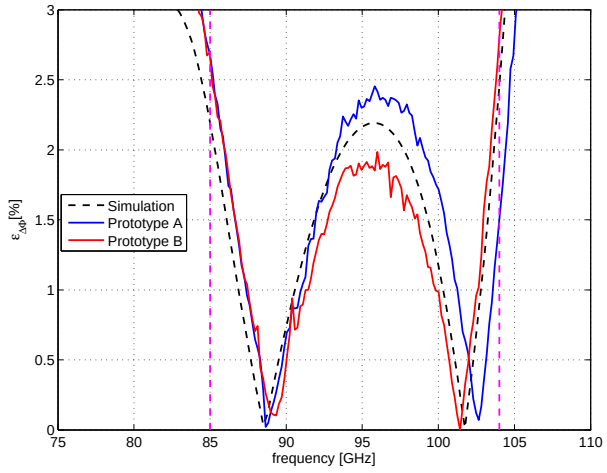

Figure 2.64. Computed and measured levels of relative differential phase error ($\epsilon_{\Delta\Phi}$) for the W-band DFS polarizer prototypes A and B. The vertical dash lines denote the operative band $[85,\ 104]$ GHz

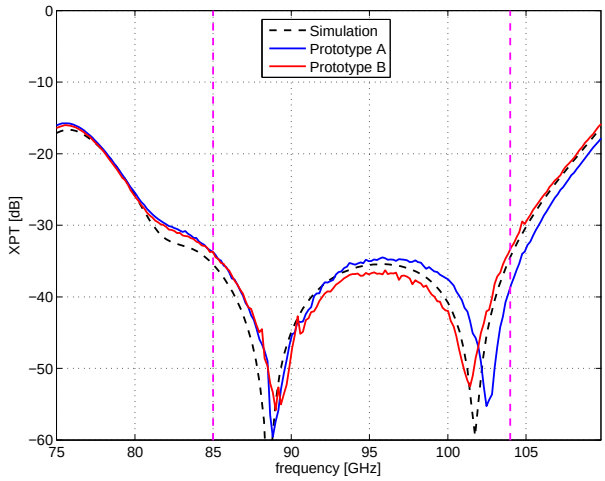

Figure 2.65. Computed and measured levels of Cross Polarization in Transmission (XPT) for the W-band DFS polarizer prototypes A and B. The vertical dash lines denote the operative band [85, 104] GHz.

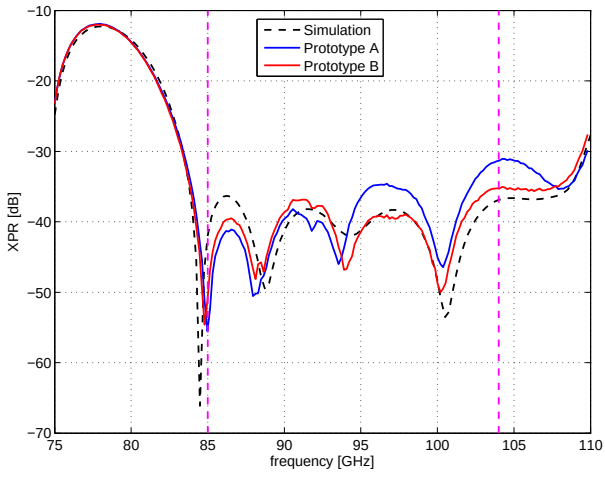

Figure 2.66. Computed and measured levels of Cross Polarization in Reflection (XPR) for the W-band DFS polarizer prototypes A and B. The vertical dash lines denote the operative band [85, 104] GHz.

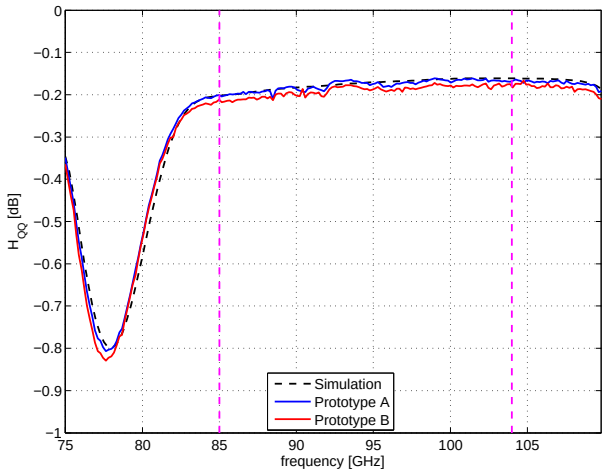

Figure 2.67. Computed and measured coefficients $\boldsymbol{H}_{QQ}$ for the W-band DFS polarizer prototypes A and B. The vertical dash lines denote the operative band [85, 104] GHz.

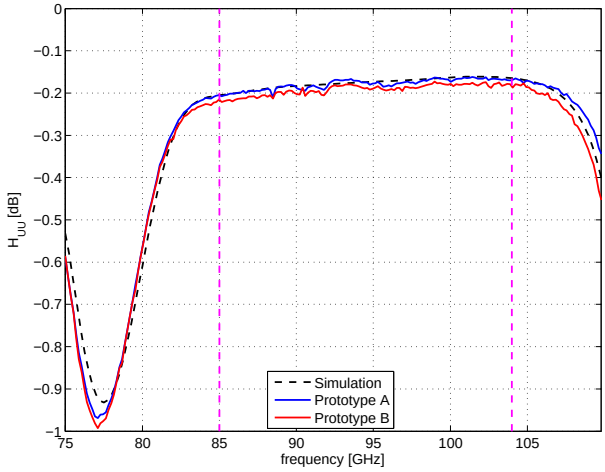

Figure 2.68. Computed and measured coefficients of $\boldsymbol{H}_{UU}$ for the W-band DFS polarizer prototypes A and B. The vertical dash lines denote the operative band [85,104] GHz.

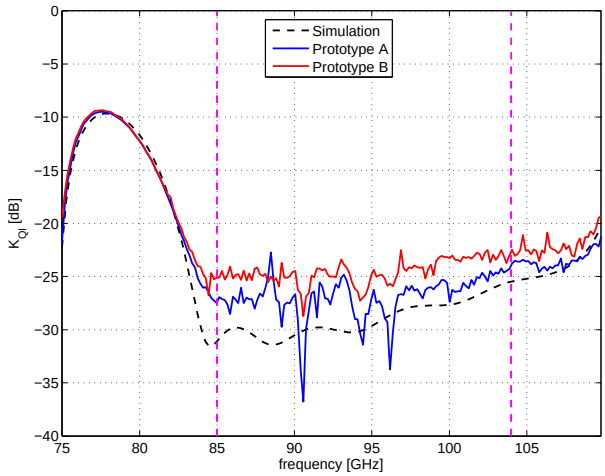

Figure 2.69. Computed and measured effects on the Q channel due to total intensity ($\boldsymbol{K}_{QI}$) for the W-band DFS polarizer prototypes A and B. The vertical dash lines denote the operative band [85, 104] GHz

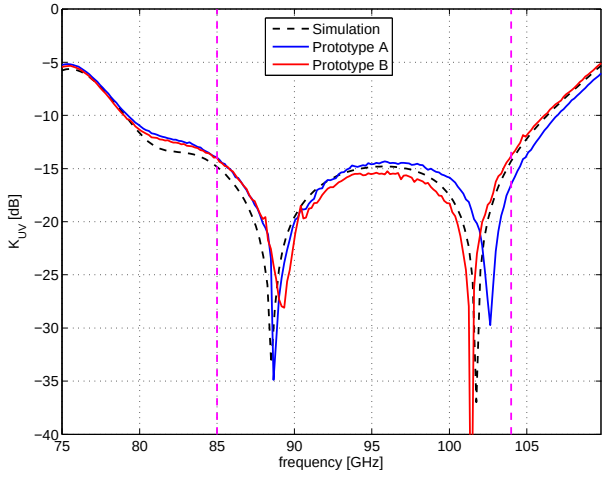

Figure 2.70. Computed and measured effects on the U channel due to circularly polarized signals ($\boldsymbol{K}_{UV}$) for the W-band DFS polarizer prototypes A and B. The vertical dash lines denote the operative band [85, 104] GHz.

2.4 Conclusions

In this chapter two polarizer configurations (i.e. SFS and DFS) have been considered for a W-band high performance polarizer with 20 % bandwidth centered at 94.5 GHz. It has been shown that the DFS solution is particularly suitable for wide band performances and mass production manufacturing, exploiting platelet technology and wire spark erosion technique. Two prototypes have been manufactured and mechanically/electrically measured. The remarkable agreement between simulated and measured results confirms the applicability of the configuration conceived during this doctoral program to the realization of polarimeter arrays.

Chapter 3

OMT

3.1 Introduction

Ortho-mode transducer (OMTs) are exploited in dual-polarization waveguide feed-systems to combine or separate orthogonal polarizations. The OMT is a waveguide component usually placed just after the polarizer in the feed assembly chain, as depicted in Fig. 1.1 on page number 5[1]. An OMT has three physical waveguide ports: the so called common port and two coupled ports, as shown in Fig. 3.1. The common port has two-fold-symmetrical cross section, for instance a square or a circular waveguide. Since the structure has two-fold-symmetry, it allows the propagation of two degenerated modes. The two coupled ports are usually mono-modal rectangular waveguide ports.

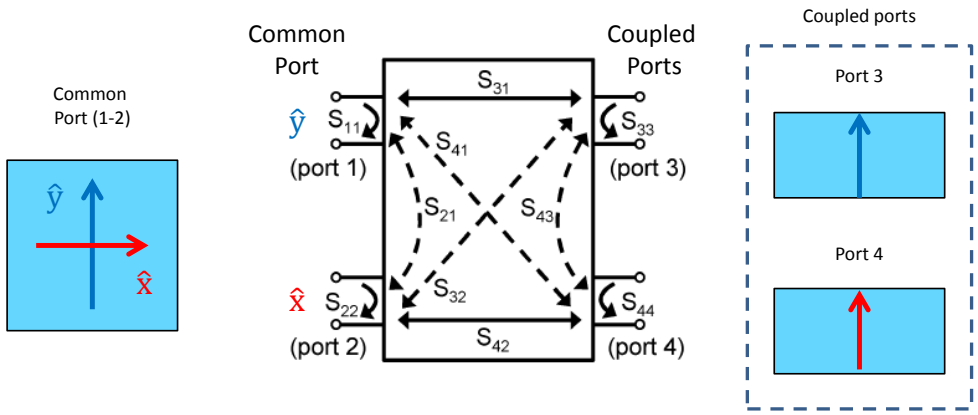

Figure 3.1. Three waveguide ports of the OMT and the four-port scattering matrix equivalent circuit

[1]If the system works in linear polarization, then OMT is placed just after the horn/antenna.

A waveguide OMT is designed in such a way that the incident polarizations along $\hat{\mathbf{x}}$ and $\hat{\mathbf{y}}$ direction (hereinafter referred as orthogonal polarizations) at the common ports are routed separately to the two single-mode ports. In Fig. 3.1, Ports 3 and 4 are the ports coupled to the two orthogonal polarizations at the common port. Therefore, from an electrical point of view, four electrical ports are required in order to describe an OMT, as shown in Fig. 3.1. In ideal conditions, the magnitude of the direct transmission scattering parameters s_{31} and s_{42} should be ideally equal to one. On the other hand, the magnitude of the cross-coupling terms s_{41}, s_{32} and the isolation terms s_{21}, s_{43} should be zero.

3.2 OMT Performance Evaluation Parameters

In the feed assembly chain, the mechanical and electrical characteristics of the OMT play a significant role. From the mechanical point of view, it should have compact size and low weight because these two parameters are directly related to the size and weight of the entire feed assembly. The orientations and the dimensions of the ports are also an important design parameter. Transitions and bends can be avoided if the proper orientation and the standard dimension ports are considered. From the electrical perspective, the isolation between the orthogonal polarizations should be high and this requirement can be achieved by considering a symmetrical structure. Since the return loss should be high, some matching elements are introduced as discussed in the subsequent section. The insertion loss should be very low and this requirement can be attained by using some material with low surface equivalent resistive (e.g. Aluminum) and a sufficient number of packing screws in order to avoid any wave leakage. Group delay equalization between the orthogonal polarizations is also required in some specific applications e.g. correlation polarimeters.

3.3 OMT in Literature

Several OMT designs are reported in the literature for narrow and wide band applications. The selection of a particular configuration mainly depends on the application. As it has been already mentioned, the performance of the OMT affect the overall feed assembly, hence considerable attention is required in order to choose a proper configuration.

In the subsequent sections, asymmetrical, symmetrical and two fold symmetrical designs are discussed along their pros and cons. Then, some matching elements are reported in order to improve the return loss and, finally, a broadband turnstile junction design strategy and the simulation results are discussed in detail.

Examples of asymmetrical and symmetrical designs having a common square waveguide port are reported in section 3.3.1 and 3.3.2. The same configurations can

be used in conjunction with a common circular waveguide port. The polarizations along the $\hat{\mathbf{x}}$ and $\hat{\mathbf{y}}$ directions correspond to the TE_{10} and TE_{01} modes, respectively, as shown in Fig. 3.2 and Fig. 3.3.

3.3.1 Side-Coupling OMT

The simplest OMT configuration is a T-Junction or side-coupling OMT, as reported in[32][33] and shown in Fig. 3.2. The incident TE_{10} fundamental mode at common port having the polarization along $\hat{\mathbf{y}}$ direction propagates in the common waveguide and couples to the fundamental mode TE_{10} of the rectangular waveguide port 3. The TE_{10} mode in the common waveguide does not couple to the fundamental mode TE_{10} of the rectangular waveguide port 4. This is related to the symmetry of the structure i.e. the orthogonality of their field distributions does not allow any mutual coupling. On the other-hand, the incident TE_{01} mode at common port hav-

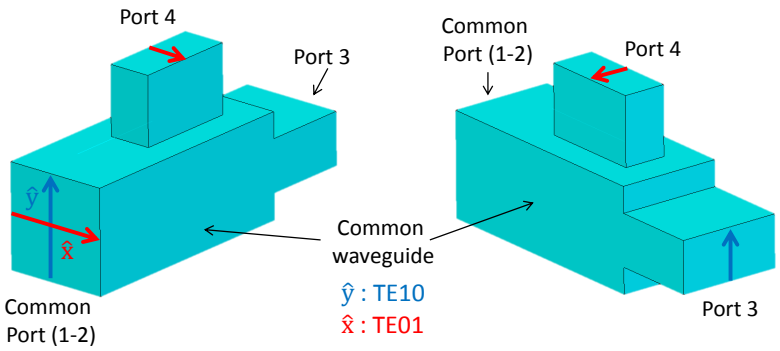

Figure 3.2. Standard T-junction OMT.

ing the polarization along $\hat{\mathbf{x}}$ direction couples to the side arm's fundamental mode TE_{10} of the rectangular waveguide port 4 and this polarization is under cut-off at port 3. Hence, port 3 and 4 are also isolated if only the fundamental mode is under consideration. The coupling arm can be changed according to the requirements of the feed system, i.e. an E-plane coupling arm can be designed instead of the H-plane coupling arm shown in Fig. 3.2. Although side-coupling OMTs are quite simple and compact, they only work in narrow frequency bands. Their operative bandwidth can be increased by introducing some matching element like septa, irises and steps. In this way, the operative bandwidth can be enlarged up to 20 % or dual-band components can be designed. In any case, because of the one-fold symmetrical structure, the bandwidth is limited due to the cutoff frequency of the higher-order modes TE_{11} and TM_{11}.

3.3.2 Boifot OMT

The *Boifot* junction based OMT is exploited to enlarge the operative band[34][35]. A symmetric E-plane coupling is used for the polarization along the $\hat{\mathbf{x}}$ direction, as shown in Fig. 3.3. This kind of coupling provides two fold symmetry[2] that avoids the excitation of the $\boldsymbol{TE}_{11}$ and $\boldsymbol{TM}_{11}$ higher-order modes in the common port. Therefore, in this configuration the bandwidth can be enlarged up to the $\boldsymbol{TE}_{20}$ cutoff frequency. On the other hand, the two symmetric side arms need to be recombined, by exploiting the straight and bent rectangular waveguide sections in order to obtain a single signal at port 4. Therefore this structure is more complex with respect to the side-coupling OMT.

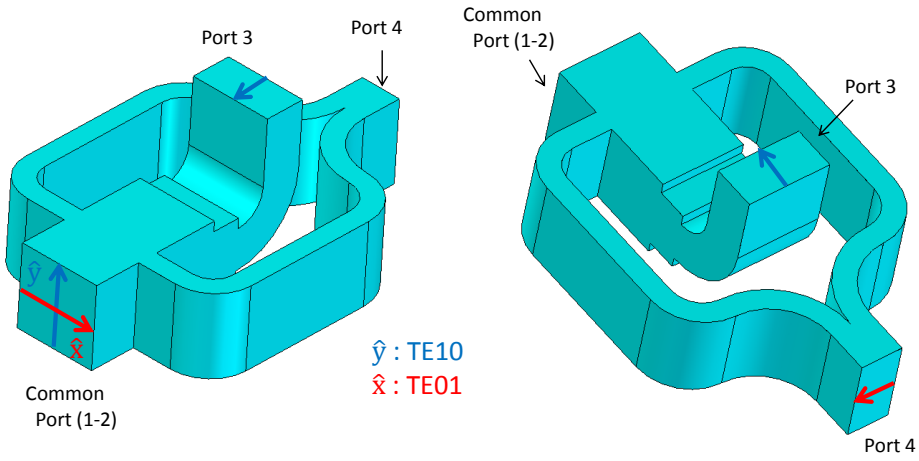

Figure 3.3. Structure of the Boifot OMT.

It should be noticed that any differential error in the length of the two waveguides of the combining network due to the machining inaccuracy could destroy the symmetry of the structure and, consequently, a performance degradation would be observed. Additionally, the insertion loss and group delay are intrinsically quite different for both polarizations.

3.3.3 Turnstile Based OMT

In this OMT configuration, a turnstile junction is used to separate the two orthogonal polarized signals into two separate waveguides. It has a common square/-circular waveguide port and four rectangular waveguide ports as reported in Fig. 3.4. The physical ports are, then, five whereas six electrical ports are necessary if only

[2]For the polarization along $\hat{\mathbf{x}}$ direction

the fundamental mode is considered. The turnstile junction exploits a symmetric E-plane coupling for both polarizations. For a perfectly symmetric structure, the incoming $\hat{\mathbf{x}}$−polarized signal couples to the fundamental $\boldsymbol{TE}_{10}$ mode at port 1 and port 2 as reported with dotted line in Fig. 3.4. The same polarization excites the $\boldsymbol{TE}_{01}$ mode at ports 3 and 4 but this mode is under cut-off in the operative frequency range of the structure. Hence, the power is equally split between port 1 and port 2, but the signals at port 1 and at port 2 are in counter-phase. Similarly, the incoming $\hat{\mathbf{y}}$-polarized signal couples to the fundamental $\boldsymbol{TE}_{10}$ mode at the ports 3 and 4 (see Fig. 3.4). In particular, half signal flows to port 3 and the other half si routed to port 4, but the two coupled signals are in counter-phase. Since the turnstile junction has two-fold symmetry, it inherently has a very good isolation level. The $\boldsymbol{TE}_{11}$ mode does not excite the $\boldsymbol{TM}_{01}$ and $\boldsymbol{TE}_{21}$ modes in the common waveguide. Therefore, the upper limit of the frequency band is related to the cutoff frequency of the $\boldsymbol{TM}_{11}$ mode at the common port and the cutoff frequency of the $\boldsymbol{TE}_{01}$ mode at the coupled ports. As a drawback, two different waveguide structures (not shown in Fig. 3.4) are required to combine the opposite ports. Also in this case, possible asymmetries of the combiners owing to the manufacturing uncertainties should be managed to avoid isolation problems. This OMT type can operate in a large frequency band (more than 30 %) with good power handling properties. However, the presence of two combiners make this configuration less compact and with higher losses with respect to the previous solutions.

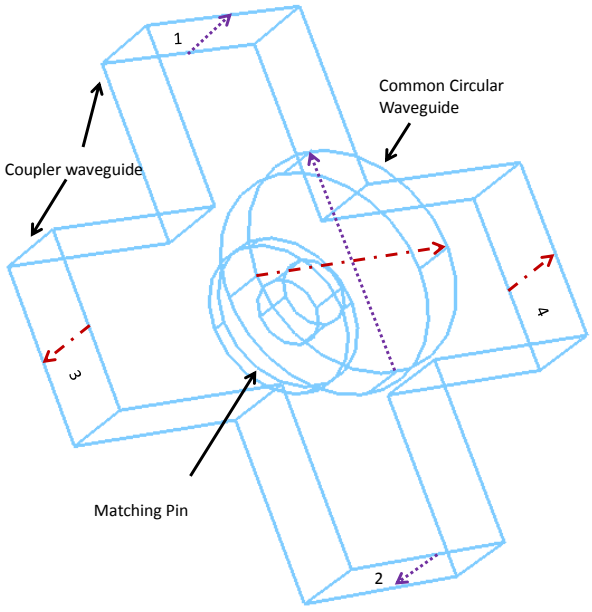

Figure 3.4. Turnstile junction having two pin as a matching element.

Matching Element

Usually a proper protrusion with either pyramidal, cylindrical or parallelepiped shapes can be introduced in the back of the junction in order to improve the matching. The turnstile junction exhibits the same insertion loss and group delay for both polarizations since the latter undergo a symmetric coupling at the same section of the common port. Various shape and combination of shapes of matching elements are reported in literature e.g.

- Cylindrical pin(Ref. [11])
- Two cylindrical pins(Ref. [36])
- Five cylindrical pins(Ref. [37])
- Pyramidal pin(Ref. [38][39])
- Square prism pin(Ref. [40][41])
- Two square prism pin.

3.3.4 Broad Band Turnstile Junction

As an example, the design of a broad band turnstile junction with a 40 % bandwidth centered at 40 GHz (Q-Band) with reflection level lower than −35 dB is described in this section. This component has been obtained by exploiting the COM-EM-AT described in Chapter 4. In the subsequent paragraph the design strategy is discussed and finally the frequency response of the turnstile junction designed is reported.

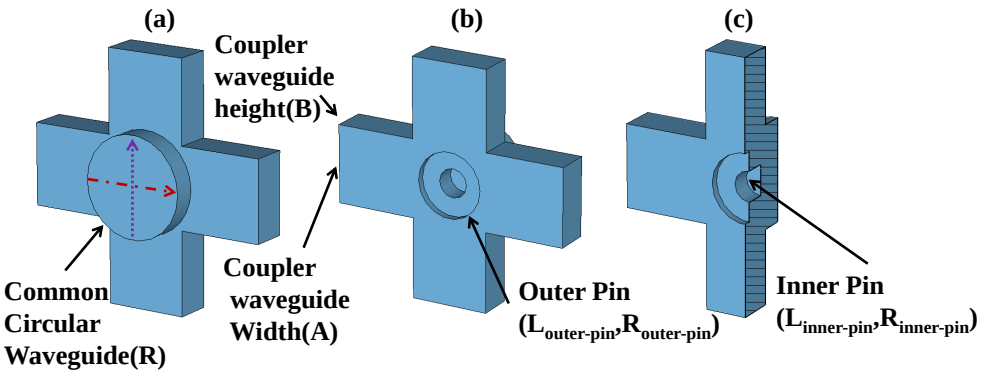

Figure 3.5. Structure of the turnstile junction. (a) Front view. (b) Back view. (c) Back view with cutting plane.

Design Approach Two cylindrical pins are used as a matching element. These are placed at the bottom of the common circular waveguide, as reported in Fig. 3.5. The two pins add four design parameter i.e. length and radius of each pin. The radius of both pins have a design constrain. If the radius of the lower pin is smaller than the upper one then there is a probability to break down this matching structure. Therefore, in order to avoid this situation, the radius of the lower cylindrical pin should always be greater than the upper pin. Henceforth, the lower and upper pins are named as outer and inner, respectively. Since the structure would be manufactured as a stack of metal plates(multi-layer design), the height $\boldsymbol{B}$ of the rectangular waveguide is fixed by the thickness of the metal plate[3]. Hence, there are six design parameters i.e.

$\boldsymbol{R}$: Common circular waveguide radius

$\boldsymbol{A}$: Broader side of the couplar waveguide

$\boldsymbol{R}_{outer-pin}$: Radius of the outer pin

$\boldsymbol{L}_{outer-pin}$: Length of the outer pin

$\boldsymbol{R}_{inner-pin}$: Radius of the inner pin

$\boldsymbol{L}_{inner-pin}$: Length of the inner pin

Instead of performing a six dimensional grid analysis this problem can be split in two groups. A parent grid is created using $\boldsymbol{R}$ and $\boldsymbol{A}$ with a step of $0.1\,\text{mm}$. The range for $\boldsymbol{R}$ and $\boldsymbol{A}$ are defined as:

- $\boldsymbol{R}$: $3.3\,\text{mm} \rightarrow 3.5\,\text{mm}$
- $\boldsymbol{A}$: $5.1\,\text{mm} \rightarrow 5.7\,\text{mm}$

Hence, the parent grid has 3×7 points as reported in Fig. 3.6. For each point of the parent grid a sub-grid related to the dimensions of the matching pins($\boldsymbol{R}_{outer-pin}$, $\boldsymbol{L}_{outer-pin}$, $\boldsymbol{R}_{inner-pin}$ and $\boldsymbol{L}_{inner-pin}$) is defined. The range for $\boldsymbol{R}_{outer-pin}$ and $\boldsymbol{R}_{inner-pin}$ vary from $0.5\,\text{mm}$ to $2.5\,\text{mm}$ with a step of $0.333\,\text{mm}$ whereas, the range for $\boldsymbol{L}_{outer-pin}$ and $\boldsymbol{L}_{inner-pin}$ is $[0.1\,\text{mm}, 2.0\,\text{mm}]$ with a step of $0.316\,\text{mm}$. The sub-grid contains 2401 points. The constrain $\boldsymbol{R}_{outer-pin} > \boldsymbol{R}_{inner-pin}$ is managed in the MATLAB® script. For each point of the parent grid the geometry, among the possible 2041, providing the best reflection level is stored. These analyses are performed by considering a

[3]All turnstile junction's design reported in this section have the height of the rectangular waveguide fixed to $2.5\,\text{mm}$.

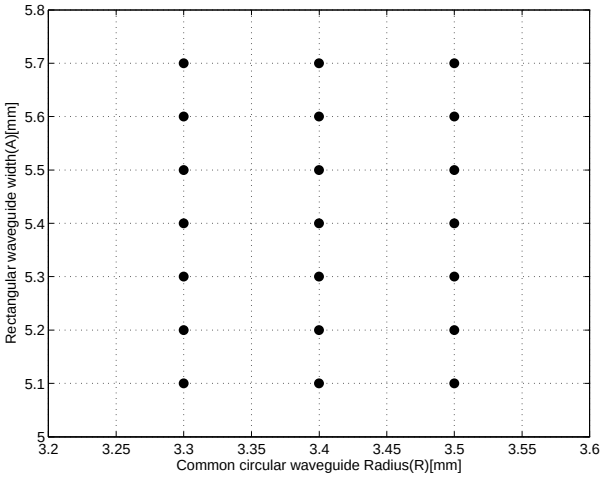

Figure 3.6. Parent grid definition for $\boldsymbol{R}$ and $\boldsymbol{A}$.

20 % bandwidth centered at 43.5 GHz[4]. Once all the sub-grid analyses have been completed, the matching pin dimensions are further optimized for each point of the parent grid starting form the corresponding best solution provided by the corresponding sub-grid analysis. In table 3.1 the results obtained before optimization and after optimization are reported. It can be noticed that the turnstile junction geometry labeled as number 8 on Table 3.1 shows the best reflection coefficient. In order to obtain a 40 %-bandwidth turnstile junction, the best geometry of the 20 %-bandwidth junction reported in Table 3.1 has been used as an initial guess. In particular, starting from the case of the 20%-bandwidth junction, the operative band considered has been enlarged step by step of 1 GHz. The relevant solution has been obtained by optimization. In this optimization, the radius $\boldsymbol{R}$ and the width $\boldsymbol{A}$ are also optimized. The 40 % bandwidth has been achieved in 13 steps. The results obtained during this optimization process are reported in Table 3.2. The frequency response of the each geometry are reported in Fig.s 3.7-3.20. It can be noticed how the two zeros are moving far from each other as the operative band increase and due to their presence the reflection level remain quite low even in a 40 % band. The geometries are reported in Table 3.2, while the geometry parameters are plotted as a function of relative bandwidth in Fig.s 3.21 -3.23. These plots show how the dimensions of the turnstile junction vary when the bandwidth increases. As one can expect, the return loss decreases (see Fig. 3.24) as a function of the bandwidth. In particular it decreases from -41.0 dB to -34.8 dB. The dimensions of the radius $\boldsymbol{R}$ and the width $\boldsymbol{A}$ increase gradually as the relative bandwidth increase (see Fig. 3.21) whereas an anomaly can be observed in the matching pin dimensions (see Fig. 3.22- Fig. 3.23).

[4]Frequency band [39, 48] GHz.

S. No	R	A	$R_{outer-pin}$		$L_{outer-pin}$		$R_{inner-pin}$		$L_{inner-pin}$		s_{11}	
			B.O	A.O	B.O	A.O	B.O	A.O	B.O	A.O	B.O	A.O
	[mm]	[mm]	[mm]	[mm]	[mm]	[mm]	[mm]	[mm]	[mm]	[mm]	[dB]	[dB]
1	3.3	5.1	2	2	0.575	0.576	1	1	1.05	1.05	-27.1	-27.2
2	3.3	5.2	2	2	0.575	0.575	1	1.001	1.05	1.05	-30.0	-30.6
3	3.3	5.3	2	2	0.575	0.576	1	1	1.05	1.05	-29.0	-29.2
4	3.3	5.4	2	1.996	0.575	0.518	1	1.084	1.05	1.039	-25.6	-26.8
5	3.3	5.5	1.5	1.776	1.05	0.793	0.5	0.799	1.05	1.123	-23.3	-28.6
6	3.3	5.6	1.5	1.565	1.05	1.017	0.5	0.559	1.05	1.025	-24.2	-28.7
7	3.3	5.7	1.5	1.517	1.05	1.087	0.5	0.51	1.05	1.016	-24.0	-28.6
8	**3.4**	**5.1**	**2.5**	**2.689**	**0.575**	**0.431**	**1**	**1.113**	**1.525**	**1.338**	**-22.9**	**-41.0**
9	3.4	5.2	2.5	2.272	0.575	0.678	1	0.832	1.525	1.575	-24.3	-30.0
10	3.4	5.3	2.5	2.547	0.575	0.534	1	1.019	1.525	1.511	-24.7	-27.6
11	3.4	5.4	2.5	2.423	0.575	0.59	1	0.922	1.525	1.637	-24.7	-30.7
12	3.4	5.5	2.5	2.394	0.575	0.485	1	0.995	1.525	1.446	-24.0	-32.3
13	3.4	5.6	2.5	2.266	0.575	0.406	1	1.124	1.525	1.26	-22.8	-28.9
14	3.4	5.7	2.5	2.615	0.575	0.46	1	1.035	1.525	1.606	-20.6	-29.3
15	3.5	5.1	2.5	2.503	0.575	0.539	1	0.968	1.525	1.488	-24.3	-25.0
16	3.5	5.2	2.5	2.579	0.575	0.546	1	1.012	1.525	1.486	-26.7	-35.6
17	3.5	5.3	2.5	2.5	0.575	0.581	1	0.972	1.525	1.546	-30.0	-34.5
18	3.5	5.4	2.5	2.5	0.575	0.575	1	1.001	1.525	1.525	-31.1	-31.8
19	3.5	5.5	2.5	2.532	0.575	0.561	1	0.992	1.525	1.618	-26.6	-34.3
20	3.5	5.6	2.5	2.495	0.575	0.514	1	1.019	1.525	1.54	-23.0	-37.2
21	3.5	5.7	2.5	2.35	0.575	0.456	1	1.057	1.525	1.48	-20.2	-25.4

Table 3.1. Twenty-one different designs of the Q-band turnstile junction. Each design refers to a single point in the parent grid of Fig. 3.6. The common circular waveguide radius and broader side of the rectangular waveguide are denoted by $\boldsymbol{R}$ and $\boldsymbol{A}$, respectively. The acronyms "B.O." and "A.O" refer to the solution before and after optimization, respectively.

This depends on the constraints on the height of the rectangular waveguide($\boldsymbol{B}$) that is fixed through out the analysis.

In Table 3.2, the geometry reported in S.No 1 has a higher reflection level as compared to the geometry reported in S.No 2, whereas the operative band for S.No 1 geometry is smaller than the operative band of S.No 2 geometry. This is due to the fact that the geometry reported in S.No 1 is obtained for 20 % bandwidth by keeping constant $\boldsymbol{R}$ and $\boldsymbol{A}$ during the optimization whereas $\boldsymbol{R}$ and $\boldsymbol{A}$ are also optimized for the geometry reported in S.No 2. Therefore, the latter one yields a slightly better reflection level for the 23.3 % bandwidth.

S.No	R	A	$R_{outer-pin}$	$L_{outer-pin}$	$R_{inner-pin}$	$L_{inner-pin}$	f_{start}	f_{center}	Rel. BW	s_{11}
	[mm]	[mm]	[mm]	[mm]	[mm]	[mm]	[GHz]	[GHz]	[%]	[dB]
1	3.4	5.1	2.689	0.431	1.113	1.338	39	43.5	20.7	-41.0
2	3.313	5.157	2.693	0.377	1.119	1.319	38	43.0	23.3	-42.9
3	3.315	5.196	2.604	0.39	1.101	1.313	37	42.5	25.9	-41.7
4	3.326	5.29	2.42	0.443	1.047	1.318	36	42.0	28.6	-40.8
5	3.322	5.32	2.343	0.457	1.035	1.298	35.0	41.5	31.3	-39.1
6	3.354	5.39	2.271	0.511	0.991	1.33	34.5	41.3	32.7	-38.2
7	3.388	5.409	2.371	0.475	1.032	1.353	34.0	41.0	34.1	-37.9
8	3.434	5.45	2.464	0.457	1.059	1.39	33.5	40.8	35.6	-37.4
9	3.432	5.465	2.384	0.49	1.028	1.388	33.2	40.6	36.5	-36.7
10	3.446	5.495	2.375	0.5	1.022	1.403	33.0	40.5	37.0	-36.6
11	3.446	5.499	2.38	0.491	1.03	1.395	32.7	40.4	37.9	-36.0
12	3.434	5.492	2.354	0.488	1.032	1.375	32.5	40.3	38.5	-35.7
13	3.450	5.511	2.34	0.508	1.017	1.39	32.2	40.1	39.4	-35.4
14	3.450	5.532	2.326	0.505	1.02	1.385	32.0	40.0	40.0	-34.8

Table 3.2. Roadmap of the broad-band turnstile-junction design in the Q band in order to achieve a 40 % bandwidth centered at 40 GHz. Operative band is defined as $[f_{start}, 48]$ GHz for each geometry. The acronym "Rel. BW" denotes the relative bandwidth.

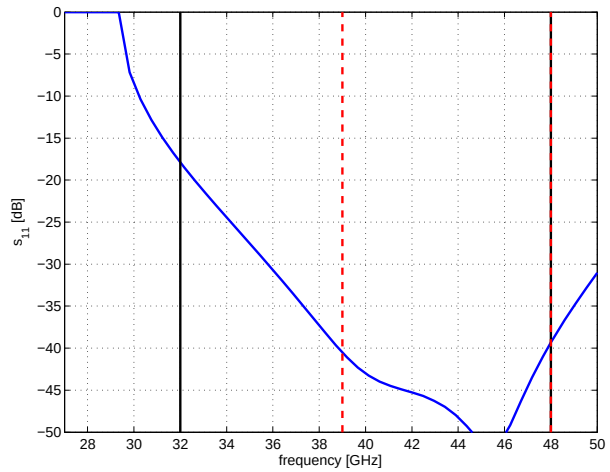

Figure 3.7. Reflection coefficient (s_{11}) at the common circular waveguide of the broadband turnstile junction S.No 1 of Tab. 3.2 (20.7 % bandwidth centered at 43.5 GHz). The vertical black(solid) lines refer to the 40 % band centered at 40 GHz, whereas the other vertical red(dash) lines denote the operative band.

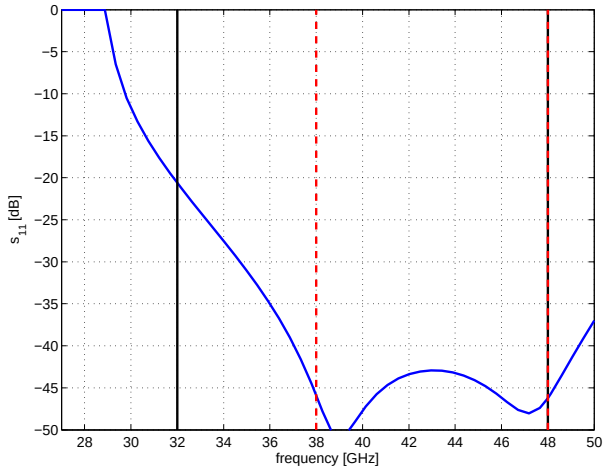

Figure 3.8. Reflection coefficient (s_{11}) at the common circular waveguide of the broadband turnstile junction S.No 2 of Tab. 3.2 (23.3 % bandwidth centered at 43 GHz). The vertical black(solid) lines refer to the 40 % band centered at 40 GHz, whereas the other vertical red(dash) lines denote the operative band.

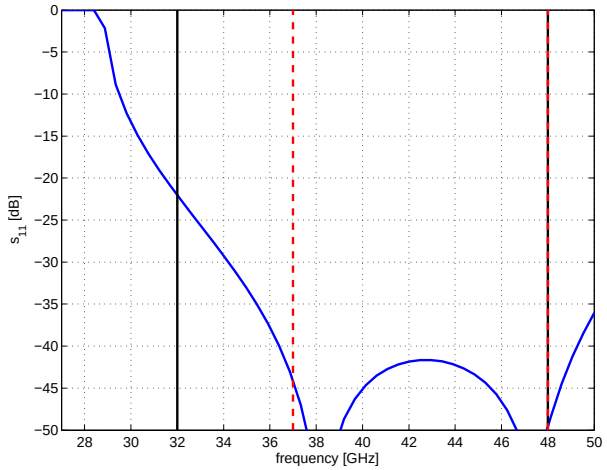

Figure 3.9. Reflection coefficient (s_{11}) at the common circular waveguide of the broadband turnstile junction S.No 3 of Tab. 3.2 (25.9 % bandwidth centered at 42.5 GHz). The vertical black(solid) lines refer to the 40 % band centered at 40 GHz, whereas the other vertical red(dash) lines denote the operative band.

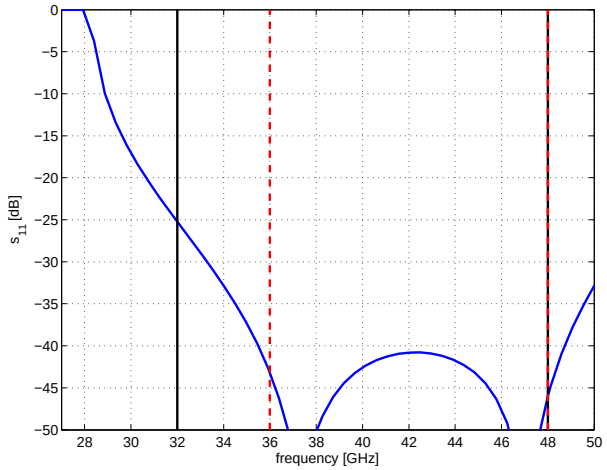

Figure 3.10. Reflection coefficient (s_{11}) at the common circular waveguide of the broadband turnstile junction S.No 4 of Tab. 3.2 (28.6 % bandwidth centered at 42 GHz). The vertical black(solid) lines refer to the 40 % band centered at 40 GHz, whereas the other vertical red(dash) lines denote the operative band.

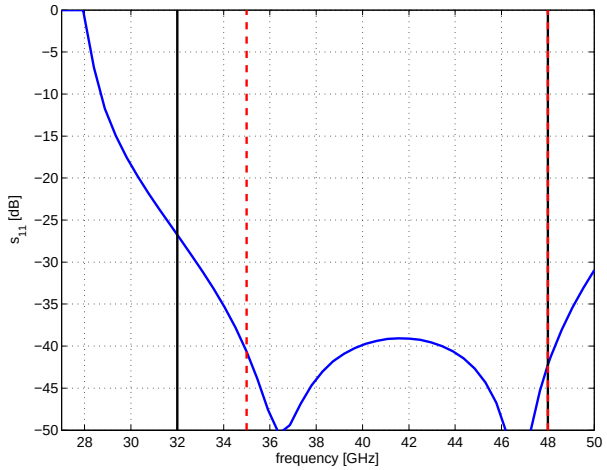

Figure 3.11. Reflection coefficient (s_{11}) at the common circular waveguide of the broadband turnstile junction S.No 5 of Tab. 3.2 (31.3 % bandwidth centered at 41.5 GHz). The vertical black(solid) lines refer to the 40 % band centered at 40 GHz, whereas the other vertical red(dash) lines denote the operative band.

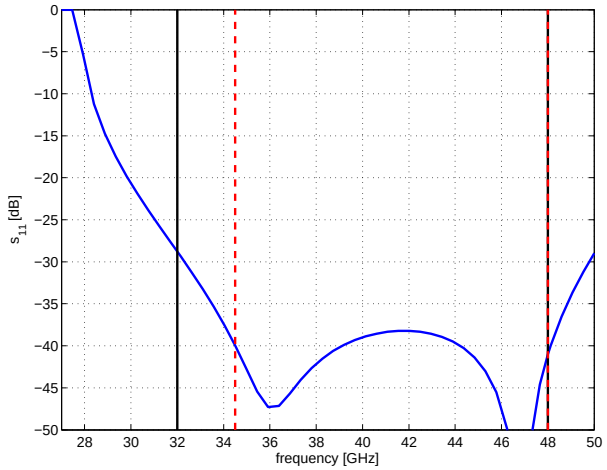

Figure 3.12. Reflection coefficient (s_{11}) at the common circular waveguide of the broadband turnstile junction S.No 6 of Tab. 3.2 (32.7 % bandwidth centered at 41.3 GHz). The vertical black(solid) lines refer to the 40 % band centered at 40 GHz, whereas the other vertical red(dash) lines denote the operative band.

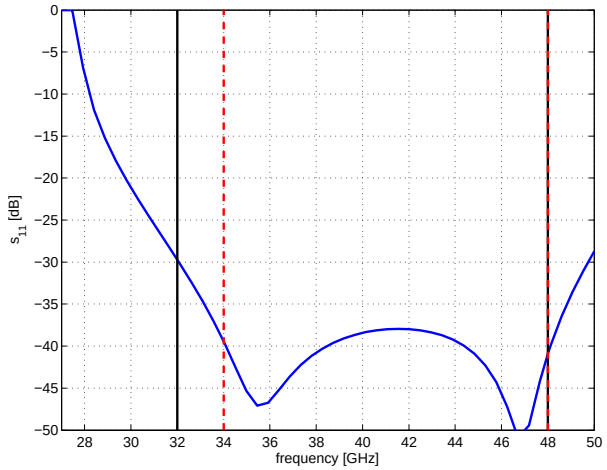

Figure 3.13. Reflection coefficient (s_{11}) at the common circular waveguide of the broadband turnstile junction S.No 7 of Tab. 3.2 (34.1 % bandwidth centered at 41 GHz). The vertical black(solid) lines refer to the 40 % band centered at 40 GHz, whereas the other vertical red(dash) lines denote the operative band.

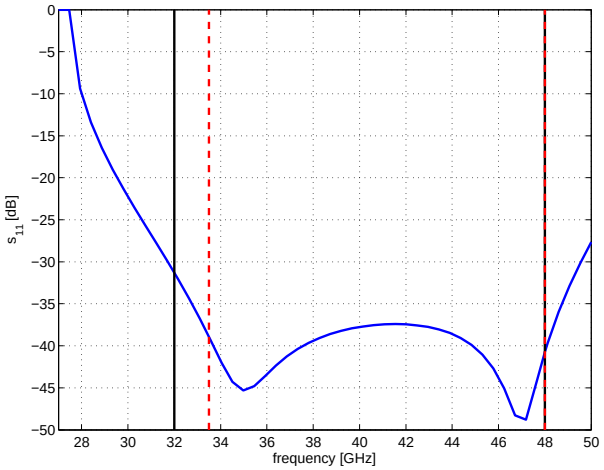

Figure 3.14. Reflection coefficient (s_{11}) at the common circular waveguide of the broadband turnstile junction S.No 8 of Tab. 3.2 (35.6 % bandwidth centered at 40.8 GHz). The vertical black(solid) lines refer to the 40 % band centered at 40 GHz, whereas the other vertical red(dash) lines denote the operative band.

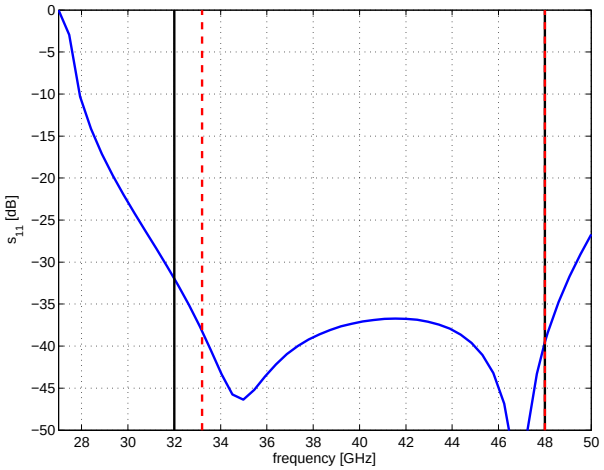

Figure 3.15. Reflection coefficient (s_{11}) at the common circular waveguide of the broadband turnstile junction S.No 9 of Tab. 3.2 (36.5 % bandwidth centered at 40.6 GHz). The vertical black(solid) lines refer to the 40 % band centered at 40 GHz, whereas the other vertical red(dash) lines denote the operative band.

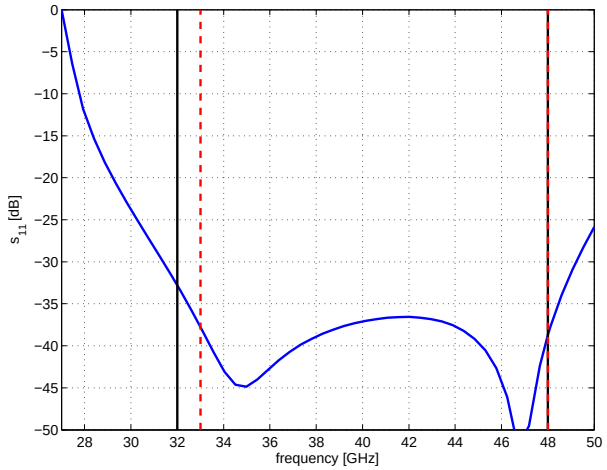

Figure 3.16. Reflection coefficient (s_{11}) at the common circular waveguide of the broadband turnstile junction S.No 10 of Tab. 3.2 (37 % bandwidth centered at 40.5 GHz). The vertical black(solid) lines refer to the 40 % band centered at 40 GHz, whereas the other vertical red(dash) lines denote the operative band.

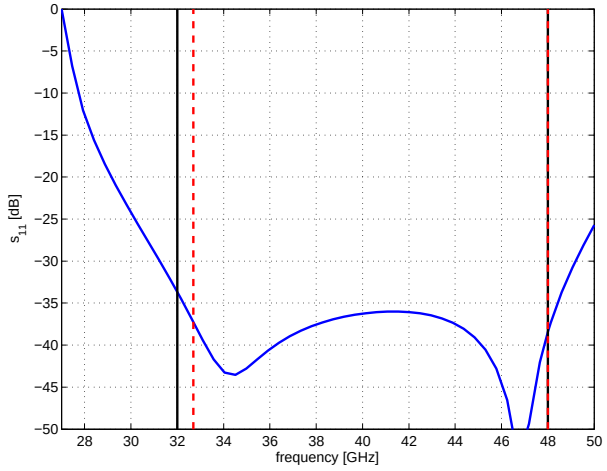

Figure 3.17. Reflection coefficient (s_{11}) at the common circular waveguide of the broadband turnstile junction S.No 11 of Tab. 3.2 (37.9 % bandwidth centered at 40.4 GHz). The vertical black(solid) lines refer to the 40 % band centered at 40 GHz, whereas the other vertical red(dash) lines denote the operative band.

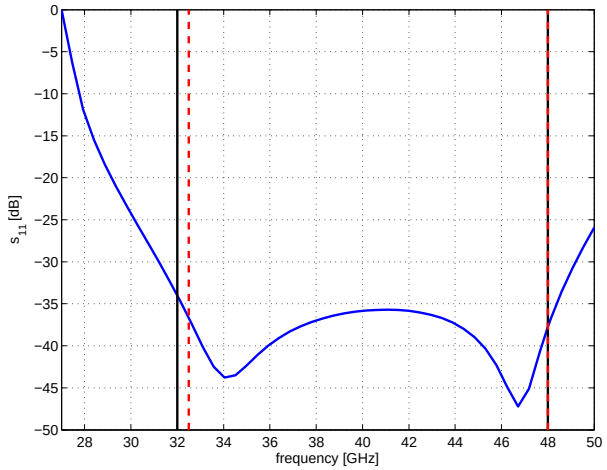

Figure 3.18. Reflection coefficient (s_{11}) at the common circular waveguide of the broadband turnstile junction S.No 12 of Tab. 3.2 (38.5 % bandwidth centered at 40.3 GHz). The vertical black(solid) lines refer to the 40 % band centered at 40 GHz, whereas the other vertical red(dash) lines denote the operative band.

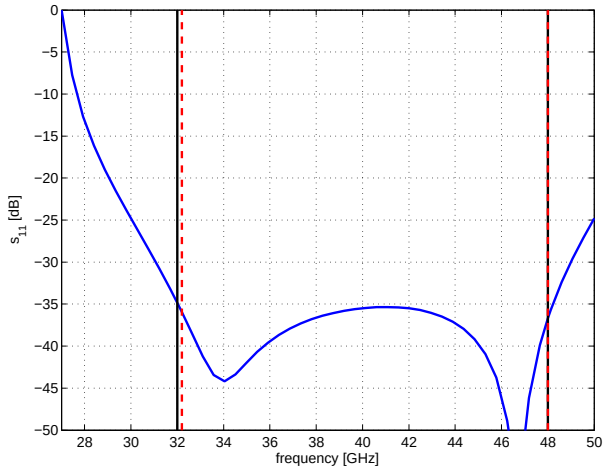

Figure 3.19. Reflection coefficient (s_{11}) at the common circular waveguide of the broadband turnstile junction S.No 13 of Tab. 3.2 (39.4 % bandwidth centered at 40.1 GHz). The vertical black(solid) lines refer to the 40 % band centered at 40 GHz, whereas the other vertical red(dash) lines denote the operative band.

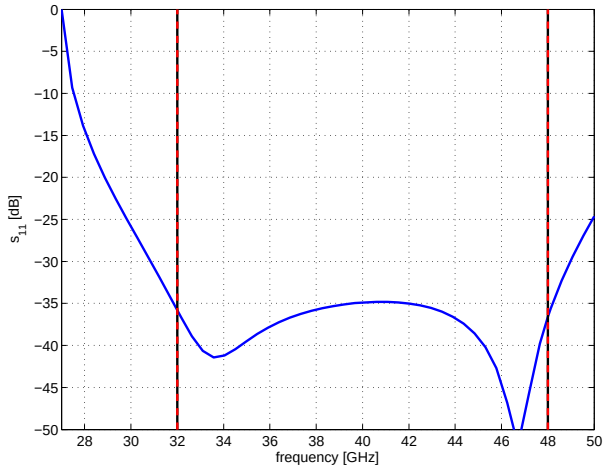

Figure 3.20. Reflection coefficient (s_{11}) at the common circular waveguide of the broadband turnstile junction S.No 14 of Tab. 3.2 (40 % bandwidth centered at 40 GHz). The vertical black(solid) lines refer to the 40 % band centered at 40 GHz, whereas the other vertical red(dash) lines denote the operative band.

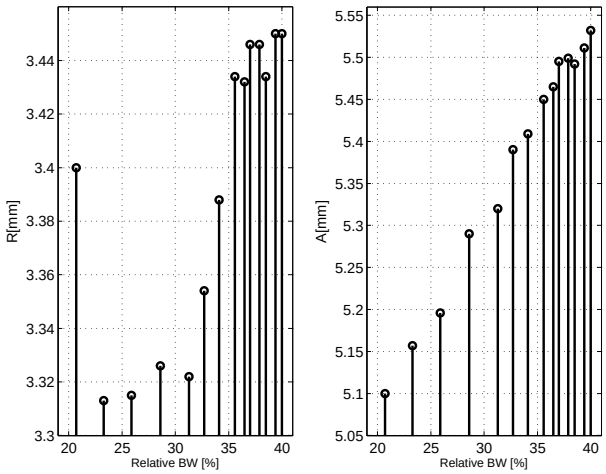

Figure 3.21. Broad band turnstile junction's common circular waveguide($\boldsymbol{R}$) and the broader side of the rectangular waveguide(A) geometrical variations as a function of the relative bandwidth.

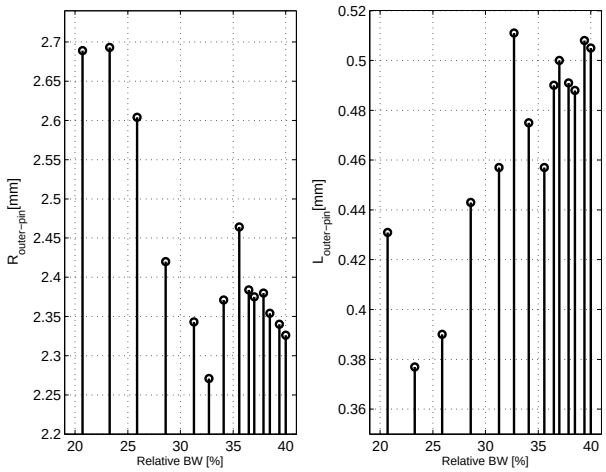

Figure 3.22. Broad band turnstile junction's outer pin radius($\boldsymbol{R_{outer-pin}}$) and length($\boldsymbol{L_{outer-pin}}$) geometrical variations as a function of the the relative bandwidth.

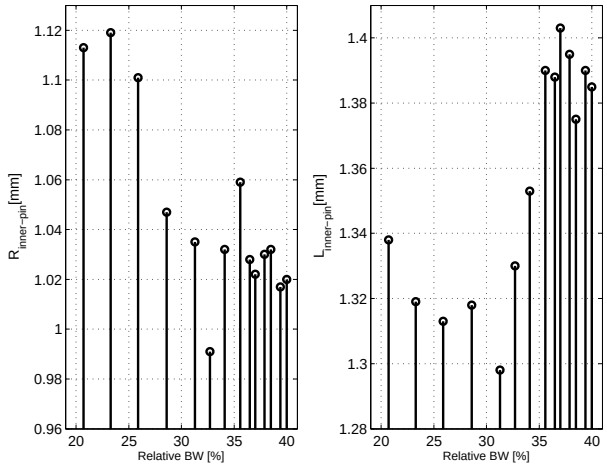

Figure 3.23. Broad band turnstile junction's inner pin radius($R_{inner-pin}$) and length($L_{inner-pin}$) geometrical variations as a function of the relative bandwidth.

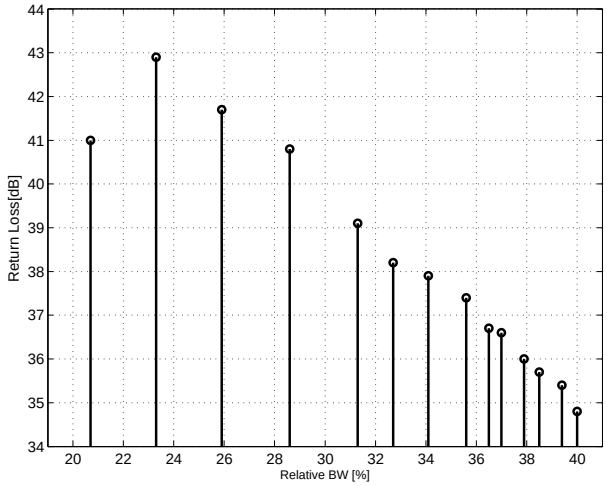

Figure 3.24. Broad band turnstile junction's return loss variation as a function of the relative bandwidth.

3.4 Stokes Parameter's Formulation

In this section, the electrical response of the OMT is described in terms of relationship between input and output Stokes parameters. The same formulation and methodology used in the polarizer case are followed in this section. The generic expression of the incident electric field vector at the common waveguide circular/rectangular port of the OMT is given as,

$$\mathbf{E}_1^{\mathbf{inc}} = E_x\hat{\mathbf{x}} + E_y\hat{\mathbf{y}}$$

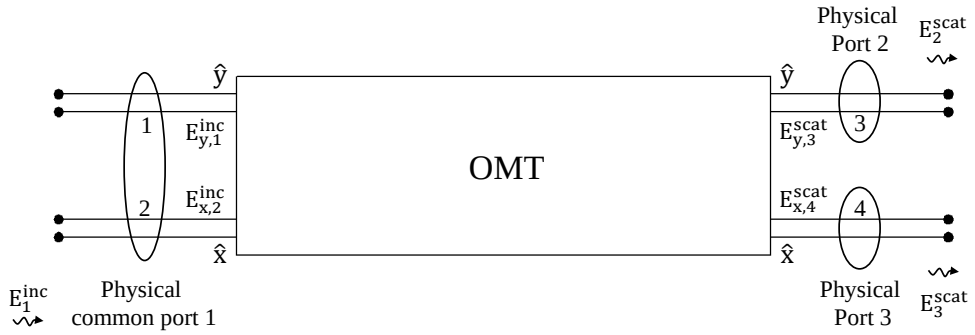

Figure 3.25. Four electrical port block diagram of the OMT (the three OMT waveguide ports are also reported).

It has to be noticed that the two linearly polarized signals E_x and E_y are proportional to the two circular polarizations collected by the horn, since it is understood that the OMT is mounted inside a dual-circular polarization receiver with a polarizer mounted in front of it (see Fig. 1.1). The scattered field components along $\hat{\mathbf{y}}$ and $\hat{\mathbf{x}}$ direction at physical port 2 and 3(see Fig. 3.25) of the OMT are given as,

$$\begin{aligned} E_2^{scat} &= s_{31}E_y + s_{32}E_x \\ E_3^{scat} &= s_{41}E_y + s_{42}E_x \end{aligned}$$

These signals are, then, routed to a correlation unit in order ot measure the Stokes parameters Q_m and U_m that are proportional to the real and imaginary parts of the product $E_3^{scat}(E_2^{scat})^*$, respectively. The detail derivation is reported in B.1. Only the final derived expression of the Q_m and U_m Stokes parameters are reported here.

$$\begin{bmatrix} Q_m \\ U_m \end{bmatrix} = \mathbf{H} \cdot \begin{bmatrix} Q \\ U \end{bmatrix} + \mathbf{K} \cdot \begin{bmatrix} I \\ V \end{bmatrix}$$

where

$$\mathbf{H} = \begin{bmatrix} H_{QQ} & H_{QU} \\ H_{UQ} & H_{UU} \end{bmatrix}, \ \mathbf{K} = \begin{bmatrix} K_{QI} & K_{QV} \\ K_{UI} & H_{UV} \end{bmatrix}$$

$$\begin{aligned} H_{QQ} &= \Re\{s_{41}s_{32}^* + s_{42}s_{31}^*\} \\ H_{QU} &= \Im\{-s_{41}s_{32}^* + s_{42}s_{31}^*\} \\ H_{UQ} &= -\Im\{s_{41}s_{32}^* + s_{42}s_{31}^*\} \\ H_{UU} &= \Re\{-s_{41}s_{32}^* + s_{42}s_{31}^*\} \end{aligned}$$

and

$$K_{QI} = \Re\{s_{41}s_{31}^* + s_{42}s_{32}^*\}$$

$$\begin{aligned} K_{QV} &= \Re\{s_{42}s_{32}^* - s_{41}s_{31}^*\} \\ K_{UI} &= -\Im\{s_{41}s_{31}^* + s_{42}s_{32}^*\} \\ K_{UV} &= -\Im\{s_{42}s_{32}^* - s_{41}s_{31}^*\} \end{aligned}$$

In order to obtain an OMT that is only sensitive to the polarized component, the diagonal terms of the **H** matrix should be equal to 1 and the off-diagonal terms should be equal to zero and this can be only achieved when the OMT design have very low cross-coupling terms (ideally, $s_{41} = s_{32} = 0$) and very good channel equalization (ideally, $s_{31} = s_{42} = 1$). Since the Q and U Stokes parameters are also affected by the other Stokers parameters I and V through matrix **K**, the latter matrix should also contain very low elements. Minimization of the OMT cross-couplings is also essential in this regard.

If the cascade of the polarizer and the OMT is considered as a single block/entity, then the Stokes parameter analysis remains the same as the one reported in this section.

3.5 W-band Multi-Layer OMT

The multi-layer architecture of the OMT in conjunction with the wire spark erosion technique provides a very compact and accurate design with high repeatability. This approach provides the parallelism in manufacturing that reduces both the machining process time and the over all cost. Therefore, it can be manufactured in a medium-large scale with high accuracy and it is very suitable for cluster applications. A multi-layer W-band OMT cluster with 7-elements has been designed and manufactured. The experimental results reported in section 3.5.4 demonstrate the validity of the proposed architecture.

By exploiting a multi-layer architecture, a two-fold symmetric-coupling OMT configuration based on the turnstile junction with a properly arranged recombination network has been conceived in order to obtain both a good equalization and a high isolation between the two channels in a large operative bandwidth (30 %). The design of the turnstile junction of the W-band OMT has been carried out by exploiting the results obtained for the Q-band junction reported in the previous sections.

3.5.1 Architecture

The multi-layer W-band OMT waveguide geometry is shown in Fig. 3.26. It is colored in such a way that all the particulars can be easily recognized in the corresponding exploded-view of Fig. 3.27 (the mounting holes are also shown). A part from the input and output sections, the thickness of the various layers is 0.5 mm (all-but-gray) and 1 mm(gray). These values have been selected during the design

stage as the best trade-off between performance and commercial availability of the metal sheets. The waveguide configuration is based on a turnstile junction that lays on the yellow and green layers. The circular input waveguide (diameter 2.62 mm) of the turnstile junction is manufactured on the brown, red and orange layers. One pair of the opposite rectangular outputs (2.144 mm × 1 mm) of the turnstile junction is routed to the upper levels (red and orange) by means of a matched staircase of waveguide E-plane steps. It undergoes two subsequent 90° H-plane piecewise-uniform bends and then it is routed back to the yellow and green layers, where the recombination occurs by means of a matched E-plane T junction. The other orthogonal pair of waveguides follows a dual path down through the lower blue and violet layers and then back up to the yellow and green layers. The matching element of the turnstile junction is manufactured as a metal cylinder (diameter 1.186 mm) which is placed into a press fit hole located in the center of the blue layer. It should be noted that the two recombination structures do not cross because they are placed two-levels apart. Moreover, they are rigorously identical as far as the single-mode is concerned. Although several evanescent higher order modes are excited by the various waveguide discontinuities, the spacing between them has been designed so that such modes are localized. Therefore, they do not produce any significant degradation to neither the channel equalization nor the cross-coupling or isolation performance. In other words, the two-fold symmetry of the turnstile junction is preserved. Two metal layers for each rectangular waveguide level (red-orange, yellow-green and blue-violet) are required in order to obtain a low-reflection coefficient in the 30 % bandwidth for both the staircase E-plane step transitions and the mitered E-plane T junctions without additional matching elements. A smaller number of layers can be adopted if an OMT design with a narrower bandwidth is required. The output waveguide sections of the T-junctions are manufactured on both the blue and violet layers in order to obtain a suitable phase condition to connect the second-order waveguide step transformer (gray and white) to the output WR10 standard waveguides (black). It should be pointed out that both rectangular outputs lay on the same reference plane. This feature is very useful when the equalization of the subsequent device chain is also important e.g. correlation polarimeters.

3.5.2 Simulation Results

The various discontinuities have been analyzed exploiting full-wave analysis tools based on the Method of Moments. The various OMT components have been designed using parametric charts to define a good guess and, subsequently, optimization algorithms to refine the solution.

A significant design constrain is the limited set of commercially-available thickness values for the metal sheets. Nevertheless, very good matching levels have been

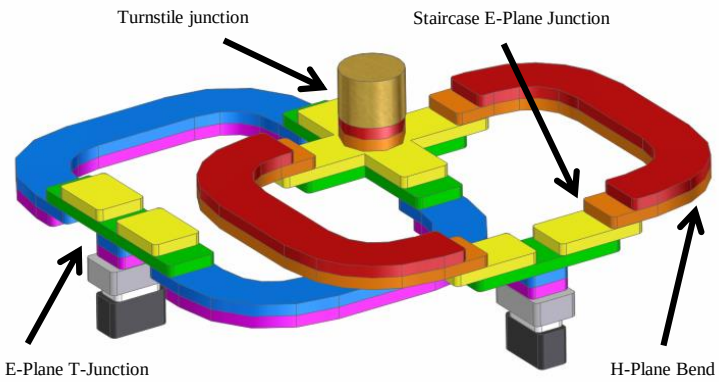

Figure 3.26. Internal waveguide configuration of the multi-layer W-band OMT. The input circular ($\Phi 2.62\,\mathrm{mm}$) and output WR10 waveguides are colored in brown and black, respectively. Both the turnstile and the T-junctions lay on the yellow and green layers.

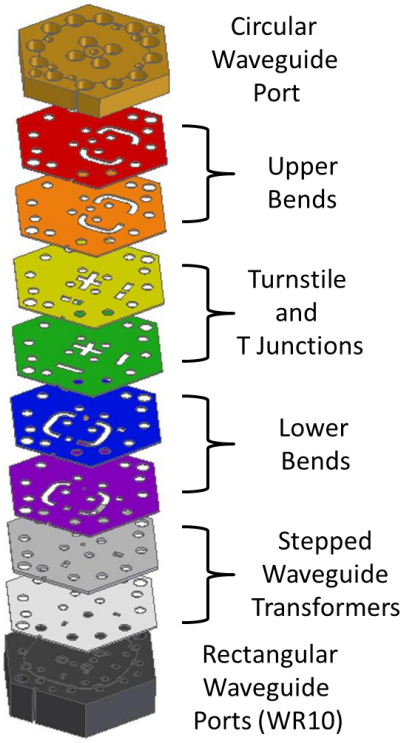

Figure 3.27. Exploded view of the multi-layer W-band OMT. The colors are consistent with Fig. 3.26. All the metal layers only exhibit through holes with the required shape.

obtained for the various discontinuities in the 30 % bandwidth centered at $94\,\mathrm{GHz}$ i.e. $-34\,\mathrm{dB}$ for the turnstile junction, $-46\,\mathrm{dB}$ for the staircase E-plane junction,

and $-42\,\mathrm{dB}$ for the E-plane T-junction with output adapters. A reflection level of $-55\,\mathrm{dB}$ has been obtained for the H-plane piecewise uniform bends. Simulatation results are reported in Fig. 3.28, 3.29, 3.30. The cross-coupling terms between the two polarizations are not reported since the simulated curves are lower than $-80\,\mathrm{dB}$.

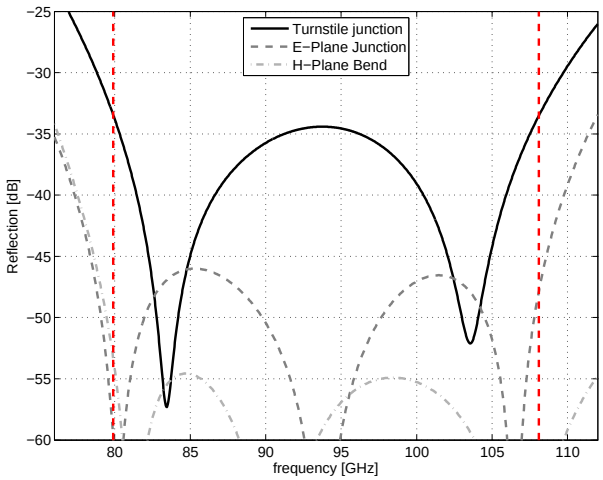

Figure 3.28. Computed reflection level for the W-band turnstile junction, E-plane junction and H-plane piecewise uniform bend. The vertical dash lines denote the operative frequency band.

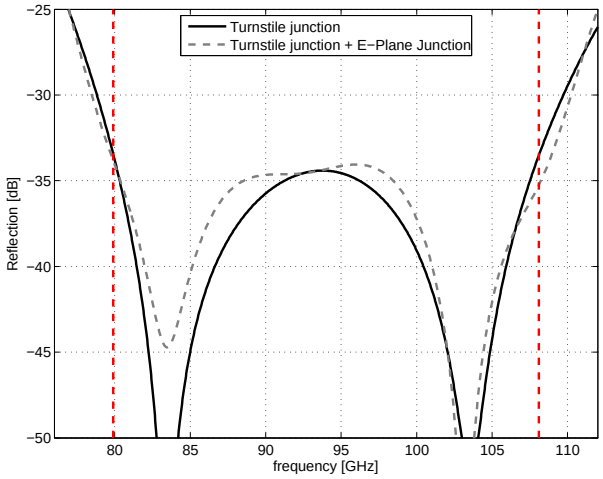

Figure 3.29. Computed reflection level for the W-band turnstile junction and the turnstile junction cascaded with the E-plane junction. The vertical dash lines denote the operative frequency band.

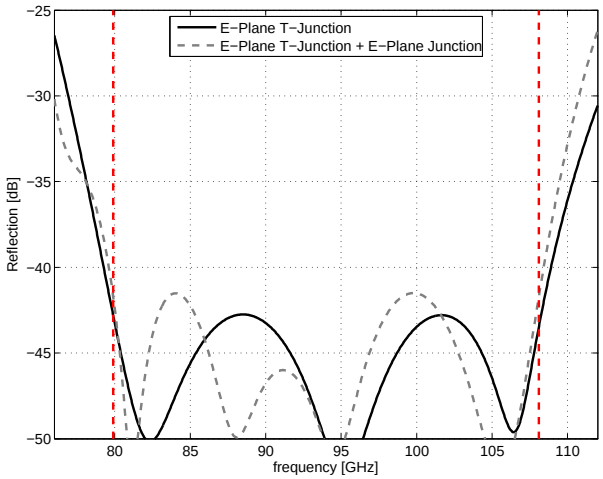

Figure 3.30. Computed reflection level for E-Plane T-junction and E-Plane T-Junction with E-Plane junction. The vertical dash lines identify the operative frequency band.

3.5.3 Prototype

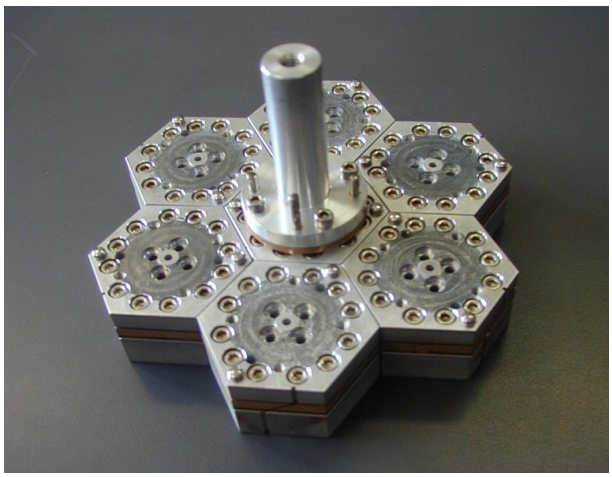

Figure 3.31. Multi-layer OMT cluster with 7 modules arranged in a equilateral triangular lattice (step 42 mm). The set of measurement loads is connected to the central module

Several prototypes of the W-band multilayer OMT has been manufactured through wire spark erosion applied to phosphor bronze plates (see Fig. 3.32). With reference to Fig. 3.32, the average radius of the bends of the recombination networks has been selected in order to provide a distance of 16 mm between the rectangular outputs. This spacing is necessary to accommodate the two standard WR10 connection flanges. Smaller devices can be designed if proper custom flanges are adopted. The

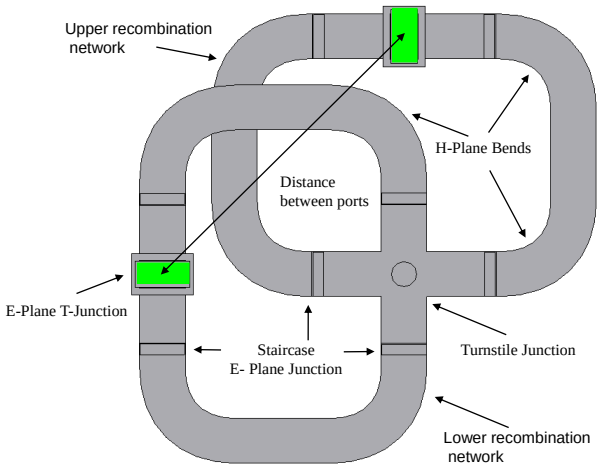

Figure 3.32. Bottom view of the OMT. Various parts of the OMT are indicated by arrows. Distance between two rectangular waveguide output ports is 16 mm

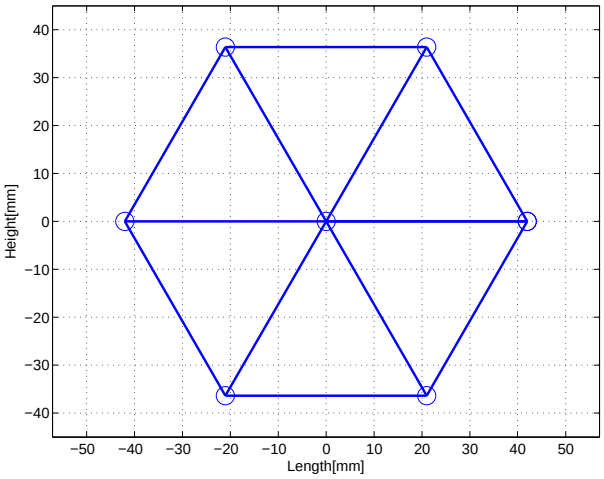

Figure 3.33. Seven OMTs arrangement in an equilateral triangular lattice (step 42 mm). Circles in the plot refers to the positions of the common circular waveguides of the seven OMTs.

mounting screws ($M3$ and $M2.5$) and the alignment dowels are also visible. It should be noted that the manufacturing time of the seven modules of Fig. 3.31, is basically equal to the manufacturing time of a single one. This happens because several samples (seven or more) of each metal layer in Fig. 3.27 are manufactured at the same time from a stack of metal sheets using the wire erosion technique. Besides reducing the manufacturing time and cost, this technique provides a set of identical devices, therefore, it is very suitable for cluster applications. A curvature radius of 0.2 mm has been considered in all the inner shaped of Fig. 3.27, owing to the diameter of the electric discharge wire. The hexagonal external profile of the OMT has been

selected to obtain the equilateral triangular lattice configuration shown in Fig. 3.33, which is the best one in terms of focal plane density. The lattice step and the module thickness are 42 mm and 23.5 mm, respectively.

3.5.4 Experimental Results

The 4×4 scattering matrix of the OMT is obtained exploiting a measurement technique developed in the past by the AE&ED group of IEIIT-CNR. In this technique [42], the two output rectangular ports of the OMT are connected to the two ports of the VNA whereas the common circular port is loaded with five different loads, i.e.

- Matched load
- Short circuit load
- Short circuit load shifted by a line
- Reactive load
- Reactive load moved back by the line

Thanks to this calibration technique, the common circular waveguide port of the OMT is not connect to the VNA , moreover the accuracy produced is greater than the standard adapter–removal technique. In Fig. 3.34-3.37, the experimental results obtained for one of the seven W-band prototypes are reported. The measured reflection level is lower than $-22\,\mathrm{dB}$ (see Fig. 3.34). The discrepancy with the simulated one is due to the manufacturing inaccuracy. The cross-coupling for both polarization is lower than $-42\,\mathrm{dB}$ in the whole operative band, as reported in Fig. 3.35. The insertion loss is $-1.2\,\mathrm{dB}$ at lower frequency and $-0.8\,\mathrm{dB}$ at the higher frequencies, as reported in Fig 3.36. The magnitudes of the scattering terms s_{31} and s_{42} are almost identical and this guarantees a very good channel equalization. Simulation for the insertion loss is performed with an equivalent resistivity of $10\,\mu\Omega\mathrm{cm}$. It can be seen that the computed curve is quite above the measurement curves. It reveals that the resistivity of the used material(phosphor bronze) is quite higher.

In order to study the behavior of the insertion loss, plate number 1 to 5 and 10 (see Fig. 3.27) are replaced with silver plated metallic plates. In this way, the upper recombination network is formed by the silver plated layers whereas the lower recombination network is formed by the phosphor bronze layers. In this condition, an improvement in the insertion loss should be observed in one channel whereas the other channel should be unaffected. The measured insertion losses reported in Fig. 3.37 confirm this situation. In this figure, only the transmission coefficient for the polarization is reported experiencing the silver plated channel, s_{42}, is reported. It

can be noticed that silver platting improves the insertion loss and measurements are more consistent with the computed results. However, since the OMT is designed in W band, a small amount of deformation in the component due to the silver platting may deteriorate its performance. Therefore a good controlled silver plating process is required in this regards. Instead of using silver plating, insertion loss can also be improved by using different materials that have good surface equivalent resistivity e.g. all aluminum metallic plates can be used instead of phosphor bronze ones.

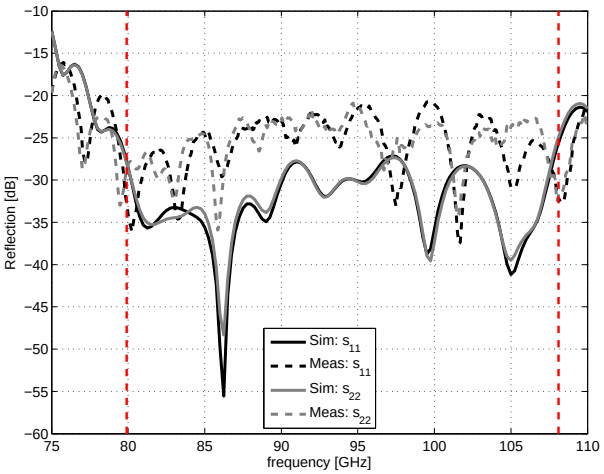

Figure 3.34. Measured (dash-lines) and simulated (solid-lines) transmission coefficient of one W-band prototype for both polarizations (s_{11} and s_{22}). The vertical dash lines denote the operative frequency band.

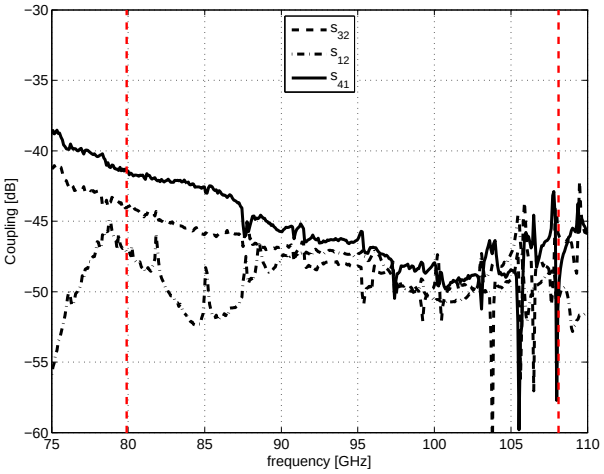

Figure 3.35. Measured cross-coupling coefficients and isolation of one W-band prototype (s_{32}, s_{12} and s_{41}). Computed results are not reported because they are lower than $-80\,\mathrm{dB}$. The vertical dash lines denote the operative frequency band.

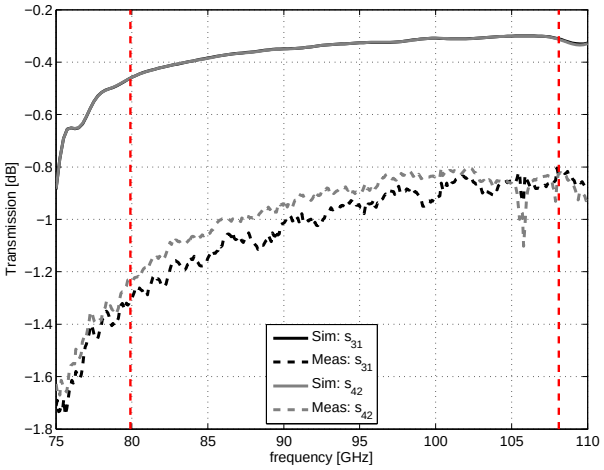

Figure 3.36. Measured (dash-lines) and simulated (solid-lines) transmission coefficient of one W-band prototype for both polarizations (s_{31} and s_{42}). Simulations have been performed with an equivalent resistivity of $10\,\mu\Omega\text{cm}$. The vertical dash lines denote the operative frequency band.

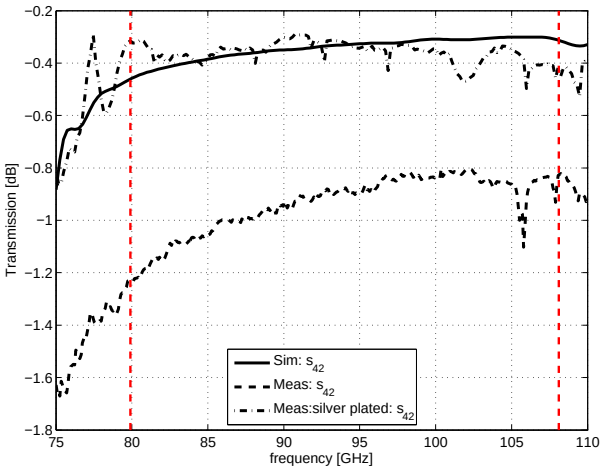

Figure 3.37. Transmission coefficient of one W-band prototype without and with silver-plating for one polarization (s_{42}). Simulations have been performed with an equivalent resistivity of $10\,\mu\Omega\text{cm}$. The vertical dash-dotted lines denote the operative frequency band.

Chapter 4

COM Automation for Commercial EM Tools

4.1 Introduction

In back 90s, it was a common practice that researchers developed their own tools in FORmula TRANslation (FORTRAN) in order to analyze the performance of a component before fabrication. These in-house developed tools were quite specific for a particular problem. With the passage of time as the technology evolves and new languages invented, the researchers have migrated to c/c++ and, eventually, to MATLAB®. In this era, when commercial EM softwares like CST-MWS, HFSS, FEKO are available, researchers exploit them along with their own in-house developed tools. Using these EM softwares, any kind of complex geometry can be created with the help of few mouse clicks and, then, this Computer-Aided Design (CAD) can be analyzed with certain boundary conditions. Obviously, commercial EM tools are very easy to use, but in terms of computation time they are slower than the in-house developed tools. The speed limitation can be avoided by means of multi-core processors or by exploiting Graphics Processing Unit (GPU). For example, these acceleration features are already available in CST-MWS for the time domain solver. Although commercial EM softwares provide a high degree of flexibility in terms of CAD designing, post processing, parametric analysis and optimization, nevertheless an end-user feels a bottleneck when more control are required over EM softwares. For instance, a specific design activity can require:

- to use a particular optimization algorithm or a self developed optimization algorithm;
- to save the results in a particular manner for the post processing;
- to plot the results in a custom way;

- to decompose the structure in several domains in order to analyze each domain through both in-house developed tools and commercial EM softwares and, then, to combine the results in order to obtain the complete performance of the component/system.

Definitely, for the later cases an end-user can perform these operations manually. However, if all the processing has to be repeated several times during the design stage, it will be very difficult to handle it without any human error. Indeed, apart from the tediousness it is quite probable to commit a mistake in handling the data manually.

In this perspective, some tools performing automation among MATLAB® and the commercial EM software through various ways have been recently developed. Using these automation tools all the above mentioned problems can be addressed very easily. In the subsequent section the existing approaches available in the literature are briefly discussed. In the later sections the Component Object Model Electromagnetic Automation Tool (COM-EM-AT) developed in this doctoral program is introduced. Its features are described in details with the help of simple examples and flow charts. The literal meaning of *automation* is the technique of making a process operating automatically. The COM automation refers to an automation for the COM protocol, i.e. it allows one application to control the objects exported by another application.

4.2 Different Approaches for EM Automation

Automation among MATLAB® and EM software has been exploited in different ways since a quite long time. For instance, parameter optimization with Genetic Algorithm (GA) using HFSS is reported in [43]. In this paper the authors exploit a macro to update the parameter during the optimization. In [44] the authors perform the automation for CST-MWS, HFSS and FEKO exploiting different techniques depending on the specific EM software. For instance, in FEKO automation the authors update the parameters in the text file that is later read by FEKO. For CST-MWS and HFSS the authors studied how these two softwares create a Visual Basic for Applications (VBA) code and, then, they recreate this code. In [45] automation among MATLAB® and HFSS is reported using GA. In this paper the authors focused on the design and on the results achievable through this automation approach. The automation approach presented in this paper is roughly the same as the one described in [43]. In [46] the authors introduced a tool named NEMO that can exploit several optimization algorithms, like fminsearch, GA real and Particle Swarm Optimization (PSO) real. Among all the above mentioned papers, only [44] focuses on the automation approach itself instead of mainly consider the design results achievable through automation. Although the approach described in this paper is quite

promising, it requires the knowledge of VBA.

4.3 COM Automation

The design of passive components involves several stages, each stage being executed by a specific application. For instance, MATLAB® can be required for the optimization, CST-MWS for the EM analysis and PowerPoint for presenting the analysis plot. Definitely, each application can be handled separately, but thanks to the Component Object Model (COM), that provides the application integration feature, it is possible to allow one application to control the objects exported by another application. In plain words, it is possible to control CST-MWS and PowerPoint from MATLAB® or vice versa by using COM. The functionality of the COM is defined by one or more interfaces that consist of properties, methods and events. The application that uses the COM object is called COM client, whereas the application that exposes the COM functionality for use is called COM server.

In the following discussion MATLAB® is considered as a COM client, whereas the remaining applications (e.g. CST-MWS, HFSS, PowerPoint) are considered as COM servers, as reported in Fig. 4.1. In this figure, a global picture of the COM automation is reported. The integration among in-house developed tool, EM software and PowerPoint produces a quite powerful EM application package.

In order to easy the COM exploitation and make it more oriented towards MATLAB® users, a tool named Component Object Model Electromagnetic Automation Tool (COM-EM-AT) has been created. The COM-EM-AT hides all implementation details inside the functions and an end-user needs to only provide the required parameters. This tool contains about 140 functions that are categorized in two groups on the basis of their required input parameters. One group accepts all the necessary parameters as input arguments, whereas the other accepts a *struct* data-type argument. The reason for this classification is that the first category contains those functions that require a small number of parameters that can be passed as function arguments[1]. Conversely, those functions requiring many parameters in order to be configured are placed in the second category[2]. Indeed, for this kind of functions the end-user typically wants to vary a few parameter values from the corresponding default ones. Therefore, for these functions there is no need to define all the fields of the structure but only those fields the user wants to initialize, while the others are automatically set to their default values inside the function. An example can be seen in Listing 4.1 that is explained in details in the following section, where the COM automation tools for CST-MWS and HFSS are discussed in detail from

[1] for example f_CreateBrick and f_PickFaceFromId

[2] for example f_CreatePort and f_CreateSolver.

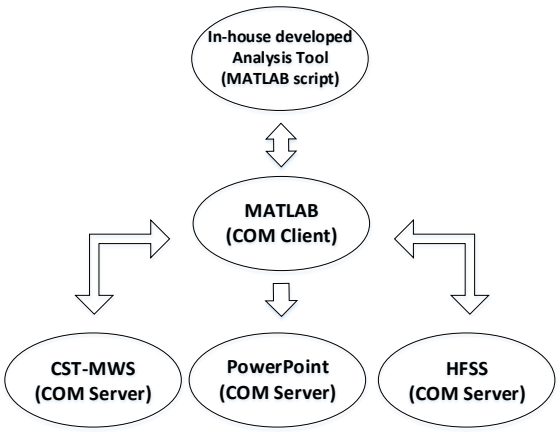

Figure 4.1. COM client and server configuration.

scratch. At the end of this section a complete example of COM-EM-AT is also given in order to show the effectiveness of the tool developed.

4.3.1 COM Automation for CST-MWS

The instance of a COM object in MATLAB® can be created with the *actxserver* function. It requires an application ID of the program. As an example, the application ID of CST is *CSTStudio.application*. The actxserver function returns a handle to the object's main interface, The interface is used to access the methods, properties and events of the object, whose details can be found in the application documentation. The interface method can be called by using the *invoke* function.

The CST DESIGN ENVIRONMENT provides the COM support and its application object can be obtained in the following way

```
oCST_Studio = actxserver('CSTStudio.application');
```

The application object has several methods. For instance, a new CST-MWS project can be opened by invoking the *NewMWS* method through the *invoke* function

```
oMWS = invoke(oCST_Studio, 'NewMWS');
```

An existing CST-MWS project can be opened by invoking the *OpenFile* method through the *invoke* function

```
oMWS = oCST_Studio.invoke('OpenFile',< Project name with full path >);
```

The above statement is equivalent to the following one

```
oMWS = invoke(oCST_Studio,'OpenFile',< Project name with full path >);
```

Both ways are presented in this chapter in order to provide more flavor to the reader. The *NewMWS* and *OpenFile* methods provide the interface/project object, i.e. oMWS. Through this interface various methods can be invoked. For instance, the existing project can be saved and closed by invoking the *Save* and *Quit* methods, respectively.

```
invoke(oMWS, 'Save');
invoke(oMWS, 'Quit');
```

The project can be saved with a different name using the *SaveAs* method. For this method an additional boolean flag is required in order to decide whether the results should be saved along with the project or not.

```
invoke(oMWS, 'SaveAs',< Project name with full path >,bool include_Results);
```

An object can be used several times. When it is no longer needed, it is recommended to release the object and all resources used by that object, i.e.

```
release(oMWS);
```

The oMWS object can be used to get some other objects that can be used to perform various operations. For example, a *brick* object can be used to create a waveguide in an existing CST-MWS project. Obviously, all methods of the brick object can be found in the documentation and, then, they can be implemented. However, it is a bit tedious to read the VBA language documentation of CST-MWS each time before implementing a function. Indeed, reading the documentation can be avoided by exploiting the history list feature of CST. Since almost every action performed on CST-MWS is recorded in the history list in the form of VBA language, it can be directly translated to an equivalent MATLAB® code. For example, if a rectangular waveguide having the dimension 5×2.5×10 mm with the name recWg is drawn in component1 in the CST-MWS, then the following code is recorded in the CST-MWS history list

```
With Brick
     .Reset
     .Name "recWg"
     .Component "component1"
     .Xrange "0", "5"
     .Yrange "0", "2.5"
     .Zrange "0", "10"
     .Material "Vacuum"
     .Create
End With.
```

In this script, *Brick* is an object and its various methods have been called. This VBA script can be easily translated in an equivalent MATLAB® code. All the methods of the *Brick* object can be called by using the *invoke* function in MATLAB®, as reported below

```
oBrick = invoke(oMWS, 'Brick');
invoke(oBrick, 'Reset');
invoke(oBrick, 'Name', 'recWg');
invoke(oBrick, 'Component', 'component1');
invoke(oBrick, 'Xrange', '0', '5');
invoke(oBrick, 'Yrange', '0', '2.5');
invoke(oBrick, 'Zrange', '0', '10');
invoke(oBrick, 'Material', 'Vacuum');
invoke(oBrick, 'Create');
```

In this way a rectangular waveguide will be created when the *Create* method is invoked. This is a very nice and easy way to translate the VBA code into an equivalent MATLAB® code without having a basic knowledge of the VBA language.

It is worthwhile to mention here that only those processes that need to be updated when any parameter is changed are recorded in the history list (e.g. the port definition is recorded in the history list because if the geometry varies, then the port definition is updated accordingly). There are some processes that do not need to be registered in the history list, e.g parameter initialization, exporting the design in sat format or exporting the scattering parameter in touchstone format. Therefore, the equivalent code of the above mentioned processes can not be found in the history list. Hence, in order to automate these processes through COM, information about the available objects and their methods must be derived from the CST-MWS documentation in the VBA language section.

The above described procedure is quite straightforward and it works very well. However, if the waveguide dimensions are parametrized, then the waveguide structure will not be updated upon changing the parameter values. The reason is that, using the above procedure, the instructions are registered in the history list and, hence, when the parameter value changes the structure will not be updated accordingly. In order to register the instructions in the history list, CST provides the *AddToHistory* method. This method requires two arguments. The *content* variable containing the instruction that has to be added in the history list and the content header. The content is executed through the VBA interpreter when the *AddToHistory* method is invoked. Therefore, the content variable must contain valid VBA commands for CST MICROWAVE STUDIO. The header of the content should follow the naming convention of CST MICROWAVE STUDIO that can be derived from the history list header. If *content* and *content header* contain valid VBA instructions, then the *AddToHistory* method returns a boolean flag having the true value, otherwise it returns a false flag. In the following example, again a rectangular waveguide having the dimension $a \times b \times c$ mm with name recWg is drawn in component1 in CST-MWS. In this way, a rectangular waveguide is created and instructions are also recorded in the CST-MWS history list.

```
content = sprintf('With Brick');
content = sprintf('%s\n.Reset',content);
```

```
content = sprintf('%s\n.Name "recWg"',content);
content = sprintf('%s\n.Component "component1"',content);
content = sprintf('%s\n.Xrange "0", "a"',content);
content = sprintf('%s\n.Yrange "0", "b"',content);
content = sprintf('%s\n.Zrange "0", "c"',content);
content = sprintf('%s\n.Material "Vacuum"',content);
content = sprintf('%s\n.Create',content);
content = sprintf('%s\n.End With',content);
header = ['define brick: component1:recWg'];
status = invoke(oMWS,'AddToHistory',header,content);
```

In this example, if any of the parameters a, b or c changes, then CST-MWS asks to update the history list by pressing the F7 key. Updating of the history list can also be done through MATLAB® by invoking the *Rebuild* function

```
invoke(oMWS,'Rebuild');
```

From the above discussion, it can be noticed that the user has to know all the parameters and methods of the brick object in order to create it. Since this is a bit cumbersome, the COM-EM-AT developed eliminates this problem. It can be seen from the following listing that the rectangular waveguide example becomes very simple using the COM-EM-AT

```
oCST_Studio = f_OpenCST_StudioSuit();
oMWS    = f_OpenCST_MWS_Project(oCST_Studio,< Project name with full
    path >);
f_StoreDoubleParameter(oMWS,'a',5.0);
f_StoreDoubleParameter(oMWS,'b',2.5);
f_StoreDoubleParameter(oMWS,'c',10.0);
status = f_CreateBrick(oMWS,'component1','recWg','Vacuum',{'0' 'a'},{'0
    ' 'b'},{'0' 'c'});
```

As a matter of fact, thanks to the COM-EM-AT the user doesn't need to worry about VBA language, application objects and their methods.

Lets consider a real world example, i.e. the analysis of the DFS polarizer using the COM-EM-AT. A generic flow chart for the COM-EM-AT is reported in Fig. 4.2. The MATLAB® listing for this flow chart is reported in Listing 4.1. In the flow chart, two types of text color are used. The gray text color indicates processes performed by MATLAB®, whereas the black text color denotes that the process needs MATLAB® along with the EM software. In this example, the first step is to add the COM-EM-AT in the MATLAB® path. Once the variables have been initialized in MATLAB®, the EM tool is opened and a new project is created. A template is chosen in order to get some default settings. It can be seen that the Listing 4.1 exactly follows the 4.2 flow chart.

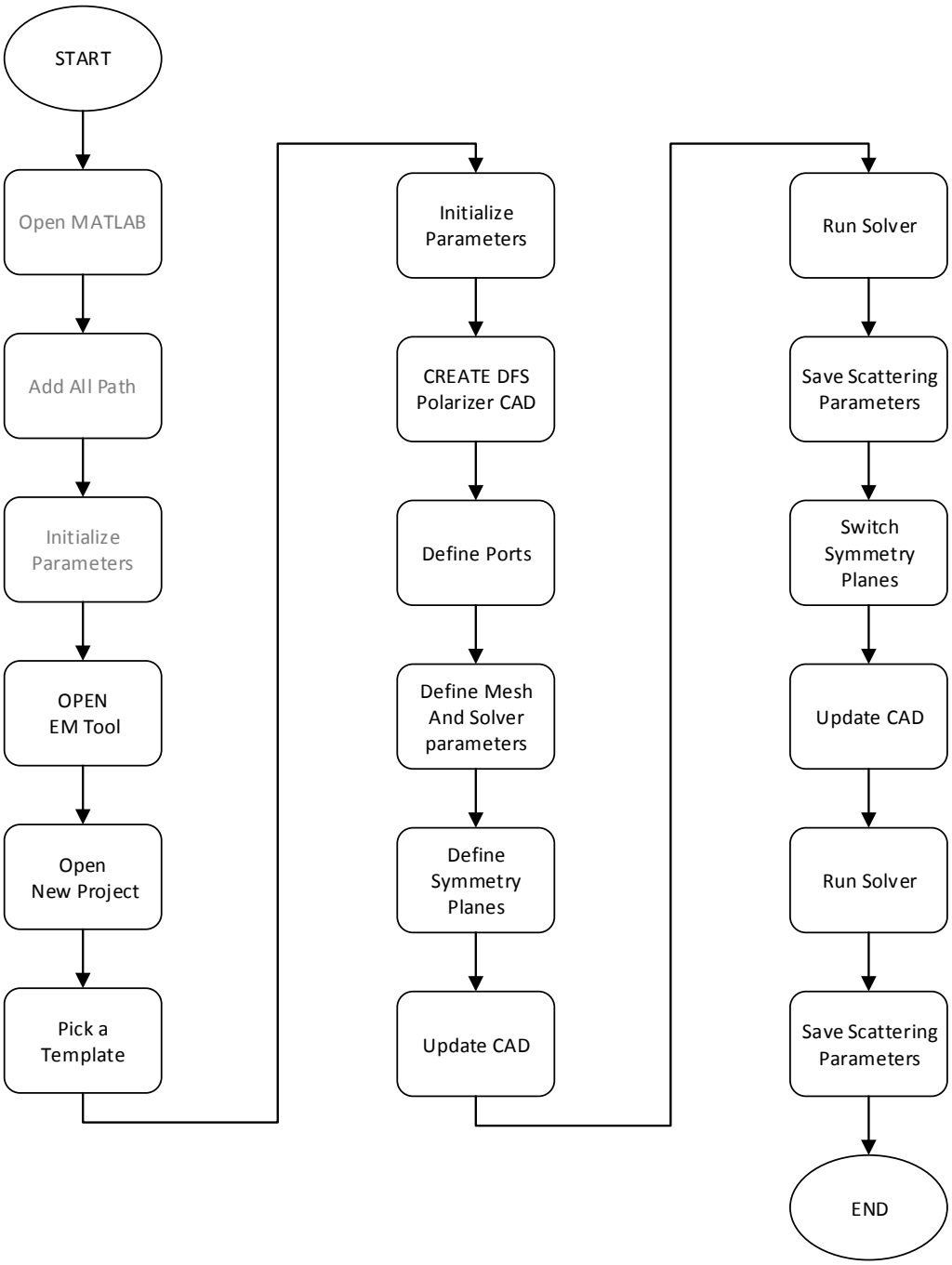

Figure 4.2. Layout of the DFS polarizer analysis using COM-EM-AT. Boxes containing text in gray color refer to operations that need only MATLAB®, whereas boxes containing text in black color refer to processes where MATLAB® and EM software interaction is required.

The parameters are initialized in CST-MWS. Using these parameters the CAD is created in CST-MWS. Finally, all the parts are added together, the relevant edges are blended and the waveguide ports are defined. In order to define the edge blending and the waveguide ports, the user must know their edge ID and the face number. However, it is difficult to know the edge ID or face number a priori. This problem can be overcome by observing the history list of CST-MWS, i.e. first select a particular edge in CST-MWS, see its corresponding ID from the history list and, then, copy this ID in the MATLAB® listing. This procedure has to be repeated for all edges for which blending is required. The same approach is followed for the port face number variable, i.e. *port1FaceNum* and *port2FaceNum*. Once the CAD and the input ports have been defined, also the mesh and the solver setting can be defined. Since the structure of the polarizer under consideration has two-fold symmetry, this property can be exploited in order to reduce the simulation time. Indeed, there is no need to simulate the full structure but only a quarter of it is sufficient by defining suitable symmetry planes. After updating the CAD and running the solver, MATLAB® will fetch the results from CST-MWS and, then, switch the symmetry plane in order to obtain the scattering parameters for the other polarization. The CAD is again updated and the solver is started. When the solver finishes its job, MATLAB® will fetch the results again from CST-MWS and all the variables will be saved in the MAT format on hard drive. Finally, MATLAB® will save the project and close it. During all this process when MATLAB® sends some request to EM tool, it will remain busy until and unless it will not have received the acknowledgment from the EM tool. Therefore, when the EM software solver runs MATLAB® will remain busy and no other operation can be performed during this time slot.

```
%-- Add path
addpath(genpath(< COM-EM-AT full path >));

%-- Initialize parameters
R = 1.31;
wInd = [1 1 1];                          % Width of the inductive
    arm
hInd = [0.6420    0.6320    0.6420]; % Height of the inductive
    arm
wCap = [1.238     1.425     1.238];  % Width of the capacitive
    arm
hCap = [0.1000    0.1220    0.1000]; % Height of the capacitive
    arm
lStub          = 3;          % Length of the DFS
lCav           = 3;          % Length of the circular cavity
lInput         = 5;          % Input circular waveguide length
lOutput        = 5;          % Output circular waveguide length
blendRad       = 0.2;        % Edge blend Radius
```

```
15 numModesIn      = 3;          % Number of modes on the input
       ports
16 numModesOut     = 3;          % Number of modes on the output
       ports
17 NfreqAnal       = 50;         % Number of analysis frequency point
18 NfreqAdapt      = 3;          % Number of adaptive frequency point
19 fMin            = 75;
20 fMax            = 110;
21 VfreqSpecAnal   = [75 110];  % Analysis frequency range
22 VfreqSpecAdapt = [104 104]; % Adaptive frequency range

24 %-- Open CST-MWS
25 oCST_Studio = f_OpenCST_StudioSuit();

27 %-- Open New MWS Project
28 oMWS         = f_CreateCST_MWS_Project(oCST_Studio);

30 %-- Select a template
31 f_CreateMWS_Template(oMWS, 'Coupler (Waveguide)^+MWS');

33 %-- Initialize parameters
34 f_StoreParameter(oMWS, 'R',R);
35 f_StoreParameter(oMWS, 'wInd_1',wInd(1));
36 f_StoreParameter(oMWS, 'wInd_2',wInd(2));
37 f_StoreParameter(oMWS, 'wInd_3',wInd(3));
38 f_StoreParameter(oMWS, 'hInd_1',hInd(1));
39 f_StoreParameter(oMWS, 'hInd_2',hInd(2));
40 f_StoreParameter(oMWS, 'hInd_3',hInd(3));
41 f_StoreParameter(oMWS, 'wCap_1',wCap(1));
42 f_StoreParameter(oMWS, 'wCap_2',wCap(2));
43 f_StoreParameter(oMWS, 'wCap_3',wCap(3));
44 f_StoreParameter(oMWS, 'hCap_1',hCap(1));
45 f_StoreParameter(oMWS, 'hCap_2',hCap(2));
46 f_StoreParameter(oMWS, 'hCap_3',hCap(3));
47 f_StoreParameter(oMWS, 'lStub',lStub);
48 f_StoreParameter(oMWS, 'lCav',lCav);
49 f_StoreParameter(oMWS, 'lInput',lInput);
50 f_StoreParameter(oMWS, 'lOutput',lOutput);
51 f_StoreParameter(oMWS, 'blendRad',blendRad);
52 f_StoreParameter(oMWS, 'fMin',fMin);
53 f_StoreParameter(oMWS, 'fMax',fMax);
54 f_StoreParameter(oMWS, 'numModesIn',numModesIn);
55 f_StoreParameter(oMWS, 'numModesOut',numModesOut);
56 f_StoreParameter(oMWS, 'NfreqAnal',NfreqAnal);
57 f_StoreParameter(oMWS, 'NfreqAdapt',NfreqAdapt);
58 componentName = 'Polarizer';
59 partName      = 'innerPart';

61 %-- Create DFS polarizer geometry
```

```
63 %-- Create a new component
64 f_CreateComponent(oMWS, componentName);
65 f_ActivateWCS(oMWS, 'global');
66 %-- Create the circular waveguide ( Input waveguide)
67 f_CreateCylinder(oMWS, componentName, 'inCircWg', 'Vacuum', 'z', 'R'
       ,0,0,0,0,{'0' 'lInput'},0);

69 %-- Stub 1
70 %-- Create the circular waveguide
71 f_CreateCylinder(oMWS, componentName, 'stub01', 'Vacuum', 'z', 'R'
       ,0,0,0,0,{'lInput' 'lInput+lStub'},0);
72 %-- Create the Inductive arm
73 f_CreateBrick(oMWS, componentName, 'part01', 'Vacuum',{'-wInd_1/2'
       'wInd_1/2'},{'-(R+hInd_1)' '(R+hInd_1)'},{'lInput' 'lInput+
       lStub'});
74 %-- Create the Capacitive arm
75 f_CreateBrick(oMWS, componentName, 'part02', 'Vacuum',{'-(R+hCap_1)
       ' '(R+hCap_1)'},{'-wCap_1/2' 'wCap_1/2'},{'lInput' 'lInput+
       lStub'});
76 %-- Add all parts together
77 f_AddSolids(oMWS, componentName, 'stub01', componentName, 'part01');
78 f_AddSolids(oMWS, componentName, 'stub01', componentName, 'part02');
79 %-- Create the circular waveguide ( Cavity 1 )
80 f_CreateCylinder(oMWS, componentName, 'cavityWg1', 'Vacuum', 'z', 'R'
       ,0,0,0,0,{'lInput+lStub' 'lInput+lStub+lCav'},0);

82 %-- Stub 2
83 %-- Create the circular waveguide
84 f_CreateCylinder(oMWS, componentName, 'stub02', 'Vacuum', 'z', 'R'
       ,0,0,0,0,{'lInput+lStub+lCav' 'lInput+lStub+lCav+lStub'},0);
85 %-- Create the Inductive arm
86 f_CreateBrick(oMWS, componentName, 'part01', 'Vacuum',{'-wInd_2/2'
       'wInd_2/2'},{'-(R+hInd_2)' '(R+hInd_2)'},{'lInput+lStub+lCav'
       'lInput+lStub+lCav+lStub'});
87 %-- Create the Capacitive arm
88 f_CreateBrick(oMWS, componentName, 'part02', 'Vacuum',{'-(R+hCap_2)
       ' '(R+hCap_2)'},{'-wCap_2/2' 'wCap_2/2'},{'lInput+lStub+lCav'
       'lInput+lStub+lCav+lStub'});
89 %-- Add all parts together
90 f_AddSolids(oMWS, componentName, 'stub02', componentName, 'part01');
91 f_AddSolids(oMWS, componentName, 'stub02', componentName, 'part02');
92 %-- Create the circular waveguide ( Cavity 2 )
93 f_CreateCylinder(oMWS, componentName, 'cavityWg2', 'Vacuum', 'z', 'R'
       ,0,0,0,0,{'lInput+lStub+lCav+lStub' 'lInput+lStub+lCav+lStub+
       lCav'},0);

95 %-- Stub 3
96 %-- Create the circular waveguide
```

```
97  f_CreateCylinder(oMWS,componentName,'stub03','Vacuum','z','R'
        ,0,0,0,0,{'lInput+lStub+lCav+lStub+lCav' 'lInput+lStub+lCav+
        lStub+lCav+lStub'},0);
98  %-- Create the Inductive arm
99  f_CreateBrick(oMWS,componentName,'part01','Vacuum',{'-wInd_3/2'
        'wInd_3/2'},{'-(R+hInd_3)' '(R+hInd_3)'},{'lInput+lStub+lCav+
        lStub+lCav' 'lInput+lStub+lCav+lStub+lCav+lStub'});
100 %-- Create the Capacitive arm
101 f_CreateBrick(oMWS,componentName,'part02','Vacuum',{'-(R+hCap_3)
        ' '(R+hCap_3)'},{'-wCap_3/2' 'wCap_3/2'},{'lInput+lStub+lCav+
        lStub+lCav' 'lInput+lStub+lCav+lStub+lCav+lStub'});
102 %-- Add all parts together
103 f_AddSolids(oMWS,componentName,'stub03',componentName,'part01');
104 f_AddSolids(oMWS,componentName,'stub03',componentName,'part02');
105 %-- Create the circular waveguide ( output waveguide )
106 f_CreateCylinder(oMWS,componentName,'outWg','Vacuum','z','R'
        ,0,0,0,0,{'lInput+2*lCav+3*lStub' 'lInput+2*lCav+3*lStub+
        lOutput'},0);

108 f_RenameComponentPart(oMWS,componentName,'inCircWg',partName);

110 %-- Add All parts togather
111 f_AddSolids(oMWS,componentName,partName,componentName,'stub01');
112 f_AddSolids(oMWS,componentName,partName,componentName,'cavityWg1
        ');
113 f_AddSolids(oMWS,componentName,partName,componentName,'stub02');
114 f_AddSolids(oMWS,componentName,partName,componentName,'cavityWg2
        ');
115 f_AddSolids(oMWS,componentName,partName,componentName,'stub03');
116 f_AddSolids(oMWS,componentName,partName,componentName,'outWg');

118 %-- Blend Edge
119 blendEdgeID = [ ...
120       12 3
121       14 4
122       26 12
123       24 11
124       11 6
125       13 5
126       23 14
127       25 13
128       61 40
129       63 39
130       75 47
131       76 46
132       62 37
133       64 38
134       73 48
135       74 45
136       112 71
```

```
137         114  72
138         124  79
139         126  80
140         111  74
141         113  73
142         123  82
143         125  81
144         ];
145 for idInd = 1:size(blendEdgeID,1);
146         f_PickEdgeFromId(oMWS, componentName, partName, blendEdgeID(
                idInd,1), blendEdgeID(idInd,2));
147 end
148 f_BlendEdge(oMWS, componentName, partName, blendRad);

150 %-- Define port 1
151 port1FaceNum = 88;
152 f_PickFaceFromId(oMWS, componentName, 'innerPart', port1FaceNum);
153 oPort.portNumber     = 1;
154 oPort.numberOfModes = numModesIn;
155 oPort.coordinates    = 'Picks';
156 oPort.orientation    = 'positive';
157 f_CreatePort(oMWS, oPort);
158 f_ClearAllPicks(oMWS);

160 %-- Define port 2
161 port2FaceNum = 3;
162 f_PickFaceFromId(oMWS, componentName, 'innerPart', port2FaceNum);
163 oPort.portNumber     = 2;
164 oPort.numberOfModes = numModesOut;
165 oPort.coordinates    = 'Picks';
166 oPort.orientation    = 'positive';
167 f_CreatePort(oMWS, oPort);
168 f_ClearAllPicks(oMWS);

170 %-- Frequency range
171 oSolver.frequencyRange = [fMin fMax];
172 f_CreateSolver(oMWS, oSolver);

174 %-- Mesh parameters
175 oMesh.meshType                    = 'Tetrahedral';
176 oMesh.PBAType                     = 'PBA';
177 oMesh.stepsPerWavelengthTet       = 15;
178 oMesh.minimumStepNumberTet        = 15;
179 oMesh.curvatureRefinementFactor   = 0.04;
180 oMesh.minimumCurvatureRefinement = 300;
181 oMesh.curvatureOrder              = 3;
182 f_CreateMesh(oMWS, oMesh);

184 %-- Mesh adaptation 3D
185 oMeshAdaption3D.setType          = 'HighFrequencyTet';
```

```
186 oMeshAdaption3D.minPasses        = 3;
187 oMeshAdaption3D.maxPasses        = 6;
188 oMeshAdaption3D.maxDeltaS        = 1e-14;
189 oMeshAdaption3D.meshIncrement    = 6;
190 f_CreateMeshAdaption3D(oMWS, oMeshAdaption3D);

192 %-- Solver parameters
193 oFD_Solver.orderTet             = 'Second';
194 oFD_Solver.bSParameterSweep     = 'False';
195 oFD_Solver.accuracyTet          = 1e-6;
196 oFD_Solver.stimulation          = {'List' 'List'};
197 oFD_Solver.stimulationList      = {'p1','1'};
198 oFD_Solver.addSampleInterval = {VfreqSpecAnal NfreqAnal '
        Equidistant' 'False';
199      VfreqSpecAdapt NfreqAdapt 'Equidistant' 'True'};
200 f_CreateFD_Solver(oMWS, oFD_Solver);

202 %-- Symmetry Planes
203 f_SetSymmetryPlane(oMWS,'magnetic','electric','none');  % X-Symm
        Plane: magnetic, Y-Symm Plane: electric, Z-Symm Plane: none

205 %-- Update CAD
206 f_UpdateModel(oMWS);

208 %-- Run Solver
209 f_StartFD_Solver(oMWS);

211 %-- Save results
212 [scatMatV_Pol, freq] = f_SaveScatMatTouchStone(oMWS);

214 %-- Switch Symmetry Planes
215 f_SetSymmetryPlane(oMWS,'electric','magnetic','none');  % X-Symm
        Plane: electric, Y-Symm Plane:magnetic , Z-Symm Plane: none

217 %-- Update CAD
218 f_UpdateModel(oMWS);

220 %-- Run Solvr
221 f_StartFD_Solver(oMWS);

223 %-- Save results
224 [scatMatH_Pol, freq] = f_SaveScatMatTouchStone(oMWS);

226 %-- Save all resutls in MAT format
227 save DFSPolarizerResults

229 %-- Save CST Project
230 f_SaveAsCST_MWS_Project(oMWS,< Project name with full path >);

232 %-- Close CST-MWS
```

```
233  f_CloseCST_MWS_Project(oMWS);
```

Listing 4.1. DFS polarizer analysis using the COM-EM-AT for CST-MWS.

4.3.2 COM Automation for HFSS

The EM software Ansys HFSS (HFSS) also provides the COM support. Its application ID is *AnsoftHfss.HfssScriptInterface*. Using its ID the application object can be obtained in the following way

```
oAnsoftApp = actxserver('AnsoftHfss.HfssScriptInterface');
```

The application object has several methods. For instance, the Desktop object can be obtained from the application object and, then, through the Desktop object a new HFSS project can be opened by invoking the *GetAppDesktop* method

```
oDesktop    = oAnsoftApp.GetAppDesktop();
invoke(oDesktop, 'NewProject');
```

The project initialization in HFSS is slightly different than that in CST-MWS. In HFSS, first, it is required to insert the *HFSSDesign* that provides the *Project* object. The *project* object is provided by the *Design* object by setting the current design as an active design. Then, the *Design* object provides the *Editor* object by setting the active editor as 3D modeler. These three objects are essential objects, since they provide several useful methods. They can be obtained in the following way through COM interface.

```
oProject    = oDesktop.GetActiveProject();
oProject.InsertDesign( 'HFSS', 'HFSSDesign1', 'DrivenModal', '');
oDesign = oProject.SetActiveDesign('HFSSDesign1');
oEditor = oDesign.SetActiveEditor('3D Modeler');
```

HFSS also uses the VBA script on the back end. In order to develop a COM automation, one way could be to study the documentation and, then, to develop the required functions. This is an interesting approach, but it requires a basic knowledge of the VBA language. The other way, that is similar to the one adopted in the previous section, is based on recording of the VBA script. HFSS provides this feature that allows the user to record[3] his action in the form of a VBA script that can be subsequently used as a macro. This approach becomes more attractive when the recorded script is converted to an equivalent MATLAB® script. This code transformation is straightforward, since no VBA expertise are required. As an example, lets consider again the rectangular waveguide example. In order ot draw a rectangular waveguide in HFSS, the following script can be recorded

[3]this option can be accessed from: Tool → Record Script To File.

```
oEditor.CreateBox Array("NAME:BoxParameters", "XPosition:=", "0mm", "
    YPosition:=","0mm", "ZPosition:=", "0mm", "XSize:=", "5.0mm", "
    YSize:=", "2.5mm", "ZSize:=","10.0mm"), Array("NAME:Attributes", "
    Name:=", "recWg", "Flags:=", "", "Color:=","(132 132 193)", "
    Transparency:=", 0, "PartCoordinateSystem:=", "Global", "UDMId:=","
    ", "MaterialValue:=", "" & Chr(34) & "vacuum" & Chr(34) & "", "
    SolveInside:=",true)
```

It is clear from the above VBA script that the *Editor* object is using its *CreateBox* method. The Editor[4] object would call the *CreateBox* method through the invoke function in the equivalent MATLAB®. Another conversion is still required in the above script to replace all the *Array()* keywords along with its parentheses with braces. Finally, the equivalent MATLAB® script for the above VBA code could be as

```
invoke(oEditor,'CreateBox',{'NAME:BoxParameters', 'XPosition:=', '0mm',
    'YPosition:=','0mm', 'ZPosition:=', '0mm', 'XSize:=', '5.0mm', '
    YSize:=', '2.5mm', 'ZSize:=','10.0mm'}, {'NAME:Attributes', 'Name:=
    ', 'recWg', 'Flags:=', '', 'Color:=','(132 132 193)', 'Transparency
    :=', 0, 'PartCoordinateSystem:=', 'Global', 'UDMId:=','', '
    MaterialValue:=', '' & Chr(34) & 'vacuum' & Chr(34) & '', '
    SolveInside:=',true});
```

The above script can be run in MATLAB® in order to create a rectangular waveguide having the dimension 5×2.5×10 mm. Surely, this function can be parametrized in order to make it more general.

A similar approach can be used for the other functions by recording the VBA script in a file and creating the MATLAB® equivalent code. The COM-EM-AT developed for HFSS is quite general and user-friendly, since all the implementation details are defined inside the 38 functions that have been created. The DFS polarizer has also been analyzed using the COM-EM-AT for HFSS. The flow of the program is exactly the same as the one reported in the Listing 4.2. In order to avoid the duplication of the work, the HFSS example for the COM-EM-AT is not reported here.

4.3.3 COM Automation for Parametric Analysis

The possibility of performing a full parametric analysis through the COM-EM-AT is a very powerful feature, since it allows the RF designer to easily perform a manual pre-optimization of the structure. The parametric analysis feature is generic and it can be used for any type of problem. For instance, the main script of the parametric analysis of the COM-EM-AT contains only two lines as reported below

[4]It is assumed that the oEditor object has already been created as mentioned in the above paragraph.

inputConfiguration
PerformParameterSweepMultiPort

The parametric analysis feature is currently available only for CST-MWS, but it can be extended for HFSS with some minimal changes. The prerequisite of the parametric analysis feature of the COM-EM-AT is an existing design project and the corresponding configuration file. The user needs to configure only the input configuration file. An example of the input configuration file is reported in Listing 4.2

```
addpath(genpath( < COM Automation Tool Path > ))
cstProjectPath = '< CST Project Path >';
cstProjectName = '< CST Project Name >';
deviceName = '<Device Name>';
%-- Grid Defination
parameterName = {'A','B','C'};
parameterRange = [...
    5.0 2.4 09 % Min. value
    5.5 2.6 11 % Max. value
    03  03  03 % Number of points
    ];
simulationPort = [1]; % Simulation Port Number e.g. [ 2 5 7] or [1:9]
   or [1:4 7 9]
%-- Flag Settings
activateGridAnalysis = 0;     % Analysis type.
                              % 0-Grid Analysis 1-User defined points
saveScatMatInTouchStone = 1; % Save Scat Mat in Touch Stone Format
                              % 0-No, 1-Yes
saveEfficiency      = 1; % Save Efficiency results
                         % 0-No, 1-Yes
saveScatMatInPolar = 1; % Save Scat Mat in Polar Form
                         % 0-No, 1-Yes
saveFarFieldsData  = 1; % Save Farfield Data
                         % 0-No, 1-Yes
saveCST_Parameter  = 1; % Save all CST Parameter
                         % 0-No, 1-Yes
putParamNameInDir  = 0; % Directory name
                         % 0-Selected parameters, 1-All parameters
solverType          = 'TD-Solver'; % 'TD-Solver', 'FD-Solver'
```

Listing 4.2. Configuration file for parametric analysis.

According to this input configuration file a parent directory, whose name is defined in the variable *deviceName*, is created and all the data is saved inside this directory. Hereafter, this directory is referred as parent directory and A, B and C denote three parameters that are necessary in the CST-MWS project. The span of each parameter is defined in the *parameterRange* variable. For example, the interval for the parameter A is [5 5.5] spanned with 3 samples. According to this configuration file, since there are three parameters and each parameter has 3 samples, a 3-dimensional

grid is created and 9 analysis are performed. The results of each analysis results are saved in a separate directory that is referred to as parameter directory. The name of the parameter directory contains either the parameter name along with its value or the parameter name that is defined in the CST-MWS project. This option can be choosen from the *putParamNameInDir* flag. The description of each variable and each flag used in the configuration file are given below.

cstProjectPath This variable contains the existing CST-MWS project path.

cstProjectName This variable contains the existing CST-MWS project name.

deviceName This variable contains the Parent directory name. All the data is saved inside this directory that is the top level directory for the parametric analysis.

parameterName This variable contains the parameter list. The name of the parameter should be exactly the same as the one defined in the existing CST-MWS project.

parameterRange This variable contains the grid point definition upon which the analysis is performed. For instance according to the listing 4.2 the parameter A varies from 5 to 5.5 and 3 samples are defined in this interval using the *linspace* function. If the user wants to perform the analysis on a particular set of values, instead of considering all the grid points, he can also pass those valuein this variable, e.g. parameterRange = [5.0 2.4 09]. In this case the *activateGridAnalysis* flag has to be set to 1.

simulationPort This variable contains the ports that are excited during the analysis, e.g. simulationPort = [2 5 7] or simulationPort = [1:9] or simulationPort = [1:4 7 9].

activateGridAnalysis This flag is set to zero when the parameterRange variable is defined as a grid, i.e parameterRange contains the minimum, maximum and the number of samples for this interval. This flag is set to one when the user wants to perform the analysis only on some particular points.

saveScatMatInTouchStone This flag is used to decide whether the scattering parameter should be exported in touch stone format or not. If this flag is set to one, the scattering parameters are exported to the parameter directory. If this flag is set to zero, the scattering parameters are not exported.

saveEfficiency This flag is used to decide whether the efficiency should be save or not. If this flag is set to one, two directories named 'linear' and 'db' are created inside the parameter directory and the radiation and total efficiency are saved in linear and in db format inside the receptive directories.

saveScatMatInPolar This flag is used to decide whether the scattering matrix in polar format should be saved or not. If this flag is set to one, the scattering matrix in polar format is saved inside the parameter directory.

saveFarFieldsData This flag is used to decide whether the farfield data should be saved or not. If this flag is set to one, all the defined farfield monitor data are exported to the parameter directory and the value of the frequency is added in the file name.

saveCST_Parameter If this flag is set to one, all the parameters defined in the CST-MWS project are exported to the parameter directory in dat format.

putParamNameInDir This flag is used to decide whether the parameter directory name contains all the parameter name defined in the CST-MWS project or the parameter name defined in the parameterName variable.

solverType This flag is used to decide which solver is used during the analysis. i.e. 'TD-Solver' or 'FD-Solver'.

4.3.4 COM Automation for Optimization

Optimization of RF components can be performed using both CST-MWS and HFSS, but there are very few optimization algorithms available in these EM softwares. This aspect can be a bottleneck in a specific design activity. The problem becomes more stringent when users want to exploit their own optimization algorithms or to use some particular optimization algorithm that is available in MATLAB®. In these cases, the COM-EM-AT provides the required flexibility. Indeed, using the COM-EM-AT any MATLAB® optimization or any user defined algorithm can be exploited with the EM software. A generic flow chart is reported in Listing 4.3. In this flow chart the text having the gray color refers to a process that only runs on MATLAB®, whereas the text having black color refers to a process in which interaction among MATLAB® and EM software occurs.

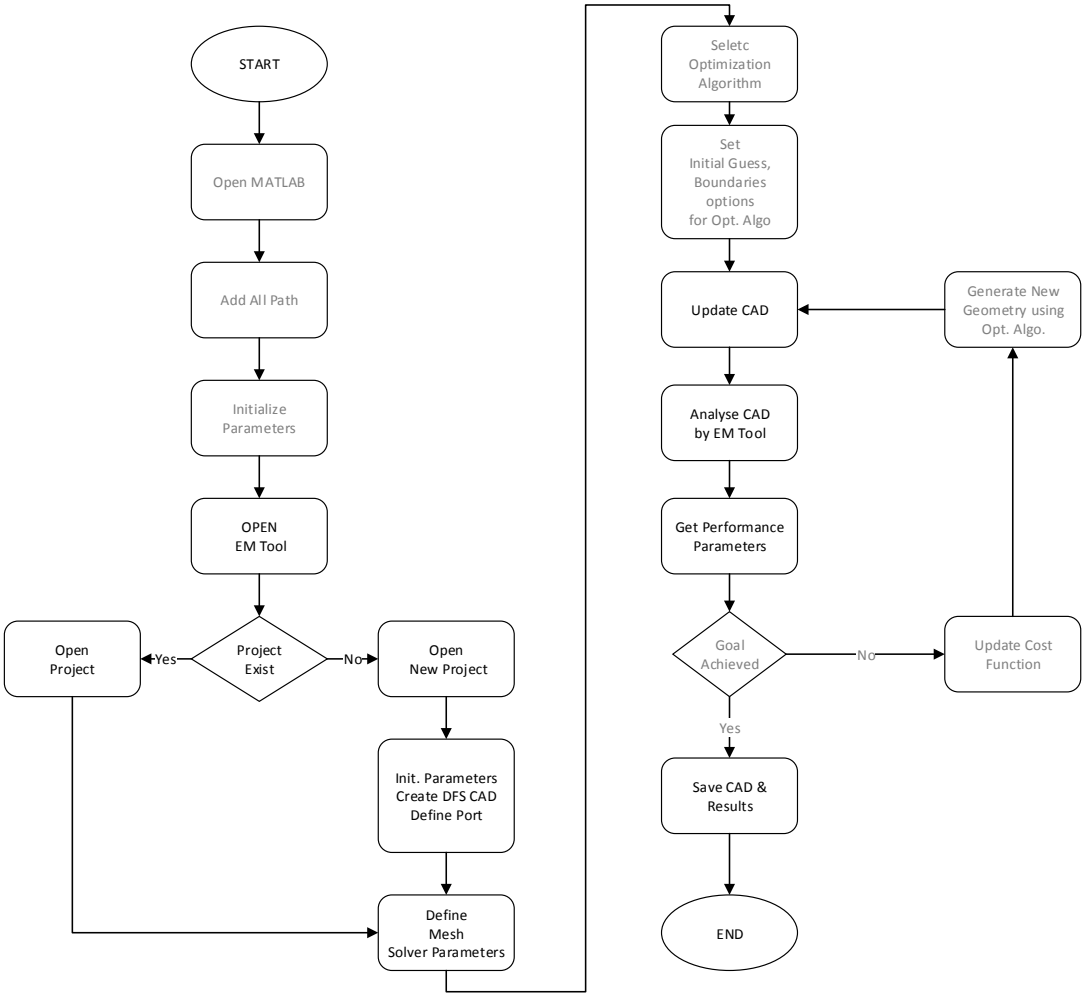

Figure 4.3. A generic optimization layout using the COM-EM-AT. Boxes containing text in gray color refer to operations that need only MATLAB®, whereas boxes containing text in black color refer to processes where MATLAB® and EM software interaction is required.

4.3.5 COM Automation for Post Processing

The COM-EM-AT is also very useful for post processing. For instance, if the E-field or H-field at some particular cross section (e.g. the longitudinal cut of the DFS polarizer shown in Fig. 4.4) or at some face for various frequency points is required, it is very tedious each time to set the cross section, to export the data and to save it with some particular file name. On the contrary, these step becomes very simple when using the COM-EM-AT. A simple example is shown in Listing 4.3, where the cutting plane is set by points.

```
addpath(genpath( < COM Automation Tool Path > ));

%-- Open CST Studio Suit
oCST_Studio = f_OpenCST_StudioSuit();

%-- Open CST MWS Project
oMWS = f_OpenCST_MWS_Project(oCST_Studio,< Project name with full path
    >);

%-- Set Cut Plane by Point
oPlot.definePlane.nx = 1;
oPlot.definePlane.ny = 0;
oPlot.definePlane.nz = 0;
oPlot.definePlane.px = 0;
oPlot.definePlane.py = 0;
oPlot.definePlane.pz = 0;
oPlot.bShowCutplane  = true;
f_SetCutPlane(oMWS, oPlot);

% Get H_FieldData and also export data using Cutting plane
oH_Field.exportFilePathWithName = [pwd '\H_Field_Results'];
oH_Field.bPlot3DPlotsOn2DPlane  = true; % Set cut place before getting
    the H_FieldData
H_FieldData = f_GetH_Fields(oMWS, oH_Field)
```

Listing 4.3. Exporting the H-field at a particular cross section defined by points.

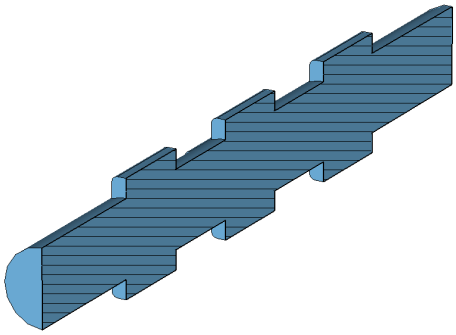

Figure 4.4. DFS polarizer cross section. The H-field is exported on this cross section.

4.4 Conclusion

In this chapter the COM-EM-AT developed during the doctoral program has been is introduced. This tool provides several benefits, among which are more control to the user over the EM software, a flexible way for performing parametric analysis and possibility of using the EM software in conjunction with any optimization algorithm. The COM-EM-AT also provides a high degree of flexibility in data processing, especially when a large number of field monitors and data have to be exported. From the practical point of view, an interesting aspect is that the developed COM-EM-AT does not require any basic knowledge of VBA to the user. Moreover, any MATLAB® user can easily exploit all its functionalities. The broadband turnstile junction reported in chapter 3 and having 40 % bandwidth centered at 40 GHz has been designed using the COM-EM-AT, thus proving the effectiveness of the tool.

Chapter 5

Distributed Computing Using MATLAB® for In-House Developed Analysis Tool

5.1 Introduction

Computational power and memory resources are key aspects in EM modeling. As an example, surfaces of 3D metallic structure can be discretized by means of many flat triangular or quadrilateral elements,on which a set of local basis functions are defined for each element, e.g. RWG for triangular domains. The basis function could be first, second or mixed order. When the dimension of the structure is electrically large then a very high number of elements and unknowns are required to properly model the structure. This drives the requirement of higher computational power and memory. Computational power can be increased in various ways. For instance, exploitation of multi core processor is one simple solution among others.

The multi processing can be exploited by Open Multi-Processing (OpenMP) that is a portable standard for shared memory multiprocessing. OpenMP Application Program Interface (API) consists of compiler directives that control the flow of the program. If the directives are defined then it will exploit the multiprocessing and if it is not defined the program will still generate the correct output but it will not exploit the available parallelism. OpenMP does not require a significant effort to parallelize an existing code. It requires only to place some compiler directives around the computationally intensive part of the code[1]. OpenMP is effectively employed in order to accelerate the various numerical method in EM domain. For example, Finite-Element Method (FEM), Finite-Difference Time-Domain

[1] i.e. computationally intensive loops.

Method (FDTD) and Time-Domain Finite-Element Method (TDFEM) parallelized through OpenMP can be found in [47], [48] and [49] respectively. In[50], computational time of NURBS-HOMM[2] is reduced, through OpenMP by computing the impedance matrix in parallel. OpenMP employment is very easy, although essential synchronization can also be easily overlooked. OpenMP directives can be put into C/C++ or FORTRAN programs.

The computation power can also be increased by splitting the problem in small chunks and, then, distributing these small chucks of problem over the network using Open Message Passing Interface (OpenMPI). OpenMPI standard is a message-passing specification between computers and provides very high efficiency. OpenMPI scripts are easily scalable and manageable. However,its employment is quite puzzling because workload distribution has to be managed manually. Therefore, enough expertise are required in order to achieve an adequate speed up factor. Even if OpenMPI is easier to understand, its coding is complex to read, write and maintain. A comparison among OpenMP and OpenMPI performance for FEM and FDTD are reported in [51, 52].

The exploitation of OpenMP along with OpenMPI could be an optimal solution for very huge structures. Although this hybrid approach requires much more efforts, the advantage of shared and distribute memory can be exploited simultaneously[52, 53].

The computationally intensive problems can also be accelerated by using GPU through Compute Unified Device Architecture (Nvidia) (CUDA), Open Graphics Library (OpenGL) or Open Computing Language (OpenCL) APIs. This approach provides massive data-parallel computation even by exploiting off the shelf, general purpose GPU[54] and, then, it is also beneficial from the economical point of view. The only limitation in this case is the GPU memory. For huge problems, a frequent data transfer among the Central Processing Unit (CPU) and GPU happens and the GPU performance degrades[55] as the size of the structure increases. Instead of using one GPU, it is also a good choice to exploit a cluster of GPU. This approach provides significant improvement in the performance as it can be seen in [56] where a speed up factor 71.9 is obtained by using a cluster of GPU for Discontinuous Galerkin FEM (DG-FEM).

The above discussion provides an overview about the different ways for speedup the simulations. If the in-house analysis tool is developed in MATLAB®, then the above stated option can not be exploited because their APIs are available only in C/C++. However MATLAB® provides PCT in order to exploit the CUDA GPU resources without learning the intricacies of GPU architectures. When this option is exhausted due to the larger dimensions of the matrices, the latter can be split in small chunks and, then, transferred from CPU to GPU. However, the overhead

[2]NURBS-HOMM: Non-Uniform Rational B-Splines model with Higher Order Moment Method.

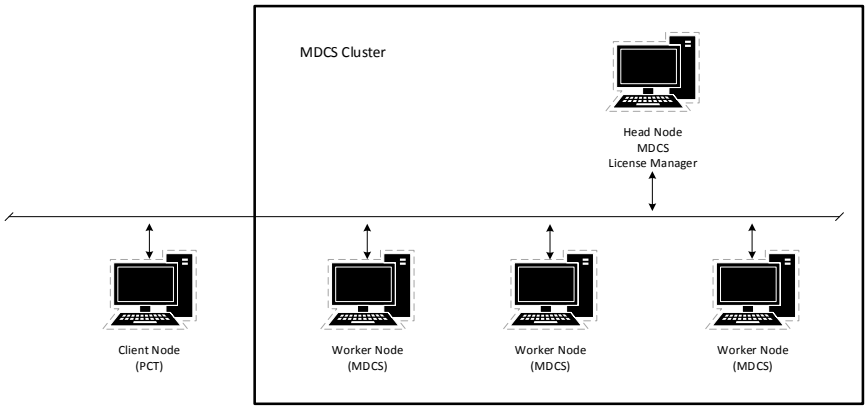

Figure 5.1. A generic MATLAB® Distributed Computing layout.

of frequent data transfer among CPU and GPU degrades the overall performance, specially when the mathematical operation is not so intensive. Therefore, for the present scenario the best choice is MATLAB® Distributed Computing and it can be accomplished by exploiting two MATLAB® toolboxes i.e. MDCST and PCT. In the following section MATLAB® DC configuration and implementation is discussed in detail.

5.2 MATLAB® DC

A generic MATLAB® Distributed Computing Server (MDCS) cluster's outline is reported in Fig. 5.1. It can be seen that the MDCS cluster consists of a head node and several worker nodes. MATLAB® license manager is installed on the head node. The job manager/scheduler is also installed on the head node. The client node is the user-end where user defines its job and submits it to the job manager. Then, the job manager receives the job from the client node and distributes it among the worker nodes. Each worker node performs its job independently from the other worker nodes and submits back the results to the head node. The job manager collects all the distributed task from the worker nodes and, finally, the client node gets the results from the job manager. Since the job manager is running on the head node, the head node should have enough capability to handle the request from the client node as well as from the worker nodes. In MATLAB® documentation it is recommended that the number of worker nodes on each CPU should be equal to the number of cores. For instance, four worker nodes is sufficient for a quad core processor.

In this discussion, MATLAB® default job manager is considered, which is provided with MDCST. It is quite simple and easy to configure for small to medium

size cluster. However, PCT and MDCS also support the following third-party job managers

- Platform LSF
- Microsoft Windows Compute Cluster Server 2003 and Windows HPC Server 2008
- PBS Pro and TORQUE
- mpiexec

The PCT has to be installed on the client node, whereas the MDCST has to be installed on the head and worker nodes as it is depicted in Fig. 5.2. Since we are using the MATLAB® default job manager, it is necessary to install and run the mdce service on each worker and head node. The firewall should be configured accordingly on each machine and the TCP/IP port[3] should be open in order to allow the communication among nodes.

[3]default TCP/IP ports number for a particular MATLAB® version can be seen from MATLAB® documentation

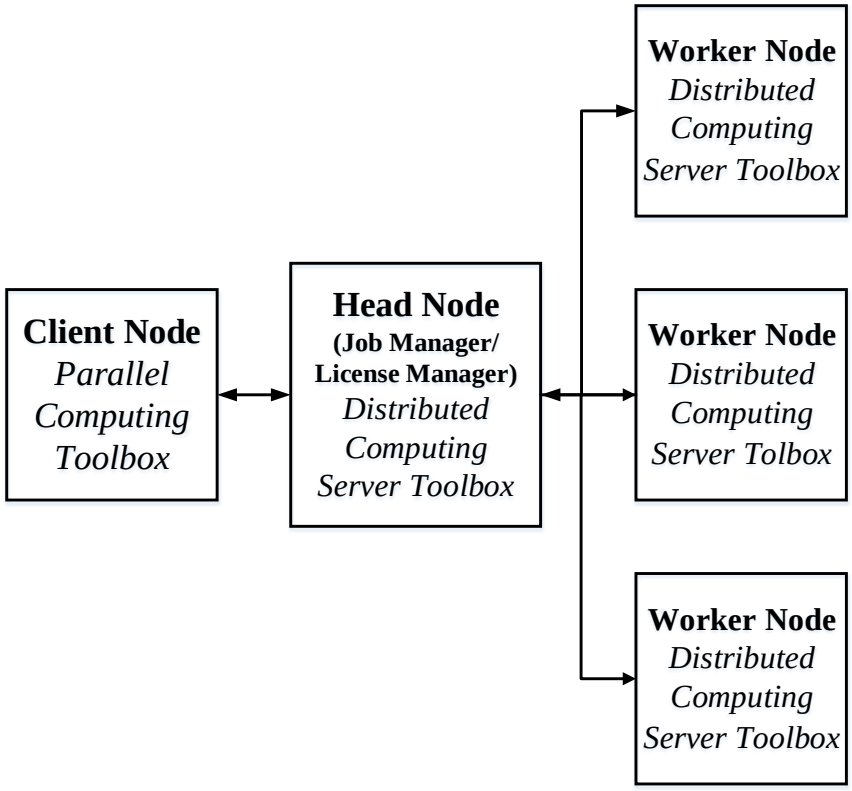

Figure 5.2. MATLAB® toolboxes installation scheme for Distributed Computing. Parallel Computing Toolbox (PCT) is installed on the client node. The license manager is installed on head node, whereas MATLAB® Distributed Computing Server Toolbox (MDCST) is installed on the head and worker nodes.

5.3 In-House Tool Parallelization

PCT along with MDCST provides a variety of solutions in order to accelerate computationally intensive analysis tools. The detail can be seen on the respective toolbox documentation. In this section only those options that can be exploited easily and effectively from the EM perspective are discussed. In order to exploit the available power of the cluster, it is necessary to parallelize the script in such a way that it can use the maximum available computation resources. Otherwise, most of the time worker node would be remain idle and the cluster resources would be unused/wasted. However, in any case the communication overhead should be lower than the computational cost.

The rule of thumb in order to speedup the code is to mark those areas of the script that are time consuming. It can be marked easily using MATLAB® profiler. This is a very good approach and works very well for every kind of scenario. But

this approach requires modifications at grass roots level and, hence, sometimes it can become cumbersome. There is another tactic that is quite suitable if the problem is viewed from the EM perspective. For instance, in some problems parallelism inherently exists due to its structure, An example is the DFS polarizer where each building block (i.e. a single DFS) can be analyzed in parallel. In the three DFSs polarizer, each DFS scattering matrices are computed both for the vertical and the horizontal polarizations. Hence, as a result an overall of six full wave analysis have to be performed for a particular geometry having three DFSs. Since all these scattering matrices are completely independent from each other, they can be computed in parallel. If six worker nodes are used in order to compute the scattering matrices, then in principle one should obtain a speedup factor around five[4], but unfortunately for the DFS polarizer the problem is not very computationally intensive. Therefore, communication overhead becomes greater than the computational cost and, consequently, no significant acceleration is obtained in computation time. This study case reveals that if somehow we increase the computational cost for a single worker node than we can get the expected speedup factor. This can be achieved if each worker analyze a complete three DFS polarizer geometry. This methodology provides the expected results reported in section 5.4.

If the geometry to be analyzed is quite computationally intensive, then it can be parallelized over the frequency sweep. It means that the same structure is analyzed by different worker nodes for different frequency points. This parallelization strategy has been applied to the analysis of corrugated horns using an in-house tool obtaining the expected results discussed in detail in section 5.4.

Parallelization is a key feature also in optimization problems of RF components. MATLAB® PCT provides the acceleration feature also for optimization applications. For instance, during the optimization the gradient can be calculated in parallel. The optimization can also start with a multiple initial guess along the DC, but for this case MATLAB® Global Optimization Toolbox (GOT) is also required. All the above discussed promising methodology are summarized in Fig. 5.3.

[4]For ideal scenario, it would be six because six number of worker nodes are exploited but for a real scenario it is less than six due to the communication overhead.

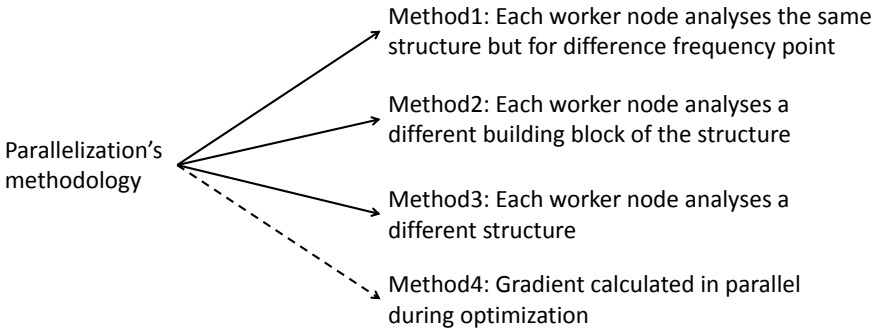

Figure 5.3. Possible methodologies for parallelization from EM perspective. All the indicated approaches can be exploited for both parametric analysis and optimization, except for the last one that can be exploited only for optimization as indicated by the dashed arrow.

5.4 MATLAB® DC For In-House Tool

A trial local cluster has been developed by exploiting some resources available at IEIIT-CNR. The local cluster consists of four identical Intel®desktop machines. Each machine is equipped with Intel®Core™ i7 – 3.40 GHz Processors(4 Cores) along with 8 GB Random Access Memory (RAM). The operating system installed on each machine is Microsoft Windows 7 Professional(64 bit). Four worker nodes[5] are hosted on each machine, so that the local cluster consists of 16 worker nodes. In this cluster configuration the head node also hosts four worker nodes. Hence, this configuration is slightly different from as the one shown in Fig. 5.1. The client node is defined separately so it is not the part of the cluster as shown in Fig. 5.1. On the cluster the MDCST(Version 6.3) is installed whereas on the client node MATLAB®(Version 8.2) along with PCT(Version 6.3) is installed. The PCT version on the client node should have the same version of the MDCST installed on worker node.

Two test cases have been studied in order to validate the effectiveness of the distributed computing approach. The three DFS polarizer reported in Fig. 5.5 and the corrugate horn reported in Fig. 5.7 are chosen as examples. Their full-wave analyses have been performed using the in-house tool described in [26] and [57], respectively. The parallelized version of each in-house tool has been developed so that it can run over the cluster[6].

The in-house tool developed for the three DFS polarizer has been parallelized for both parametric analysis (by means of method 3 of Fig. 5.3) and optimization (by

[5]worker nodes should be equal to the number of processor cores as recommended by MATLAB®

[6]Parallelized version should not have global and persistent variables. If global variables are used in the serial version of the script, then they should be removed and the corresponding parameters should be passed in every function as input arguments.

means of method 4 of Fig. 5.3). Figure 5.4 reports the corresponding speedup factors for the parametric analysis (dash line) and optimization (solid line) of the polarizer. A number of worker nodes equal to zero corresponds to serial programming, i.e. DC is not exploited, and it is regarded as a reference. In the parametric analysis of the polarizer (solid line) carried out by means of method 3 of Fig. 5.3 (i.e. each worker node evaluates the scattering matrix of a complete polarizer structure) a very good usage of the cluster resources is achieved, since this approach provides a speedup factor of about 15 by using 16 worker nodes. For the optimization test case, only *fmincon*, *fgoalattain* and *fminimax* MATLAB® solver support the parallelism. Since these solvers estimate the gradient of the objective function in various directions[7], the computation of the gradient can be carried out in parallel. In Fig. 5.4 it can be seen that the speedup factor in the optimization test case (dash curve) increases as the number of worker node is increased. However, it can also be noticed that after a certain extent the addition of worker nodes does not provide any significant advantage and that the speedup factor reaches a steady state. This behavior is due to the fact that, for this problem, the computation of the gradient exploits the cluster resources up to a certain extent. Indeed, it can be seen that using 14 and 16 worker nodes provides the same speedup factor. Its means that only 3.5 times acceleration is attainable by using method 4 over the cluster for this problem. As far as optimization is considered, the same method 4 of Fig. 5.3 is used in the corrugated horn test case. Since this problem is a bit more computationally intensive than the previous one, the maximum attainable speedup factor for this case is 5.7 for 16 worker nodes, as it is reported in Fig. 5.6 (dash curve). The speedup factor can be increased if each worker node analyzes the same structure of the corrugated horn but for different frequency points (method 1 of Fig. 5.3). For instance, if during the optimization the structure has to be analyzed at 16 frequency points, then it means that 16 structures can be analyzed in parallel. It can be seen from Fig. 5.6 (solid curve) that the obtained speedup factor is about 10 using 16 worker nodes.

[7]The number of gradients to be estimated depends on the length of the optimization vector x containing all the degree of freedom of the geometry.

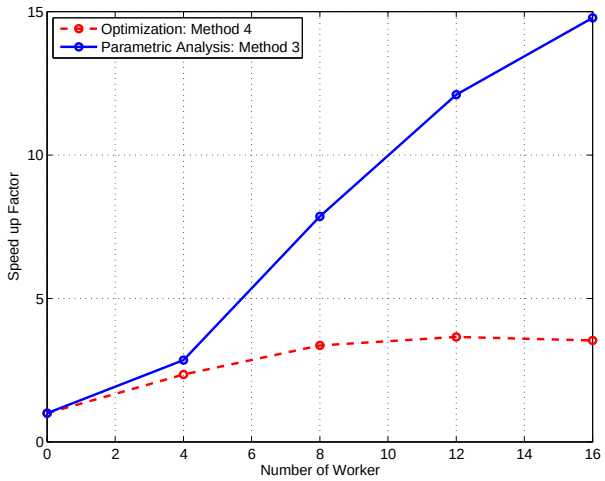

Figure 5.4. Speedup factor as a function of the number of worker nodes for the three DFS polarizer. A number of workers equal to zero refers to the case when MATLAB® Distributed Computing is not exploited (reference). Method 4 refers to the optimization test case where gradients are calculated in parallel. Method 3 refers to the parametric analysis test case where different structures are analyzed in parallel by different worker nodes.

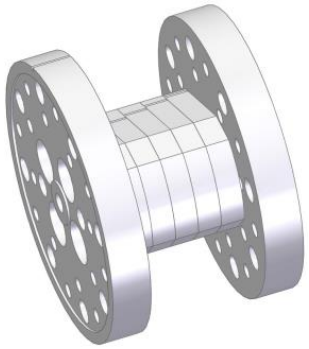

Figure 5.5. Geometry of the DFS polarizer that is studied for the parallelization methodologies 3 and 4 reported in Fig. 5.3.

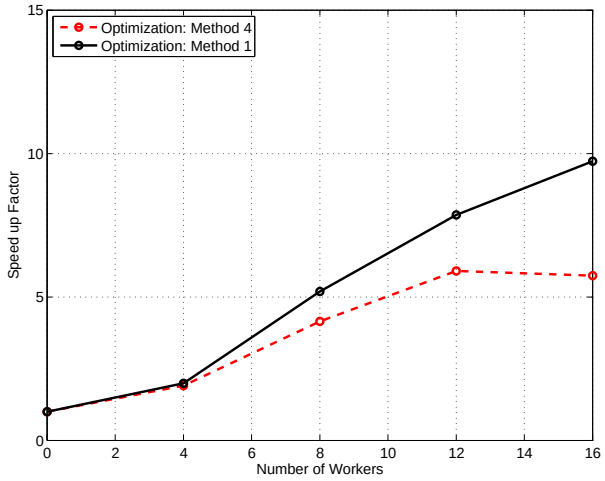

Figure 5.6. Speedup factor as a function of the number of worker nodes for the corrugated horn. A number of workers equal to zero refers to the case when MATLAB® Distributed Computing is not exploited (reference). Method 1 refers to the optimization analysis test case where the same structures is analyzed in parallel by different worker nodes for different frequency points. Method 4 refers to the optimization test case where gradients are calculated in parallel.

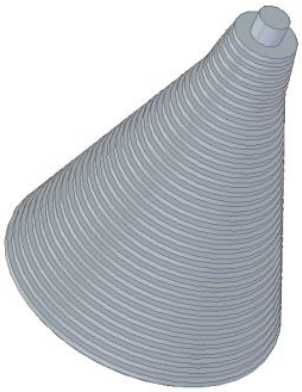

Figure 5.7. Geometry of the corrugated horn that is studied for the parallelization methodologies 1 and 4 reported in Fig. 5.3.

5.5 Conclusion

In the design of waveguide components, some time-consuming activities are envolved, e.g. optimization, parametric analysis and tolerance analysis. As an example, the latter can require thousands of geometries to be analyzed in order to measure the sensitivity of the structure. Therefore EM analysis tools should have reasonably low computation time. Reduction in computation time can be achieved either by making the analysis tool's algorithm more efficient or by exploiting some acceleration techniques. In this chapter, various acceleration methods have been reported, e.g. shared/distributed memory multiprocessing through OpenMP/OpenMPI or exploitation of cluster of GPUs through CUDA/OpenGL/OpenCL. Unfortunately their APIs are available for C/C++ whereas the available in-house analysis tool had been developed in MATLAB®. Finally, the MATLAB® DC approach has been exploited by employing the available toolboxes i.e. PCT with MDCST.

A local computer cluster has been developed using off the shelf Intel®Core™ i7 desktops and exploiting MDCST in order to perform the tolerance analysis and optimization of components in an accelerated fashion. Various parallelization methodologies have been investigated on the DFS polarizer and corrugated horn test cases by obtaining a speedup factor of about 15 and 6, respectively.

Appendix A

Polarizer:Matrix Transformations and Stokes Parameters

A.1 Basics on Polarization States of the Electric Field

In frequency domain with the $e^{j\omega t}$ time convention, the generic expression of the transverse electric field is:

$$\mathbf{E} = E_x\hat{\mathbf{x}} + E_y\hat{\mathbf{y}}$$

where

$$\begin{aligned} E_x &= \left|E_x\right| e^{j\varphi_x} \\ E_y &= \left|E_y\right| e^{j\varphi_y} \end{aligned}$$

The relevant time harmonic expression is:

$$\begin{aligned} \mathscr{E}(t) &= \Re\{\mathbf{E}e^{j\omega t}\} \\ \mathscr{E}(t) &= |E_x|\cos(\omega t + \varphi_x)\hat{\mathbf{x}} + |E_y|\cos(\omega t + \varphi_y)\hat{\mathbf{y}} \end{aligned}$$

Here we assume that the electric field polarization plane is orthogonal to z-axis. In order to derive the polarization characteristic of the field, it is useful to apply the time change $\omega t \rightarrow \omega t + \varphi_x$ then one obtains:

$$\mathscr{E}(t) = |E_x|\cos(\omega t)\hat{\mathbf{x}} + |E_y|\cos(\omega t + \Delta\varphi)\hat{\mathbf{y}}$$

where $\Delta\varphi = \varphi_y - \varphi_x$. Exploiting the standard trigonometric relation, one obtains:

$$\mathscr{E}(t) = (|E_x|\hat{\mathbf{x}} + |E_y|\cos(\Delta\varphi)\hat{\mathbf{y}})\cos(\omega t) - |E_y|\sin(\omega t)\sin(\Delta\varphi)\hat{\mathbf{y}} \qquad \text{(A.1)}$$

If $\Delta\varphi$ is 0 or an integer multiple of π i.e. then the expression (A.1) reduces to:

$$\mathscr{E}(t) = (|E_x|\hat{\mathbf{x}} \pm |E_y|\hat{\mathbf{y}})\cos(\omega t)$$

that means that the electric field direction is constant in the time: this case is referred as *linear polarization.*
If $\Delta\varphi = \pm\pi/2$ and $\left|E_x\right| = \left|E_y\right|$ then the expression (A.1) reduces to:

$$\mathscr{E}(t) = |E_y|\cos(\omega t)\hat{\mathbf{x}} \pm j|E_y|\sin(\omega t)\hat{\mathbf{y}}$$

that means that the electric field direction changes in the time and, in particular, rotates along a circle: this case is referred as *circular polarization.*

Finally, if electric field vector neither has linear polarization nor has circular polarization then it is said *elliptically polarized* since the tip of the **E** field traces an ellipse.

A.2 Scattering Matrix Transformation

$$\tilde{\mathbf{S}} = \mathbf{P}_b \cdot \mathbf{S} \cdot \mathbf{P}_a^{-1} \tag{A.2}$$

The analytical expression of the submatrices of $\tilde{\mathbf{S}}$, can be found by substituting the values of $\mathbf{P}_b$, $\mathbf{S}$ and $\mathbf{P}_a^{-1}$ in equation A.2.

$$\begin{bmatrix} \tilde{\mathbf{S}}_{11} & \tilde{\mathbf{S}}_{12} \\ \tilde{\mathbf{S}}_{21} & \tilde{\mathbf{S}}_{22} \end{bmatrix} = \begin{bmatrix} \check{\mathbf{T}} & \mathbf{0} \\ \mathbf{0} & \mathbf{T} \end{bmatrix} \begin{bmatrix} \mathbf{S}_{11} & \mathbf{S}_{12} \\ \mathbf{S}_{21} & \mathbf{S}_{22} \end{bmatrix} \begin{bmatrix} \hat{\mathbf{T}} & \mathbf{0} \\ \mathbf{0} & \mathbf{T} \end{bmatrix}^{-1}$$

$$\begin{bmatrix} \tilde{\mathbf{S}}_{11} & \tilde{\mathbf{S}}_{12} \\ \tilde{\mathbf{S}}_{21} & \tilde{\mathbf{S}}_{22} \end{bmatrix} = \begin{bmatrix} \check{\mathbf{T}} & \mathbf{0} \\ \mathbf{0} & \mathbf{T} \end{bmatrix} \begin{bmatrix} \mathbf{S}_{11} & \mathbf{S}_{12} \\ \mathbf{S}_{21} & \mathbf{S}_{22} \end{bmatrix} \begin{bmatrix} (\hat{\mathbf{T}})^{-1} & \mathbf{0} \\ \mathbf{0} & (\mathbf{T})^{-1} \end{bmatrix}$$

$$\begin{bmatrix} \tilde{\mathbf{S}}_{11} & \tilde{\mathbf{S}}_{12} \\ \tilde{\mathbf{S}}_{21} & \tilde{\mathbf{S}}_{22} \end{bmatrix} = \begin{bmatrix} \check{\mathbf{T}}\,\mathbf{S}_{11} & \check{\mathbf{T}}\,\mathbf{S}_{12} \\ \mathbf{T}\,\mathbf{S}_{21} & \mathbf{T}\,\mathbf{S}_{22} \end{bmatrix} \begin{bmatrix} (\hat{\mathbf{T}})^{-1} & \mathbf{0} \\ \mathbf{0} & (\mathbf{T})^{-1} \end{bmatrix}$$

$$\begin{bmatrix} \tilde{\mathbf{S}}_{11} & \tilde{\mathbf{S}}_{12} \\ \tilde{\mathbf{S}}_{21} & \tilde{\mathbf{S}}_{22} \end{bmatrix} = \begin{bmatrix} \check{\mathbf{T}}\,\mathbf{S}_{11}\,(\hat{\mathbf{T}})^{-1} & \check{\mathbf{T}}\,\mathbf{S}_{12}\,(\mathbf{T})^{-1} \\ \mathbf{T}\,\mathbf{S}_{21}\,(\hat{\mathbf{T}})^{-1} & \mathbf{T}\,\mathbf{S}_{22}\,(\mathbf{T})^{-1} \end{bmatrix}$$

Equating the corresponding elements leads to

$$\tilde{\mathbf{S}}_{11} = \check{\mathbf{T}}\,\mathbf{S}_{11}\,(\hat{\mathbf{T}})^{-1} \tag{A.3}$$

$$\tilde{\mathbf{S}}_{12} = \check{\mathbf{T}}\,\mathbf{S}_{12}\,(\mathbf{T})^{-1} \tag{A.4}$$

$$\tilde{\mathbf{S}}_{21} = \mathbf{T}\,\mathbf{S}_{21}\,(\hat{\mathbf{T}})^{-1} \tag{A.5}$$

$$\tilde{\mathbf{S}}_{22} = \mathbf{T}\,\mathbf{S}_{22}\,(\mathbf{T})^{-1} \tag{A.6}$$

In the subsequent paragraph an explicit mathematical expression is derived for $\tilde{\mathbf{S}}_{11}$, $\tilde{\mathbf{S}}_{12}$, $\tilde{\mathbf{S}}_{21}$ and $\tilde{\mathbf{S}}_{22}$ in terms of principal direction scattering elements.

For $\tilde{\mathbf{S}}_{11}$, consider equation (A.3)

$$\begin{aligned}
\tilde{\mathbf{S}}_{11} &= \check{\mathbf{T}}\,\mathbf{S}_{11}\,(\hat{\mathbf{T}})^{-1} \\
\tilde{\mathbf{S}}_{11} &= \frac{1}{\sqrt{2}}\begin{bmatrix} -j & 1 \\ j & 1 \end{bmatrix} \cdot \begin{bmatrix} s_{11} & s_{12} \\ s_{21} & s_{22} \end{bmatrix} \cdot \left(\frac{1}{\sqrt{2}}\begin{bmatrix} -j & 1 \\ j & 1 \end{bmatrix} \right)^{-1} \\
\tilde{\mathbf{S}}_{11} &= \frac{1}{\sqrt{2}}\begin{bmatrix} -j & 1 \\ j & 1 \end{bmatrix} \cdot \begin{bmatrix} s_{11} & s_{12} \\ s_{21} & s_{22} \end{bmatrix} \cdot \frac{1}{\sqrt{2}}\begin{bmatrix} -j & -j \\ 1 & 1 \end{bmatrix} \\
\tilde{\mathbf{S}}_{11} &= \frac{1}{2}\begin{bmatrix} -js_{11} + s_{21} & -js_{12} + s_{22} \\ js_{11} + s_{21} & js_{12} + s_{22} \end{bmatrix} \cdot \begin{bmatrix} -j & -j \\ 1 & 1 \end{bmatrix}
\end{aligned}$$

$$\tilde{\mathbf{S}}_{11} = \frac{1}{2}\begin{bmatrix} s_{22} - s_{11} - j(s_{12} + s_{21}) & s_{11} + s_{22} + j(-s_{12} + s_{21}) \\ s_{11} + s_{22} + j(s_{12} - s_{21}) & s_{22} - s_{11} + j(s_{12} + s_{21}) \end{bmatrix} \tag{A.7}$$

Consider equation (A.4)

$$\begin{aligned}
\tilde{\mathbf{S}}_{12} &= \check{\mathbf{T}}\,\mathbf{S}_{12}\,(\mathbf{T})^{-1} \\
\tilde{\mathbf{S}}_{12} &= \frac{1}{\sqrt{2}}\begin{bmatrix} j & 1 \\ -j & 1 \end{bmatrix} \cdot \begin{bmatrix} s_{13} & s_{14} \\ s_{23} & s_{24} \end{bmatrix} \cdot \left(\frac{1}{\sqrt{2}}\begin{bmatrix} 1 & 1 \\ -1 & 1 \end{bmatrix} \right)^{-1} \\
\tilde{\mathbf{S}}_{12} &= \frac{1}{\sqrt{2}}\begin{bmatrix} j & 1 \\ -j & 1 \end{bmatrix} \cdot \begin{bmatrix} s_{13} & s_{14} \\ s_{23} & s_{24} \end{bmatrix} \cdot \frac{1}{\sqrt{2}}\begin{bmatrix} 1 & -1 \\ 1 & 1 \end{bmatrix} \\
\tilde{\mathbf{S}}_{12} &= \frac{1}{2}\begin{bmatrix} -js_{13} + s_{23} & -js_{14} + s_{24} \\ js_{13} + s_{23} & js_{14} + s_{24} \end{bmatrix} \cdot \begin{bmatrix} 1 & -1 \\ 1 & 1 \end{bmatrix}
\end{aligned}$$

$$\tilde{\mathbf{S}}_{12} = \frac{1}{2}\begin{bmatrix} s_{23} + s_{24} - j(s_{13} + s_{14}) & s_{24} - s_{23} + j(s_{13} - s_{14}) \\ s_{23} + s_{24} + j(s_{13} + s_{14}) & s_{24} - s_{23} + j(-s_{13} + s_{14}) \end{bmatrix} \tag{A.8}$$

Consider equation (A.5)

$$\begin{aligned}
\tilde{\mathbf{S}}_{21} &= \mathbf{T}\,\mathbf{S}_{21}\,(\hat{\mathbf{T}})^{-1} \\
\tilde{\mathbf{S}}_{21} &= \frac{1}{\sqrt{2}}\begin{bmatrix} 1 & 1 \\ -1 & 1 \end{bmatrix} \cdot \begin{bmatrix} s_{31} & s_{32} \\ s_{41} & s_{42} \end{bmatrix} \cdot \left(\frac{1}{\sqrt{2}}\begin{bmatrix} j & 1 \\ -j & 1 \end{bmatrix} \right)^{-1} \\
\tilde{\mathbf{S}}_{21} &= \frac{1}{2}\begin{bmatrix} 1 & 1 \\ -1 & 1 \end{bmatrix} \cdot \begin{bmatrix} s_{31} & s_{32} \\ s_{41} & s_{42} \end{bmatrix} \cdot \begin{bmatrix} -j & j \\ 1 & 1 \end{bmatrix} \\
\tilde{\mathbf{S}}_{21} &= \frac{1}{2}\begin{bmatrix} s_{31} + s_{41} & s_{32} + s_{42} \\ -s_{31} + s_{41} & -s_{32} + s_{42} \end{bmatrix} \cdot \begin{bmatrix} -j & j \\ 1 & 1 \end{bmatrix}
\end{aligned}$$

$$\tilde{\mathbf{S}}_{21} = \frac{1}{2}\begin{bmatrix} s_{32}+s_{42}-j(s_{31}+s_{41}) & s_{32}+s_{42}+j(s_{31}+s_{41}) \\ s_{42}-s_{32}+j(s_{31}-s_{41}) & s_{42}-s_{32}-j(s_{31}-s_{41}) \end{bmatrix} \tag{A.9}$$

Similarly consider equation (A.6)

$$\begin{aligned}
\tilde{\mathbf{S}}_{22} &= \mathbf{T}\,\mathbf{S}_{22}\,(\mathbf{T})^{-1} \\
\tilde{\mathbf{S}}_{22} &= \frac{1}{\sqrt{2}}\begin{bmatrix} 1 & 1 \\ -1 & 1 \end{bmatrix} \cdot \begin{bmatrix} s_{33} & s_{34} \\ s_{43} & s_{44} \end{bmatrix} \cdot \left(\frac{1}{\sqrt{2}}\begin{bmatrix} 1 & 1 \\ -1 & 1 \end{bmatrix} \right)^{-1} \\
\tilde{\mathbf{S}}_{22} &= \frac{1}{\sqrt{2}}\begin{bmatrix} 1 & 1 \\ -1 & 1 \end{bmatrix} \cdot \begin{bmatrix} s_{33} & s_{34} \\ s_{43} & s_{44} \end{bmatrix} \cdot \frac{1}{\sqrt{2}}\begin{bmatrix} 1 & -1 \\ 1 & 1 \end{bmatrix} \\
\tilde{\mathbf{S}}_{22} &= \frac{1}{2}\begin{bmatrix} s_{33}+s_{43} & s_{34}+s_{44} \\ -s_{33}+s_{43} & -s_{34}+s_{44} \end{bmatrix} \cdot \begin{bmatrix} 1 & -1 \\ 1 & 1 \end{bmatrix}
\end{aligned}$$

$$\tilde{\mathbf{S}}_{22} = \frac{1}{2}\begin{bmatrix} s_{33}+s_{34}+s_{43}+s_{44} & s_{34}-s_{33}-s_{43}+s_{44} \\ s_{43}-s_{34}-s_{33}+s_{44} & s_{33}-s_{34}-s_{43}+s_{44} \end{bmatrix} \tag{A.10}$$

A.3 Stokes Parameter's Formulation for Polarizer

A generic incident field at the polarizer physical port 1 has the following expression:

$$\mathbf{E}_1^{inc} = E_R\hat{\mathbf{e}}_\mathbf{R} + E_L\hat{\mathbf{e}}_\mathbf{L}$$

It generates a scattered field at the physical port 2, which is given as,

$$\mathbf{E}_2^{scat} = \left(E_R\tilde{s}_{31} + E_L\tilde{s}_{32}\right)\hat{\mathbf{u}} + \left(E_R\tilde{s}_{41} + E_L\tilde{s}_{42}\right)\hat{\mathbf{v}} = E_u\hat{\mathbf{u}} + E_v\hat{\mathbf{v}}$$

where

$$\begin{aligned}
E_u &= E_R\tilde{s}_{31} + E_L\tilde{s}_{32} = \frac{E_R}{2}\left[\left(s_{42}+s_{32}\right) - j\left(s_{31}+s_{41}\right)\right] + \frac{E_L}{2}\left[\left(s_{42}+s_{32}\right) + j\left(s_{31}+s_{41}\right)\right] \\
E_v &= E_R\tilde{s}_{41} + E_L\tilde{s}_{42} = \frac{E_R}{2}\left[\left(s_{42}-s_{32}\right) + j\left(s_{31}-s_{41}\right)\right] + \frac{E_L}{2}\left[\left(s_{42}-s_{32}\right) - j\left(s_{31}-s_{41}\right)\right]
\end{aligned}$$

Since $Q_m = 2\Re\{E_vE_u^*\}$ and $U_m = -2\Im\{E_vE_u^*\}$, let us consider in detail the product $E_vE_u^*$:

$$\begin{aligned}
E_vE_u^* = \; & \left[\frac{E_R}{2}\left[\left(s_{42}-s_{32}\right) + j\left(s_{31}-s_{41}\right)\right] + \frac{E_L}{2}\left[\left(s_{42}-s_{32}\right) - j\left(s_{31}-s_{41}\right)\right]\right] \cdot \\
& \left[\frac{E_R}{2}\left[\left(s_{42}+s_{32}\right) - j\left(s_{31}+s_{41}\right)\right] + \frac{E_L}{2}\left[\left(s_{42}+s_{32}\right) + j\left(s_{31}+s_{41}\right)\right]\right]^*
\end{aligned}$$

Apply conjugate and multiply both side by a factor 4

$$\begin{aligned}4E_v E_u^* = \; & \left[E_R\left[\left(s_{42}-s_{32}\right)+j\left(s_{31}-s_{41}\right)\right]+E_L\left[\left(s_{42}-s_{32}\right)-j\left(s_{31}-s_{41}\right)\right]\right]\cdot \\ & \left[E_R^*\left[\left(s_{42}^*+s_{32}^*\right)+j\left(s_{31}^*+s_{41}^*\right)\right]+E_L^*\left[\left(s_{42}^*+s_{32}^*\right)-j\left(s_{31}^*+s_{41}^*\right)\right]\right]\end{aligned}$$

Collect $|E_R|^2$, $E_R E_L^*$, $E_L E_R^*$ and $|E_L|^2$ terms

$$\begin{aligned}4E_v E_u^* = \; & |E_R|^2\left(\left(s_{42}-s_{32}\right)+j\left(s_{31}-s_{41}\right)\right)\left(\left(s_{32}^*+s_{42}^*\right)+j\left(s_{31}^*+s_{41}^*\right)\right) \\ + \; & E_R E_L^*\left(\left(s_{42}-s_{32}\right)+j\left(s_{31}-s_{41}\right)\right)\left(\left(s_{32}^*+s_{42}^*\right)-j\left(s_{31}^*+s_{41}^*\right)\right) \\ + \; & E_L E_R^*\left(\left(s_{42}-s_{32}\right)-j\left(s_{31}-s_{41}\right)\right)\left(\left(s_{32}^*+s_{42}^*\right)+j\left(s_{31}^*+s_{41}^*\right)\right) \\ + \; & |E_L|^2\left(\left(s_{42}-s_{32}\right)-j\left(s_{31}-s_{41}\right)\right)\left(\left(s_{32}^*+s_{42}^*\right)-j\left(s_{31}^*+s_{41}^*\right)\right)\end{aligned}$$

Multiply

$$\begin{aligned}4E_v E_u^* = \; & |E_R|^2\left(s_{42}-s_{32}\right)\left(s_{32}^*+s_{42}^*\right)+j|E_R|^2\left(s_{42}-s_{32}\right)\left(s_{31}^*+s_{41}^*\right) \\ + \; & j|E_R|^2\left(s_{31}-s_{41}\right)\left(s_{32}^*+s_{42}^*\right)-|E_R|^2\left(s_{31}-s_{41}\right)\left(s_{31}^*+s_{41}^*\right) \\ + \; & E_R E_L^*\left(s_{42}-s_{32}\right)\left(s_{32}^*+s_{42}^*\right)-j*E_R E_L^*\left(s_{42}-s_{32}\right)\left(s_{31}^*+s_{41}^*\right) \\ + \; & jE_R E_L^*\left(s_{31}-s_{41}\right)\left(s_{32}^*+s_{42}^*\right)+E_R E_L^*\left(s_{31}-s_{41}\right)\left(s_{31}^*+s_{41}^*\right) \\ + \; & E_L E_R^*\left(s_{42}-s_{32}\right)\left(s_{32}^*+s_{42}^*\right)+jE_L E_R^*\left(s_{42}-s_{32}\right)\left(s_{31}^*+s_{41}^*\right) \\ - \; & jE_L E_R^*\left(s_{31}-s_{41}\right)\left(s_{32}^*+s_{42}^*\right)+E_L E_R^*\left(s_{31}-s_{41}\right)\left(s_{31}^*+s_{41}^*\right) \\ + \; & |E_L|^2\left(s_{42}-s_{32}\right)\left(s_{32}^*+s_{42}^*\right)-j|E_L|^2\left(s_{42}-s_{32}\right)\left(s_{31}^*+s_{41}^*\right) \\ - \; & j|E_L|^2\left(s_{31}-s_{41}\right)\left(s_{32}^*+s_{42}^*\right)-|E_L|^2\left(s_{31}-s_{41}\right)\left(s_{31}^*+s_{41}^*\right)\end{aligned}$$

collect the common terms

$$\begin{aligned}4E_v E_u^* = \; & \left(s_{42}-s_{32}\right)\left(s_{32}^*+s_{42}^*\right)\left(|E_R|^2+E_R E_L^*+E_L E_R^*+|E_L|^2\right) \\ + \; & j\left(s_{42}-s_{32}\right)\left(s_{31}^*+s_{41}^*\right)\left(|E_R|^2-E_R E_L^*+E_L E_R^*-|E_L|^2\right) \\ + \; & j\left(s_{31}-s_{41}\right)\left(s_{32}^*+s_{42}^*\right)\left(|E_R|^2+E_R E_L^*-E_L E_R^*-|E_L|^2\right) \\ + \; & \left(s_{31}-s_{41}\right)\left(s_{31}^*+s_{41}^*\right)\left(-|E_R|^2+E_R E_L^*+E_L E_R^*-|E_L|^2\right)\end{aligned}$$

exploit the identities: $a^*b+ab^*=2\Re\{ab^*\}$ and $a^*b-ab^*=-2j\Im\{ab^*\}$

$$\begin{aligned}4E_v E_u^* = \; & \left(s_{42}-s_{32}\right)\left(s_{42}^*+s_{32}^*\right)\left(|E_R|^2+2\Re\{E_L E_R^*\}+|E_L|^2\right) \\ + \; & j\left(s_{42}-s_{32}\right)\left(s_{31}^*+s_{41}^*\right)\left(|E_R|^2+2j\Im\{E_L E_R^*\}-|E_L|^2\right) \\ + \; & j\left(s_{31}-s_{41}\right)\left(s_{32}^*+s_{42}^*\right)\left(|E_R|^2-2j\Im\{E_L E_R^*\}-|E_L|^2\right) \\ + \; & \left(s_{31}-s_{41}\right)\left(s_{31}^*+s_{41}^*\right)\left(-|E_R|^2+2\Re\{E_L E_R^*\}-|E_L|^2\right)\end{aligned}$$

Multiply,

$$\begin{aligned}
4E_v E_u^* = & \left(|s_{42}|^2 - |s_{32}|^2 + 2j\Im\{s_{42}s_{32}^*\}\right)\left(|E_R|^2 + 2\Re\{E_L E_R^*\} + |E_L|^2\right) \\
- & \; j\left(s_{42}s_{31}^* + s_{42}s_{41}^* - s_{31}^*s_{32} - s_{32}s_{41}^*\right)\left(-|E_R|^2 - 2j\Im\{E_L E_R^*\} + |E_L|^2\right) \\
- & \; j\left(s_{31}s_{32}^* + s_{31}s_{42}^* - s_{32}^*s_{41} - s_{41}s_{42}^*\right)\left(-|E_R|^2 + 2j\Im\{E_L E_R^*\} + |E_L|^2\right) \\
+ & \left(|s_{31}|^2 - |s_{41}|^2 + 2j\Im\{s_{31}s_{41}^*\}\right)\left(-|E_R|^2 + 2\Re\{E_L E_R^*\} - |E_L|^2\right)
\end{aligned}$$

Exploit the stokes parameters definition, as defined in Eq.(1.17)

$$\begin{aligned}
4E_v E_u^* = & \left(|s_{42}|^2 - |s_{32}|^2 + 2j\Im\{s_{42}s_{32}^*\}\right)(I+Q) \\
- & \; j\left(s_{42}s_{31}^* + s_{42}s_{41}^* - s_{31}^*s_{32} - s_{32}s_{41}^*\right)(V+jU) \\
- & \; j\left(s_{31}s_{32}^* + s_{31}s_{42}^* - s_{32}^*s_{41} - s_{41}s_{42}^*\right)(V-jU) \\
- & \left(|s_{31}|^2 - |s_{41}|^2 + 2j\Im\{s_{31}s_{41}^*\}\right)(I-Q)
\end{aligned}$$

Collect Q, U, I and V terms

$$\begin{aligned}
4E_v E_u^* = & \left(|s_{42}|^2 - |s_{32}|^2 + 2j\Im\{s_{42}s_{32}^*\} + |s_{31}|^2 - |s_{41}|^2 + 2j\Im\{s_{31}s_{41}^*\}\right)Q \\
+ & \left(s_{42}s_{31}^* + s_{42}s_{41}^* - s_{31}^*s_{32} - s_{32}s_{41}^* - s_{31}s_{32}^* - s_{31}s_{42}^* + s_{32}^*s_{41} + s_{41}s_{42}^*\right)U \\
+ & \left(|s_{42}|^2 - |s_{32}|^2 + 2j\Im\{s_{42}s_{32}^*\} - |s_{31}|^2 + |s_{41}|^2 - 2j\Im\{s_{31}s_{41}^*\}\right)I \\
- & \; j\left(s_{42}s_{31}^* + s_{42}s_{41}^* - s_{31}^*s_{32} - s_{32}s_{41}^* + s_{31}s_{32}^* + s_{31}s_{42}^* - s_{32}^*s_{41} - s_{41}s_{42}^*\right)V
\end{aligned}$$

Rearrange,

$$\begin{aligned}
4E_v E_u^* = & \left(|s_{42}|^2 - |s_{32}|^2 + |s_{31}|^2 - |s_{41}|^2 + 2j\Im\{s_{42}s_{32}^*\} + 2j\Im\{s_{31}s_{41}^*\}\right)Q \\
+ & \left(2j\Im\{s_{42}s_{31}^*\} + 2\Re\{s_{41}s_{42}^*\} - 2\Re\{s_{31}s_{32}^*\} - 2j\Im\{s_{32}s_{41}^*\}\right)U \\
+ & \left(|s_{42}|^2 - |s_{32}|^2 - |s_{31}|^2 + |s_{41}|^2 + 2j\Im\{s_{42}s_{32}^*\} - 2j\Im\{s_{31}s_{41}^*\}\right)I \\
- & \; j\left(2\Re\{s_{42}s_{31}^*\} - 2j\Im\{s_{41}s_{42}^*\} + 2j\Im\{s_{31}s_{32}^*\} - 2\Re\{s_{32}s_{41}^*\}\right)V
\end{aligned}$$

separate Q, U, I and V terms real and imaginary part

$$\begin{aligned}
2E_v E_u^* = & \; \frac{1}{2}\left(|s_{42}|^2 - |s_{32}|^2 + |s_{31}|^2 - |s_{41}|^2\right)Q + \left(\Re\{s_{41}s_{42}^*\} - \Re\{s_{31}s_{32}^*\}\right)U \\
+ & \; \frac{1}{2}\left(|s_{42}|^2 - |s_{32}|^2 - |s_{31}|^2 + |s_{41}|^2\right)I + \left(-\Im\{s_{41}s_{42}^*\} + \Im\{s_{31}s_{32}^*\}\right)V \\
+ & \; j\left(\Im\{s_{42}s_{32}^*\} + \Im\{s_{31}s_{41}^*\}\right)Q + j\left(\Im\{s_{42}s_{31}^*\} - \Im\{s_{32}s_{41}^*\}\right)U \\
+ & \; j\left(\Im\{s_{42}s_{32}^*\} - \Im\{s_{31}s_{41}^*\}\right)I - j\left(\Re\{s_{42}s_{31}^*\} - \Re\{s_{32}s_{41}^*\}\right)V
\end{aligned}$$

Since $Q_m = 2\Re\{E_v E_u^*\}$ we have:

$$\begin{aligned} Q_m &= \frac{1}{2}\left(\left|s_{42}\right|^2 - \left|s_{32}\right|^2 + \left|s_{31}\right|^2 - \left|s_{41}\right|^2\right) Q + \left(\Re\{s_{41}s_{42}^*\} - \Re\{s_{31}s_{32}^*\}\right) U \\ &+ \frac{1}{2}\left(\left|s_{42}\right|^2 - \left|s_{32}\right|^2 - \left|s_{31}\right|^2 + \left|s_{41}\right|^2\right) I + \left(-\Im\{s_{41}s_{42}^*\} + \Im\{s_{31}s_{32}^*\}\right) V \end{aligned}$$

In similar way, since $U_m = -2\Im\{E_v E_u^*\}$:

$$\begin{aligned} U_m &= -\left(\Im\{s_{42}s_{32}^*\} + \Im\{s_{31}s_{41}^*\}\right) Q + \left(\Im\{s_{32}s_{41}^*\} - \Im\{s_{42}s_{31}^*\}\right) U \\ &+ \left(-\Im\{s_{42}s_{32}^*\} + \Im\{s_{31}s_{41}^*\}\right) I + \left(\Re\{s_{42}s_{31}^*\} - \Re\{s_{32}s_{41}^*\}\right) V \end{aligned}$$

Appendix B

OMT: Stokes Parameters

B.1 Stokes Parameter's Formulation for OMT

The generic expression of the incident electric field vector at the common waveguide circular/rectangular port is given as,

$$\mathbf{E}_1^{\mathbf{inc}} = E_y\hat{\mathbf{y}} + E_x\hat{\mathbf{x}}$$

Then, the scattered filed component along $\hat{\mathbf{y}}$ and $\hat{\mathbf{x}}$ direction at physical port 2 and 3 (see Fig. 3.25) of OMT are given as,

$$\begin{aligned} E_2^{scat} &= s_{31}E_y + s_{32}E_x \\ E_3^{scat} &= s_{41}E_y + s_{42}E_x \end{aligned}$$

The measured Stokes parameters Q_m and U_m are proportional to the real and imaginary parts of the product $E_3^{scat}(E_2^{scat})^*$, respectively. This product is given as,

$$\begin{aligned} E_3^{scat}(E_2^{scat})^* &= (s_{41}E_y + s_{42}E_x)(s_{31}E_y + s_{32}E_x)^* \\ E_3^{scat}(E_2^{scat})^* &= (s_{41}E_y + s_{42}E_x)(s_{31}^*E_y^* + s_{32}^*E_x^*) \\ E_3^{scat}(E_2^{scat})^* &= s_{41}s_{31}^*|E_y|^2 + s_{41}s_{32}^*E_rE_x^* + s_{42}s_{31}^*E_xE_y^* + s_{42}s_{32}^*|E_x|^2 \end{aligned} \quad \text{(B.1)}$$

Exploiting the Stoke parameters definition

$$\begin{aligned} Q &= 2\Re\{E_xE_y^*\} \\ U &= -2\Im\{E_xE_y^*\} \\ I &= |E_x|^2 + |E_y|^2 \\ V &= |E_x|^2 - |E_y|^2 \end{aligned}$$

one deduces:

$$2|E_x|^2 = I + V$$

$$\begin{aligned} 2|E_y|^2 &= I - V \\ 2E_x E_y^* &= Q - jU \\ 2E_y E_x^* &= Q + jU \end{aligned}$$

Substituting these relations in (B.1) one obtains:

$$E_3^{scat}(E_2^{scat})^* = \frac{1}{2}\left(s_{41}s_{32}^* + s_{42}s_{31}^*\right)Q + \frac{i}{2}\left(s_{41}s_{32}^* - s_{42}s_{31}^*\right)U + \frac{1}{2}\left(s_{41}s_{31}^* + s_{42}s_{32}^*\right)I + \frac{1}{2}\left(s_{42}s_{32}^* - s_{41}s_{31}^*\right)V$$

Since $Q_m = 2\Re\{E_3^{scat}(E_2^{scat})^*\}$, therefore:

$$Q_m = \Re\{s_{41}s_{32}^* + s_{42}s_{31}^*\}Q + \Im\{-s_{41}s_{32}^* + s_{42}s_{31}^*\}U + \Re\{s_{41}s_{31}^* + s_{42}s_{32}^*\}I + \Re\{s_{42}s_{32}^* - s_{41}s_{31}^*\}V$$

Similarly, since $U_m = -2\Im\{E_3^{scat}(E_2^{scat})^*\}$, therefore:

$$U_m = -\Im\{s_{41}s_{32}^* + s_{42}s_{31}^*\}Q + \Re\{-s_{41}s_{32}^* + s_{42}s_{31}^*\}U - \Im\{s_{41}s_{31}^* + s_{42}s_{32}^*\}I - \Im\{s_{42}s_{32}^* - s_{41}s_{31}^*\}V$$

In matrix form:

$$\begin{bmatrix} Q_m \\ U_m \end{bmatrix} = \mathbf{H} \cdot \begin{bmatrix} Q \\ U \end{bmatrix} + \mathbf{K} \cdot \begin{bmatrix} I \\ V \end{bmatrix}$$

where

$$\mathbf{H} = \begin{bmatrix} H_{QQ} & H_{QU} \\ H_{UQ} & H_{UU} \end{bmatrix}, \ \mathbf{K} = \begin{bmatrix} K_{QI} & K_{QV} \\ K_{UI} & H_{UV} \end{bmatrix}$$

where

$$\begin{aligned} H_{QQ} &= \Re\{s_{41}s_{32}^* + s_{42}s_{31}^*\} \\ H_{QU} &= \Im\{-s_{41}s_{32}^* + s_{42}s_{31}^*\} \\ H_{UQ} &= -\Im\{s_{41}s_{32}^* + s_{42}s_{31}^*\} \\ H_{UU} &= \Re\{-s_{41}s_{32}^* + s_{42}s_{31}^*\} \end{aligned}$$

and

$$\begin{aligned} K_{QI} &= \Re\{s_{41}s_{31}^* + s_{42}s_{32}^*\} \\ K_{QV} &= \Re\{s_{42}s_{32}^* - s_{41}s_{31}^*\} \\ K_{UI} &= -\Im\{s_{41}s_{31}^* + s_{42}s_{32}^*\} \\ K_{UV} &= -\Im\{s_{42}s_{32}^* - s_{41}s_{31}^*\} \end{aligned}$$

Bibliography

[1] S. Renaux-Petel, C. Fidler, C. Pitrou, and G. W. Pettinari, "Spectral distortions in the cosmic microwave background polarization," *ArXiv e-prints*, Dec. 2013.

[2] J. E. Carlstrom, J. Kovac, E. M. Leitch, and C. Pryke, "Status of CMB polarization measurements from DASI and other experiments," *New Astronomy Review*, vol. 47, pp. 953–966, Dec. 2003.

[3] S. De and H. Tashiro, "Circular Polarization of the CMB: A probe of the First stars," *ArXiv*, Jan. 2014.

[4] R. Mohammadi, "Evidence for cosmic neutrino background form CMB circular polarization," *ArXiv*, Dec. 2013.

[5] W. Hu and M. White, "A CMB polarization primer," *New Astronomy*, vol. 2, pp. 323–344, Oct. 1997.

[6] D. S. et al, "Measuring the Cosmic Microwave Background Radiation (CMBR) polarization with QUIET," in *A Century of Cosmology, San Servolo (Venezia, Italy)*. Il Nuovo Cimento, 2008.

[7] M. Bersanelli, A. Mennella, G. Morgante, M. Zannoni, G. Addamo, A. Baschirotto, P. Battaglia, A. Baù, B. Cappellini, F. Cavaliere, F. Cuttaia, F. Del Torto, S. Donzelli, Z. Farooqui, M. Frailis, C. Franceschet, E. Franceschi, T. Gaier, S. Galeotta, M. Gervasi, A. Gregorio, P. Kangaslahti, N. Krachmalnicoff, C. Lawrence, G. Maggio, R. Mainini, D. Maino, N. Mandolesi, B. Paroli, A. Passerini, O. A. Peverini, S. Poli, S. Ricciardi, M. Rossetti, M. Sandri, M. Seiffert, L. Stringhetti, A. Tartari, R. Tascone, D. Tavagnacco, L. Terenzi, M. Tomasi, E. Tommasi, F. Villa, G. Virone, and A. Zacchei, "A coherent polarimeter array for the Large Scale Polarization Explorer (LSPE) balloon experiment," in *Society of Photo-Optical Instrumentation Engineers (SPIE) Conference Series*, ser. Society of Photo-Optical Instrumentation Engineers (SPIE) Conference Series, vol. 8446, Sep. 2012.

[8] J. Cano, E. Villa, J. Cagigas, B. Aja, J. Teran, A. Perez, L. de la Fuente, E. Artal, A. Mediavilla, and R. Hoyland, "EM developments for a radio astronomy polarimeter: The QUIJOTE experiment," in *EM Technologies For Astrophysics, ICEAA*, 2013.

[9] ——, "Multi-pixel ka-band radiometer for the QUIJOTE experiment (phase ii)," in *Microwave Conference (EuMC), 42nd European*, 2012, pp. 37–40.

[10] O. Peverini, G. Virone, G. Addamo, Z. Farooqui, M. Lumia, and R. Tascone, "Dual-polarization passive waveguide sub-assemblies for astrophysics," in *Electromagnetics in Advanced Applications (ICEAA), 2013 International Conference on*, 2013, pp. 1531–1532.

[11] G. Virone, O. Peverini, G. Addamo, Z. Farooqui, and R. Tascone, "Platelet Ortho-mode Transducer (OMT) for millimeter-wave applications," in *Electromagnetics in Advanced Applications (ICEAA), 2013 International Conference on*, 2013, pp. 394–395.

[12] M. Kangas, K. Copsey, and P. Lubin, "A modular 100-ghz high-gain scalar corrugated nonbonded platelet antenna," *Antennas and Wireless Propagation Letters, IEEE*, vol. 4, pp. 89–92, 2005.

[13] J. W. Britton, J. P. Nibarger, K. W. Yoon, J. A. Beall, D. Becker, H.-M. Cho, G. C. Hilton, J. Hubmayr, M. D. Niemack, and K. D. Irwin, "Corrugated silicon platelet feed horn array for CMB polarimetry at 150 GHz," in *Society of Photo-Optical Instrumentation Engineers (SPIE) Conference Series*, vol. 7741, Jul. 2010.

[14] R. W. Haas, "Further Development of MMW and SMMW Platelet Feed Horn Arrays," in *Multi-Feed Systems for Radio Telescopes*, ser. Astronomical Society of the Pacific Conference Series, D. T. Emerson and J. M. Payne, Eds., vol. 75, 1995, p. 99.

[15] F. Del Torto, M. Bersanelli, C. Franceschet, O. Peverini, A. Simonetto, R. Tascone, and G. Virone, "A platelet w-band feed horn-omt assembly," in *Electromagnetics in Advanced Applications (ICEAA), 2013 International Conference on*, 2013, pp. 939–941.

[16] J. Gundersen and E. Wollack, "Millimeter Wave Corrugated Platelet Feeds," in *Workshop on Technology Development for a CMB Probe Inflation*, Boulder, Colorado, August 2008.

[17] F. Del Torto, M. Bersanelli, F. Cavaliere, A. De Rosa, O. D'Arcangelo, C. Franceschet, M. Gervasi, A. Mennella, E. Pagana, A. Simonetto, A. Tartari, F. Villa, and M. Zannoni, "W-band prototype of platelet feed-horn array for CMB polarisation measurements," *Journal of Instrumentation*, vol. 6, p. 6009, Jun. 2011.

[18] G. Virone, R. Tascone, O. Peverini, and R. Orta, "Optimum-iris-set concept for waveguide polarizers," *Microwave and Wireless Components Letters, IEEE*, vol. 17, no. 3, pp. 202 –204, march 2007.

[19] G. Bertin, B. Piovano, L. Accatino, and M. Mongiardo, "Full-wave design and optimization of circular waveguide polarizers with elliptical irises," *Microwave Theory and Techniques, IEEE Transactions on*, vol. 50, no. 4, pp. 1077–1083, 2002.

[20] D. Goldstein, *Polarized Light Revised and Expanded.* Marcel Dekker Inc; 2nd Revised edition (June 13), 2003.

[21] G. Virone, R. Tascone, M. Baralis, A. Olivieri, O. A. Peverini, and R. Orta, "Five-level waveguide correlation unit for astrophysical polarimetric measurements," *Microwave Theory and Techniques, IEEE Transactions on*, vol. 55, no. 2, pp. 309 –317, feb. 2007.

[22] J. Rebollar and J. Esteban, "Cad of corrugated circular-rectangular waveguide polarizers," in *Antennas and Propagation, 1993., Eighth International Conference on*, 1993, pp. 845–848 vol.2.

[23] N. Yoneda, M. Miyazaki, H. Matsumura, and M. Yamato, "A design of novel grooved circular waveguide polarizers," in *Microwave Symposium Digest. 2000 IEEE MTT-S International*, vol. 3, 2000, pp. 1449 –1452 vol.3.

[24] J. Bornemann, S. Amari, J. Uher, and R. Vahldieck, "Analysis and design of circular ridged waveguide components," *Microwave Theory and Techniques, IEEE Transactions on*, vol. 47, no. 3, pp. 330–335, 1999.

[25] G. Virone, R. Tascone, M. Baralis, O. Peverini, A. Olivieri, and R. Orta, "A novel design tool for waveguide polarizers," *Microwave Theory and Techniques, IEEE Transactions on*, vol. 53, no. 3, pp. 888 – 894, march 2005.

[26] O. Peverini, G. Addamo, G. Virone, R. Tascone, and R. Orta, "A spectral-element method for the analysis of 2-d waveguide devices with sharp edges and irregular shapes," *Microwave Theory and Techniques, IEEE Transactions on*, vol. 59, no. 7, pp. 1685–1695, 2011.

[27] M. M. LABoratory), "Numerical computing environment and fourth-generation programming language," http://www.cst.com/Content/Products/MWS/Overview.aspx.

[28] A. H. F. S. Simulator)., "Electromagnetic Simulation Software," http://www.ansys.com/Products/Simulation+Technology/Electromagnetics.

[29] C. S. Technology), "3D Electromagnetic Simulation Software," http://www.cst.com/Content/Products/MWS/Overview.aspx.

[30] M. J. D. Powell, *A fast algorithm for nonlinearly constrained optimization calculations*. Springer Verlag, 1978, vol. 630.

[31] Flann Microwave Ltd, "Rectangular To Circular Waveguide Transition WR10 Flanges UG," http://www.flann.com/Products_Home/Transition_Polarisers/transition_polarisers.html.

[32] C. Leal-Sevillano, Y. Tian, M. Lancaster, J. Ruiz-Cruz, J. Montejo-Garai, and J. Rebollar, "A Micromachined Dual-Band Orthomode Transducer," *Microwave Theory and Techniques, IEEE Transactions on*, vol. PP, no. 99, pp. 1–9, 2013.

[33] A. Dunning, S. Srikanth, and A. R. Kerr, "A Simple Orthomode Transducer for Centimeter to Submillimeter Wavelengths," in *20th International Symposium on Space Terahertz Technology, Charlottesville*, 2009, pp. 191–194.

[34] A. Boifot, E. Lier, and T. Schaug-Pettersen, "Simple and broadband orthomode transducer (antenna feed)," *Microwaves, Antennas and Propagation, IEE Proceedings H*, vol. 137, no. 6, pp. 396–400, 1990.

[35] T.-L. Zhang, Z.-H. Yan, L. Chen, and F.-F. Fan, "Design of broadband orthomode transducer based on double ridged waveguide," in *Microwave and Millimeter Wave Technology (ICMMT), 2010 International Conference on*, 2010, pp. 765–768.

[36] G. Pisano, L. Pietranera, K. Isaak, L. Piccirillo, B. Johnson, B. Maffei, and S. Melhuish, "A broadband wr10 turnstile junction orthomode transducer," *Microwave and Wireless Components Letters, IEEE*, vol. 17, no. 4, pp. 286–288, 2007.

[37] A.-A. San-Blas, F. J. Perez, J. Gil, F. Mira, V. E. Boria, and B. G. Martinez, "Full-wave analysis and design of broadband turnstile junctions," in *Progress In Electromagnetics Research(PIER)*, vol. 24, 2011, pp. 149–158.

[38] S.-G. Park, H. Lee, and Y.-H. Kim, "A turnstile junction waveguide orthomode transducer for the simultaneous dual polarization radar," in *Microwave Conference, 2009. APMC 2009. Asia Pacific*, 2009, pp. 135–138.

[39] Y. Aramaki, N. Yoneda, M. Miyazaki, and T. Horie, "Ultra-thin broadband omt with turnstile junction," in *Microwave Symposium Digest, 2003 IEEE MTT-S International*, vol. 1, 2003, pp. 47–50 vol.1.

[40] A. Navarrini and R. Plambeck, "A turnstile junction waveguide orthomode transducer," *Microwave Theory and Techniques, IEEE Transactions on*, vol. 54, no. 1, pp. 272–277, 2006.

[41] S. Srikanth and M. Solatka, "A compact full waveguide band turnstile junction orthomode transducer," in *General Assembly and Scientific Symposium, 2011 XXXth URSI*, 2011, pp. 1–4.

[42] O. Peverini, R. Tascone, A. Olivieri, M. Baralis, R. Orta, and G. Virone, "A microwave measurement procedure for a full characterization of ortho-mode transducers," *Microwave Theory and Techniques, IEEE Transactions on*, vol. 51, no. 4, pp. 1207–1213, 2003.

[43] B.-Z. W. Shu-Hui Sun, "Parameter Optimization Based on GA and HFSS," *Journal of Electronic Science and Technology*, vol. Vol. 3, no. No. 1, pp. Pages 45–47, March 2005.

[44] R. L. Haupt, "Using MATLAB® to Control Commercial Computational Electromagnetics Software," *ACES Journal*, vol. Vol. 23, no. No. 1, March 2008.

[45] S. Sun, Y. Lv, J. Zhang, Z. Zhao, and F. Ruan, "Optimization based on genetic algorithm and hfss and its application to the semiautomatic design of antenna," in *Microwave and Millimeter Wave Technology (ICMMT), 2010 International Conference on*, 2010, pp. 892–894.

[46] A. Boryssenko and N. Herscovici, "A MATLAB® based Universal CEM CAD optimizer," in *Antennas and Propagation Society International Symposium (APSURSI), 2012 IEEE*, 2012, pp. 1–2.

[47] N. Seshima, M. Tanaka, and H. Tsuboi, "Electromagnetic field analysis by using parallel processing based on openmp," in *Electromagnetic Field Computation,*

2006 12th Biennial IEEE Conference on, 2006, pp. 114–114.

[48] J. Alvarez Cedillo, J. Herrera Lozada, M. Olguin Carbajal, H. Taud, M. Enciso Aguilar, and A. Rodriguez Sanchez, "An OpenMP-based parallel algorithm for solving the three-dimensional FDTD Method," *Cahiers Des Sciences Naturelles*, 2011.

[49] B. Sun, L. Ping, and X. He, "Acceleration of time-domain finite-element method in electromagnetic analysis with Open MP," in *Microwave and Millimeter Wave Technology (ICMMT), 2010 International Conference on*, 2010, pp. 845–848.

[50] Z.-L. Liu and C.-F. Wang, "Open MP parallelization of NURBS-HOMM for electromagnetic scattering problems on multi-core computer," in *Antennas and Propagation Society International Symposium (APSURSI), 2010 IEEE*, 2010, pp. 1–4.

[51] M. Bane, R. Keller, M. Pettipher, and I. Smith, "A Comparison of MPI and OpenMP Implementations of a Finite Element Analysis Code," 2000.

[52] M. Su, I. El-Kady, D. Bader, and S.-Y. Lin, "A novel fdtd application featuring openmp-mpi hybrid parallelization," in *Parallel Processing, 2004. ICPP 2004. International Conference on*, 2004, pp. 373–379 vol.1.

[53] X. Pan, W. Pi, and X. Sheng, "On open MP parallelization of the multilevel fast multipole algorithm," in *Progress In Electromagnetics Research(PIER)*, 2011, pp. 199–213.

[54] L. Kun, "Graphics Processor Unit (GPU) acceleration of Time-Domain Finite Element Method (TD-FEM) algorithm," in *Microwave, Antenna, Propagation and EMC Technologies for Wireless Communications, 2009 3rd IEEE International Symposium on*, 2009, pp. 928–931.

[55] Y. Liu, shaohui Jiao, W. Wu, and S. De, "GPU accelerated fast FEM deformation simulation," in *Circuits and Systems, 2008. APCCAS 2008. IEEE Asia Pacific Conference on*, 2008, pp. 606–609.

[56] N. Goedel, T. Warburton, and M. Clemens, "GPU accelerated Discontinuous Galerkin FEM for electromagnetic radio frequency problems," in *Antennas and Propagation Society International Symposium, 2009. APSURSI '09. IEEE*, 2009, pp. 1–4.

[57] G. Addamo, O. Peverini, G. Virone, R. Tascone, and R. Orta, "Model-order reduction technique for the efficient analysis of complex waveguide structures 2014;an application to the design of corrugated horns," *Antennas and Wireless Propagation Letters, IEEE*, vol. 8, pp. 1039–1042, 2009.